



Libraries and Learning Services

University of Auckland Research Repository, ResearchSpace

Copyright Statement

The digital copy of this thesis is protected by the Copyright Act 1994 (New Zealand).

This thesis may be consulted by you, provided you comply with the provisions of the Act and the following conditions of use:

- Any use you make of these documents or images must be for research or private study purposes only, and you may not make them available to any other person.
- Authors control the copyright of their thesis. You will recognize the author's right to be identified as the author of this thesis, and due acknowledgement will be made to the author where appropriate.
- You will obtain the author's permission before publishing any material from their thesis.

General copyright and disclaimer

In addition to the above conditions, authors give their consent for the digital copy of their work to be used subject to the conditions specified on the [Library Thesis Consent Form](#) and [Deposit Licence](#).

Exploration of the Effects of Electrode Shape on the Performance of an Electrochemical Biosensor

Johnny Chung Yu Yeh

A thesis submitted to the
Department of Electrical and Computer Engineering
of the University of Auckland
in fulfilment of the requirements for the degree of
Doctor of Philosophy in Computer Systems Engineering

15th April 2018

Abstract

Analysis of biochemical samples is important in applications such as agriculture and medicine. The conventional methods of bioanalytical chemistry are mostly done inside specialist laboratories. However, recently there has been an increase of interest in developing new technologies that allow sample analysis to be performed on-the-spot. Electrochemical impedance biosensor is a promising candidate for creating portable and low-cost devices due to its simplistic signal transduction mechanism.

Improving the sensitivity of impedance biosensors is important in achieving the detection limit required for practical applications. The effect of three-dimensional electrode geometry on the performance of impedance biosensors was investigated in this thesis. Three distinct microelectrodes shapes, namely flat, ridge, and trough, were selected for comparison. The effectiveness of the three geometries were evaluated by the detection of micron-sized polystyrene beads using faradaic electrochemical impedance spectroscopy.

The conventional use of charge transfer resistance for modelling the change of impedance in faradaic impedance biosensors does not reflect the effect of electrode geometry. Therefore, an alternative model based on the diffusion process was developed. Finite element method was employed to simulate the change in diffusion impedance by solving Fick's second law of diffusion in the presence of particle obstructions. The model was validated against experiment data involving the detection of polystyrene beads using flat macroelectrodes. The model showed good agreement with observations, suggesting that the developed numerical model could be used to interpret the impedance response to captured particles.

The properties of the three-dimensional electrode were firstly investigated using the developed model. Simulation suggested the trough-shaped microelectrode exhibits greater impedance change upon analyte binding, owing to the focussing of diffusion flux due to the concaved geometry. Subsequently, flat and trough-shaped electrodes were fabricated and subjected to experimentation. The experimentally observed data agreed with the simulation with trough-shaped electrodes exhibiting greater impedance response upon analyte immobilisation. The result of this research contributes to improved understanding of how the faradaic process is involved in sensing applications. In addition, we also concluded that three-dimensional electrode geometry modulates the sensor properties and can be applied to improve the performance of impedance biosensors.

Acknowledgement

The work presented in this thesis could not be completed without the contribution and support from many individuals, and I can only hope to mention the most important persons here.

I would like to express my gratitude towards my main supervisor Professor Zoran Salcic and co-supervisor Dr. Kevin Wang for directing me throughout this PhD project. This thesis would not be completed without their guidance.

I would like to show my appreciation to the members at Digital Sensing Ltd. and Manufacturing Systems Ltd. for their contributions in this project. I want to thank Professor Ashton Partridge for his inputs toward this project. I also want to recognise Dr. Karthik Kannappan and Mr. Munther Ghanima for their help with sensor fabrication.

I would like to thank the people at Polymer Electronics Research Centre of the University of Auckland, particularly Bicheng Zhu and Professor Jadranka Travas-Sejdic for providing their expertise in the use of conducting polymer.

I want to acknowledge the University of Auckland and the Ministry of Business, Innovation and Employment of New Zealand (UOAX1201) for funding this research.

“This work was performed in part at the Bandwidth Foundry International part of the OptoFab node of the Australian National Fabrication Facility, a company established under the National Collaborative Research Infrastructure Strategy to provide nano and micro-fabrication facilities for Australia’s researchers.”

Table of Contents

Abstract	ii
Acknowledgement	iv
Table of Contents	v
Common abbreviations	viii
Common symbols	viii
Published works	ix
1. Bioanalytical Chemistry and Biosensors	1
1.1. Bioanalytical chemistry and current limitations	1
1.2. Biosensors	2
1.2.1. Research challenges for biosensor development	4
1.2.2. Fabrication technology and biosensor	5
1.3. Electrochemical biosensors and impedance spectroscopy	6
1.4. Contemporary bioanalytical chemistry methods and biosensing technologies	9
1.5. Research motivation and thesis outline	11
2. Electrochemical Impedance Biosensors	13
2.1. Principle of signal transduction in electrochemical impedance biosensor	13
2.2. Electrical models	14
2.2.1. Solution resistance R_{sol}	17
2.2.2. Double layer capacitance C_{dl}	17
2.2.3. Charge transfer resistance R_{ct}	20
2.2.4. Diffusion impedance Z_d	23
2.3. Geometric optimisation of impedance biosensor	31
2.3.1. Electrode geometry and sensor performance	31
2.3.2. Finite element method modelling in impedance biosensor research	33
2.4. Faradaic current in sensing and the effects of three-dimensional electrode geometry	38

3. Modelling Diffusion Impedance in the Detection of Micron-sized Targets.....	42
3.1. Introduction	42
3.2. Finite element simulation	42
3.2.1. FEM model setup.....	44
3.2.2. FEM simulation results	50
3.3. Experimental impedance measurement in the presence of polystyrene beads.....	56
3.3.1. Experiment procedure	56
3.3.2. Model validation.....	63
3.3.3. Application of diffusion impedance in sensing	73
3.4. Conclusion.....	82
4. Fabrication of Three-dimensional Microelectrodes	83
4.1. Introduction	83
4.2. Fabrication of the master template using photoresist reflow	86
4.2.1. Description of the master template	86
4.2.2. Fabrication process for the master template	87
4.3. Gold coating the master template	96
4.4. Nickel electroforming of the master template	98
4.5. Hot embossing	100
4.6. Defining electrodes with photolithography.....	101
4.6.1. Gold coating	101
4.6.2. Spin coat and softbake	102
4.6.3. Photolithography.....	103
4.6.4. Gold etching and photoresist strip-off.....	106
4.6.5. Challenges with ridge-shaped electrodes	108
4.7. Device setup	109
4.8. Conclusion.....	113
5. Effects of Three-dimensional Electrode Geometry on Sensor Performance.....	114
5.1. Introduction	114

5.2. Finite element model.....	114
5.2.1. FEM model setup.....	114
5.2.2. FEM simulation results	119
5.3. Experimental validation	128
5.3.1. Polystyrene beads binding on the microelectrodes.....	129
5.3.2. Impedance and sensor response of three-dimensional microelectrodes..	130
5.4. Conclusion.....	134
6. Research Contributions and Future Works	135
6.1. Significance of findings	135
6.2. Future research directions	140
6.3. Conclusion.....	141
Bibliography.....	143

Common abbreviations

CFU	colony forming units
CPE	constant phase element
FEM	finite element method
PETG	glycol-modified polyethylene terephthalate
PBS	phosphate buffered saline
PS	polystyrene

Common symbols

c	concentration
C_{dl}	double layer capacitance
D	diffusion coefficient
F	Faraday constant
i	current
j	imaginary number
R	universal gas constant
R_{ct}	charge transfer resistance
R_{sol}	solution resistance
T	temperature
v	voltage
Z	impedance
Z'	real component of impedance
Z''	imaginary component of impedance
Z_d	diffusion impedance
$Z_{Warburg}$	Warburg element
ω	angular frequency

Published works

Yeh J, Wang KI-K, Salcic Z, Kannappan K, Partridge A. (2015). Modelling impedance for 3D impedimetric biosensor. 2015 9th International Conference on Sensing Technology (ICST), Auckland, New Zealand, 08 Dec 2015 - 10 Dec 2015. Proceedings of the International Conference on Sensing Technology, ICST. 34-39. 2015

Yeh J, Zhu B, Wang KI-K, Salcic Z, Kannappan K, Partridge A. (2016). "Modelling diffusion impedance in the sensing of micron-sized particles." Sensors and Actuators B: Chemical **237**: 329-340.
<https://doi.org/10.1016/j.snb.2016.06.065>

1. Bioanalytical Chemistry and Biosensors

1.1. Bioanalytical chemistry and current limitations

Detection and quantification of chemical and biological analytes are an essential part of a myriad of application fields. These include areas such as:

- food safety [1-6]
- medical diagnosis [7-12]
- agriculture [5, 13-16]
- environmental monitoring [17-21]
- consumer test kits related to health and physiology [22-24]

All the listed disciplines would benefit from the ability to perform immediate sample analysis in the field. For instance, having the capability to confirm food safety quickly and accurately enables faster harvest-to-shelf time, thus reducing the cost of holding inventory and prevent costly recalls of contaminated products. Identifying the cause of infection or intoxication of a patient with point-of-care diagnosis allows the corresponding treatment to be administered more quickly. A shorter delay to treatment is often the central factor in determining the outcome and survivability of the patient.

The conventional procedures for analysing biological and chemical samples involve techniques such as ELISA (enzyme-linked immunosorbent assay), PCR (polymerase chain reaction), and selective medium culturing. These methods usually involve elaborate processing steps such as sample enrichment and analyte labelling, which prolong the overall analysis time and require trained personnel to execute [4, 25, 26]. Moreover, these procedures often require complex and expensive equipment to carry out. As a result, bioanalytical chemistry procedures such as ELISA and PCR are

performed almost exclusively in laboratory settings. Test samples are usually sent to specialist facilities for processing, and the analysis can take several days before the result is returned. Therefore, there is tremendous interest in developing new bioanalytical chemistry technologies that are more convenient and accessible to use in the field.

1.2. Biosensors

Biosensors are devices that can be used to analyse biological and chemical samples in the field in an accessible manner. To achieve this goal, the technology needs to exhibit qualities such as easy to operate, short analysis time, cost-effective, portable, as well as having sufficiently sensitive and reliable measurements.

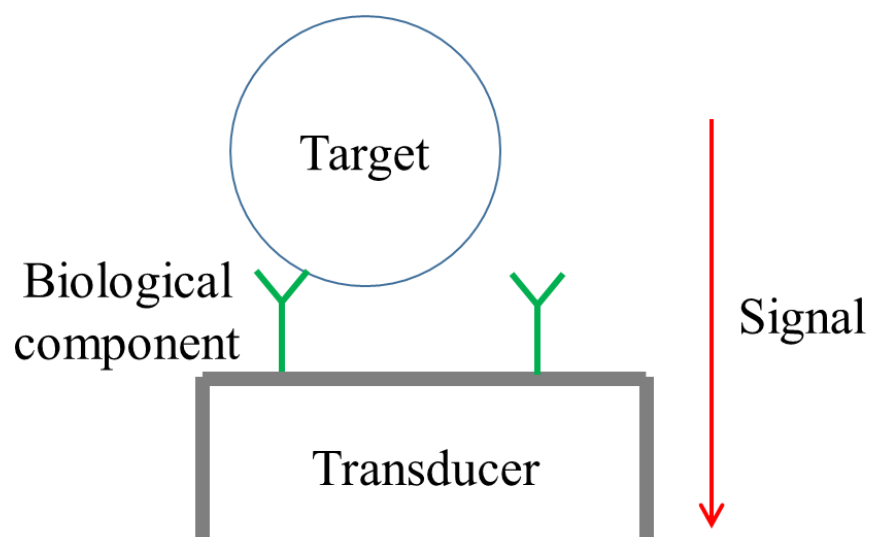


Figure 1.1. Illustration of the elements of a biosensor. The target analyte interacts with the biological component. The transducer converts this interaction to a signal appropriate for readout.

Biosensors are made up of a biological component and a transducer component (Figure 1.1). The biological component interacts specifically with the analyte of interest. A sensor can be made to detect a variety of target analytes by selecting the appropriate biological component. A large proportion of biosensors are affinity-based [27], which involves the biological components acting as probes that selectively immobilise the analyte of interest on the sensor's surface. Other probes may catalyse chemical reactions specifically with the target analyte, for example, the glucose oxidase enzyme used in blood glucose biosensors [22, 28]. The different types of biological component which have been used in biosensors include:

- antibodies [29, 30]
- proteins [22, 31-34]
- single stranded DNAs [35, 36]
- aptamers [37, 38]

while common target analytes of a biosensor include:

- cells (bacterial and eukaryotic) [30, 31, 39]
- proteins [40, 41]
- nucleic acids [35, 42]
- viruses [29, 43]
- small molecules [28, 41]

The transducer component of a biosensor converts the interaction between the analyte and the biological component to a proportional signal in a form that is appropriate for readout. Examples of signal transduction mechanisms that have been applied in biosensors include optical (photometric and surface plasmon resonance), piezoelectric (quartz crystal microbalance and resonant cantilever), and electrochemical.

Some biosensors rely on the use of labels for signal transduction or to enhance the signal strength. Examples include the use of fluorophore labels to emit light signal for readout [44] and magnetic bead labels used to produce a detectable interference in the magnetic field [45]. However, the use of labelling means additional reagents and processing steps are required, which makes achieving sample analysis in the field more challenging.

1.2.1. Research challenges for biosensor development

The main barriers limiting biosensor from being widely applied in real world applications include difficulties in achieving sufficient sensor selectivity, limit of detection, and reproducibility in the sensor readout.

Selectivity is the ability of a sensor to detect the target analyte from a matrix of background molecules. This is especially important in real world contexts as the analyte of interest may be present at a very small fraction out of the total molecules in the test sample. For instance, prediction of prostate cancer needs to detect prostate specific antigen at 2 ng/mL from a total protein content of 70 mg/mL in the blood serum [46]. Most of the biosensors reported in literatures are characterised with pure test samples in the absence of interfering molecules, and their performances against real world samples are uncertain. Sample pre-purification may be used to remove a proportion of background molecules to improve the selectivity of the overall analysis procedure. However, the number of additional sample treatment steps can be reduced when the biosensor has high selectivity.

Biosensors also require low limits of detection (high sensitivity) since the analyte of interest may need to be detected at very low concentrations for real world applications. For example, the maximum accepted value for the presence of *Escherichia*

coli in drinking water set by New Zealand Ministry of Health is 1 unit per 100 mL [47]. The maximum residual levels of contaminating compounds in agricultural products are usually in the range of micrograms to milligrams per kilogram of product depending on the compound [48]. A sample pre-concentration step may be required prior to the detection step under these situations.

The lack of robust sensor quality due to challenging fabrication processes leads to problems with readout consistency across individual sensors. This can be a result of the variabilities in the deposited biological components as well as in the manufacturing of the transducer component. This variation can adversely impact the confidence of data interpretation. The typical approach to reducing the effect of variations between individual sensors is to calibrate the readout of each sensor against a blank measurement.

1.2.2. Fabrication technology and biosensor

Opportunities for device miniaturisation and creating unique sensor designs have opened up with recent advancements in micro and nanofabrication technologies [49, 50]. Device miniaturisation is typically associated with improvements in the sensor's sensitivity [51, 52]. This is because analytes interacting with a smaller active sensor area induce a relatively greater signal change. In addition, the required total sample amount can be reduced to microlitre volumes using a microfluidic system [53-56]. The throughput of a sensor device can be multiplied by packaging several miniaturised sensor components into one device and perform measurements in parallel [57]. Creation of uniquely designed sensor geometry and form factors are used to address specific applications more effectively [58-60]. For instance, Klob et al. created electrodes embedded in microcavities which are used to house multicellular cultures as to mimic in vivo-like conditions [61].

A common application of fabrication technology in biosensor research is the enhancement of biosensor performance through optimising the transducer geometry. The research in this thesis focuses on investigating how microfabrication techniques can be used to produce different three-dimensional electrode geometries to improve the performance of electrochemical impedance biosensors, particularly in terms of sensitivity.

1.3. Electrochemical biosensors and impedance spectroscopy

Electrochemical biosensors rely on electrochemical processes for signal transduction [62-64]. The transducer of an electrochemical biosensor is simply a set of electrodes that are used to simultaneously electrically excite the electrochemical cell and readout the electrical current response. The electrical properties of an electrochemical system are mainly dictated by the chemical contents of its cell. For instance, the ionic content of the electrolyte controls the electrical conductivity of the solution. Counterions can stabilise the accumulation of charges on the electrode's surface, thus introducing a capacitive effect. Electroactive molecules in the solution can undergo heterogeneous redox reaction with the solid electrode, transferring electrons in the process and causing current to flow. The binding of a target analyte can directly affect these processes and produce a detectable change in the electrical signal, allowing label-free sensing to be achieved. The ability to perform label-free sensing is advantageous for simplifying the overall analysis procedure of an electrochemical biosensor. Although labelling is also possible for electrochemical biosensors. For instance, labelled-enzyme catalysed precipitation of insoluble product on the electrode surface can cause a larger decrease in the overall electrode conductivity [65, 66].

Researchers have also used magnetic beads to aggregate the target analyte to the electrode surface as to increase the size of the entity being observed [67-70].

Electrochemical measurement involves applying an electrical excitation across terminals of an electrochemical cell system. A potentiostat is the instrument used to perform electrochemical measurements. It generates the required excitation signal and reads the current response. For a two-electrode electrochemical system, the excitation is applied across the counter and working electrodes. In a three-electrode system, an additional reference electrode measures the potential of the solution to provide feedback to the measuring circuit. The counter electrode of a three-electrode system in turn attempts to maintain the solution potential at the desired level relative to the working electrode. Response measurement usually happens at the working electrode and is usually the one modified with biological components. A three-electrode setup is useful for removing in the readout the contribution of electrochemical processes happening at the counter electrode, so that the observed current response is mostly determined by what is happening at the working electrode.

A major advantage of an electrochemical sensor is that the transducer is very simple. Only a set of conductors acting as electrodes is required to simultaneously perform system excitation and signal readout, which means the sensors can be fabricated easily. Since the excitation and response signals are already in electrical form, the potentiostat measuring instrument is also relatively trivial. These taken together help with lowering the cost of the biosensor and improve the portability of the overall device. For these reasons, electrochemical biosensors are the most popular type of biosensors reported in the literatures.

Electrochemical biosensors are categorised based on the type of excitation signals used in measurement, and the most common techniques are amperometric,

voltammetric, and impedimetric [62]. Amperometric and voltammetric techniques involve a relatively large DC excitation, usually with the intention to drive a chemical reaction at the electrode by changing the electrode conditions. The large electric potential applied in amperometric and voltammetric measurements can cause the biological component to be modified or disrupted. This is usually unfavourable in biosensing applications as the change can cause drifts in measurements and influence the accuracy of sensing result. In contrast, impedimetric measurement involves a small AC excitation superimposed on a steady state DC offset with the goal to minimise change to the electrode caused by the measuring process.

The properties of an electrochemical system are determined by a combination of different physical processes of different time constants. All components convolve together in the readout signal for time-domain measurements such as amperometry and voltammetry. On the other hand, frequency-domain measurements like electrochemical impedance spectroscopy (EIS) naturally separates the information for each component into different frequency ranges based on the time constant of the process; a particular physical phenomenon can be observed by exciting the system at specific frequencies. This has the potential to provide more detailed insight into the processes that is operating in the electrochemical system. The more intricate information can contribute to identifying more subtle changes caused by analyte-sensor interaction and improve the detection limit of the sensing technique. For these reasons, EIS is a particularly popular measurement technique for electrochemical biosensor [71-73]. However, EIS being a sensitive technique also means it is susceptible to non-specific signal and noise [74]. Therefore, the sensor readouts often need to be compared to a robust system of control measurements for reliable data interpretation.

1.4. Contemporary bioanalytical chemistry methods and biosensing technologies

Immunoassay methods such as enzyme-linked immunosorbent assay (ELISA) are performed regularly for analytical chemistry and are able to provide analyte detection at high sensitivity. However, the technique usually requires trained personnel to carry out and is time consuming [1, 75, 76]. One major limitation with immunoassays is the difficulty in the miniaturisation and integration of all the necessary steps into a single portable device, making quantitative analysis in the field hard to achieve. Nevertheless, the technology is applied in portable lateral flow tests in applications where a qualitative analysis is sufficient [77]. A well-known example of such device is the pregnancy test kit.

Polymerase chain reaction (PCR) is another well-established method for analytical chemistry. It is usually more sensitive than ELISA and also faster with ~5 hours analysis time [76]. However, the technique is only applicable to nucleic acid analytes. Typically, extra processing steps are necessary to extract and purify the genetic materials from the sample. The method also requires expensive equipment and reagents that are only available in laboratories. Although recently there have been attempts to make this technology more portable [78, 79], while successful for parts of the overall process, it is still difficult to carry out the whole PCR analysis in the field in an accessible fashion.

Surface plasmon resonance is a well-researched biosensing technique which relies on manipulating the optical properties of the biological element for signal transduction [80]. The technique can be performed label-free. However, the fact that it is an optics-based method means it requires more sophisticated instrument for sensor

excitation and readout, which is a barrier for making inexpensive and portable devices. The detection limit is usually worse for surface plasmon resonance in comparison to impedance biosensor. Impedimetric measurement was found to have a much lower detection limit (12 CFU/mL) than the surface plasmon resonance technique (6.1×10^7 CFU/mL) for direct sensing of *Escherichia coli* using concanavalin A as the biorecognition element [32]. Another publication has found a similar conclusion using biotin-neutravidin interaction for immobilising the *Escherichia coli* bacteria [67].

Quartz crystal microbalance and **mechanical cantilever** are examples of novel mechanical biosensors currently in a similar stage of research as impedance biosensors [81-83]. Both approaches can perform label-free sensing like impedimetric sensors. While quartz crystal microbalance biosensors have worse performance in terms of limit of detection, cantilever biosensors have reported similar performance as impedance biosensors [1, 7]. The shortcoming of these mechanical biosensors is related to their complex transducer technology, making the sensors more difficult and expensive to produce at a mass scale.

Electrochemical amperometric biosensor is generally less sensitive than **impedimetric biosensor**. This means a label that amplifies the change in electrical current is usually necessary for amperometric biosensors while impedimetric biosensor can be label-free [84]. However, amperometric sensors are very successful when the interaction between the target analyte and the biorecognition element of the sensor directly generates the electrical current for readout. An example of this is the commercially successful electrochemical blood glucose sensor for diabetic patients [22], in which glucose oxidase on the electrode surface catalyses the oxidation of glucose and generates an observable electrical current response.

The key strength of electrochemical biosensor lies in its simple transducing mechanism. The transducer for the biosensor is simply a set of conductors acting as electrodes, which can be integrated with MEMS to create a single compact device that conveniently performs all the steps involved with analyte detection. In addition, the excitation and readout signals are electrical, which can be generated and read very easily with a simple interfacing circuit. These characteristics mean electrochemical biosensors hold great promise for creating cost effective and portable biosensing devices that are capable of on-the-spot quantitative analysis, which is advantageous in comparison to qualitative methods such as lateral flow tests. However, electrochemical biosensor can be expensive to produce depending on the material used to create the sensor and the extent of integration with the fluidic and electronic components. This is a major barrier for commercialising electrochemical biosensors.

1.5. Research motivation and thesis outline

Currently, it is difficult to achieve direct sensing of samples in the field with any biosensor technology due to the extremely low limit of detection required for real world applications. Therefore, enhancing the sensitivity of electrochemical impedance biosensors has been a strong research focus, and so far it has shown competitive performance advantages to other contemporary technologies. In this work, we investigated the use of microfabrication methods to create three-dimensional electrode geometries and examined their effects on the performance of the impedance biosensors.

Chapter 2 of this thesis provides the fundamental theory of the mathematical modelling of electrode impedance with focus given to diffusion impedance. Chapter 3 reports on the mathematical model developed to explain the impedance change observed upon analyte recognition based on blocked diffusional transport of

electroactive molecules. Chapter 4 outlines the fabrication process developed for fabricating the three-dimensional electrodes used in experimental testing. In Chapter 5, the three-dimensional electrodes are compared using the developed mathematical model and then experimentally. Finally the results of this work are discussed and future works are proposed in Chapter 6.

2. Electrochemical Impedance Biosensors

2.1. Principle of signal transduction in electrochemical impedance biosensor

Electrochemical impedance biosensor utilises electrochemical impedance spectroscopy (EIS) as the transducing technique for sensor readout [71, 72, 85]. Typically, a sinusoidal voltage excitation signal $V(\omega)$ of a specified frequency ω is superimposed on a DC offset at the open-circuit potential of the electrochemical cell V_{DC} . This voltage excitation drives a current response $I(\omega)$ that is measured, which reflects the properties of the electrochemical cell and the conditions of the electrode surface. Biorecognition of the target analyte can change these properties, and the corresponding change in the current response is the basis for the readout of impedance biosensors. The readout is usually interpreted in the form of impedance $Z(\omega)$, which is calculated as the ratio between the applied AC voltage $v_{AC}(\omega)$ and the AC current response $i_{AC}(\omega)$ (Equation 2.3).

$$V(\omega) = V_{DC} + v_{AC}(\omega)e^{j\omega t} \quad (\text{Equation 2.1})$$

$$I(\omega) = I_{DC} + i_{AC}(\omega)e^{j(\omega t - \varphi)} \quad (\text{Equation 2.2})$$

$$\boxed{Z(\omega) = \frac{v_{AC}(\omega)}{i_{AC}(\omega)} e^{j\varphi}} \quad (\text{Equation 2.3})$$

Voltage excitations at various frequencies are applied to the system to deduce the impedance spectrum. In most cases, AC excitation is applied one frequency at a time and is repeated over a defined frequency range. Sometimes a voltage signal composed of multiple frequency information may be used to acquire measurements at different frequencies simultaneously to reduce the data acquisition time. These signals include multi-sine wave, chirp signal, wavelet, pulse signal, and step signal [86-92].

Typically, the AC voltage excitation has a small amplitude (~ 10 mV). Firstly, this is because a small voltage excitation helps to minimise the disruption to the biofunctional layer and probe-target interaction on the electrode surface. This would reduce variations in the electrode condition over repeated measurements. Secondly, the voltage-current relationship of an electrochemical system is not linear over a large voltage range. Impedance would not be adequate for interpreting the observed measurements under this situation since impedance describes linear systems only. However, electrochemical systems can be approximated with a linear behaviour when excitations of small voltage differentials are used.

2.2. Electrical models

There are two primary forms of current that can be generated in response to a voltage excitation in electrochemical systems. The first is non-faradaic current generated by the transient charging and discharging of capacitance at the electrode surface. In this case, electrons do not physically cross the electrode-solution interface. The main cause for this current flow is due to the electric double layer capacitance phenomenon at the electrode-solution interface. The second type is faradaic current. Here, electrons are physically exchanged between the electrode and the electroactive molecules in the solution. This occurs via a heterogeneous redox reaction. The reaction

depletes reactants and build-up products near the electrode surface, which need to be replenished or removed for the reaction to continue. This mass transfer of electroactive molecules also contributes to the impedance in the faradaic current path.

Randles circuit is the conventional circuit model used to interpret electrode impedances [71-73, 85]. Sometimes, modified Randles circuits are used to accommodate unique sensor constructs. These may reflect variations in the electrode material, form factor of the sensor, or biofunctionalisation of the sensor surface [87, 93-95]. Typically a circuit model is assumed a priori based on known information about the current paths that operate in the system.

The standard Randles circuit and its characteristic Nyquist plot are shown in Figure 2.1. The electric double layer capacitance (C_{dl}) models the non-faradaic current flow, whereas faradaic current path is commonly modelled with a series combination of charge transfer resistance (R_{ct}) and diffusion impedance (Z_d). Solution resistance (R_{sol}) models the electrical conductivity of the bulk solution due to mobile ions.

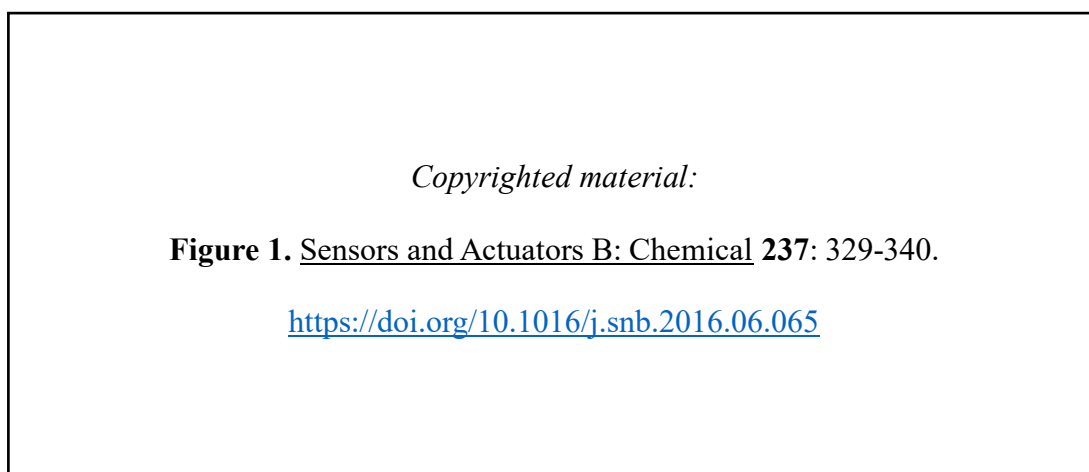


Figure 2.1. Randles circuit (A) and its Nyquist plot (B). C_{dl} is often modelled as a constant phase element (CPE). The red line in the Nyquist plot denotes the faradaic impedance components.

Since non-faradaic and faradaic processes are two parallel paths of current, the path with higher rate of current flow would dominate in the observed electrode impedance. The non-faradaic current is proportional to frequency while the diffusion component of the faradaic process is proportional to the square root of the frequency. This means the current in the non-faradaic path decreases more rapidly with decrease in frequency in comparison to the faradaic path. Therefore, the non-faradaic path usually dominates at high frequencies while the faradaic path dominates at lower frequencies. The non-faradaic component appears as the semicircle near the origin of the Nyquist plot, which represents the high frequency section of the impedance spectrum. The faradaic current path dominates as the excitation frequency decrease, and the impedance is predominantly determined by the diffusion impedance of the faradaic process at very low frequencies.

Although a one-to-one correspondence is assumed between the circuit model components and the physical processes that contribute to electrode current, this may not be strictly true. Also, many of the phenomena do not behave the same as ideal circuit components, for instance, the linearity of voltage-current relationship. Nevertheless, circuit models are still used to fit experimental data in order to make sense of and interpret the observed electrode impedance. Each component of the Randles circuit is described in more detail in the following sections.

2.2.1. Solution resistance R_{sol}

$$R_{sol} = \frac{1}{\sigma} \kappa$$

(Equation 2.4)

The movement of mobile ions in the solution in response to electric field generates current. This is modelled by the solution resistance R_{sol} (Equation 2.4). The solution resistance is inversely proportional to the conductivity σ of the cell's electrolyte. The cell constant κ is a value associated with the electric field line distribution between the electrode terminals. For the classic two parallel plate terminals, κ is the distance between two plates divided by the area of the plates. For coplanar electrodes, κ can be estimated using Schwarz–Christoffel conformal mapping [96].

Increase in the solution resistance causes the electrode impedance plot to shift to the right along the real axis (x-axis).

2.2.2. Double layer capacitance C_{dl}

Charges accumulate on the electrode surface when a voltage excitation is applied across the electrode-solution interface. As a result, mobile counterions in the solution are attracted to the electrode. This process stabilises the high charge density on the electrode surface and allows the electrode to store charge like a capacitor. This phenomenon is termed electric double layer. The capacitance can be very high due to the fact that ions in the solution can approach the electrode very closely at sub nm range, which corresponds to the radius of hydrated ions. This is akin to having a very small plate separation in a conventional capacitor. In addition, the dielectric between the two charge layers in this case is water, which has high dielectric constant. The biofunctionalisation of the biosensor surface would usually decrease the double layer

capacitance [97]. Firstly, it increases the separation between the two “plates” of the capacitance. Secondly, the dielectric constant of the biological components are usually lower than that of the water.

Sterns model is commonly used to describe double layer capacitance [98]. It describes a high density of counter charge at the plane of closest approach (Helmholtz layer) and an exponential decay of the charge density towards the bulk of the solution in the diffusion layer. The charge-potential relationship for this model has an exponential term and so it is non-linear [98-101]. Although the theory of double layer capacitance is complex, its model can be simplified to an ideal capacitance component in practice when a small voltage range is used for excitation.

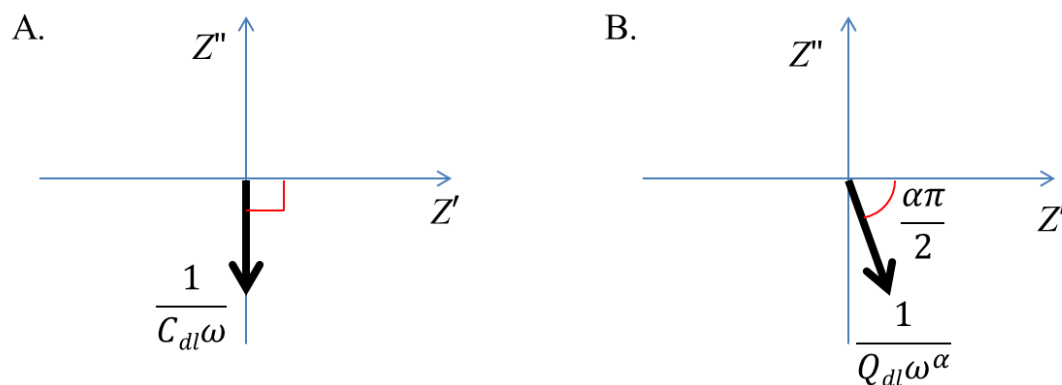


Figure 2.2. Complex plane representation of (A) an ideal capacitor reactance component and (B) a CPE impedance component.

$$Z_{ideal\ capacitor} = \frac{1}{j\omega C_{dl}} = \frac{1}{\omega C_{dl}} e^{-j\frac{\pi}{2}}$$

(Equation 2.5)

$$Z_{CPE} = \frac{1}{(j\omega)^\alpha Q_{dl}} = \frac{1}{\omega^\alpha Q_{dl}} e^{-j\frac{\alpha\pi}{2}}$$

(Equation 2.6)

j: imaginary number $\sqrt{-1}$

ω : angular frequency of excitation signal (radians.s⁻¹)

C_{dl} : double layer capacitance

The voltage across an ideal capacitor component lags the current by 90° phase. However, the capacitance component observed in electrochemical systems often has a phase that is slightly less than 90°. The explanation for this observation is attributed to factors such as surface roughness and current distribution heterogeneity. Therefore, it is more often that a constant phase element (CPE) is used instead of an ideal capacitor to fit the experimentally observed impedance data [102]. The complex plane representations of the impedance of the two components are shown in Figure 2.2. The expressions for the impedance component of an ideal capacitor and a CPE are shown in Equation 2.5 and Equation 2.6, respectively.

An increase in double layer capacitance causes the semicircle of the Nyquist plot to join up with the diffusion component (Z_d) at a lower frequency.

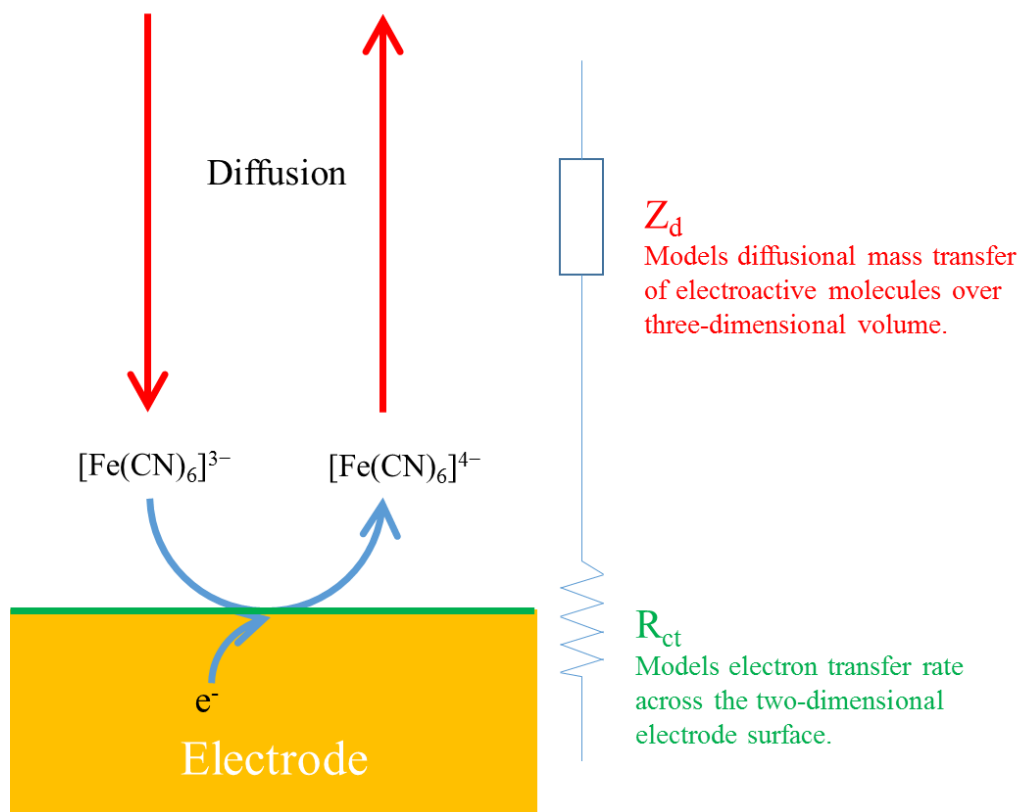


Figure 2.3. Graphical representation of the faradaic reaction process.

2.2.3. Charge transfer resistance R_{ct}

Electron transfer can occur between the electrode and electroactive molecules in the solution via heterogeneous redox reaction (Figure 2.3). This phenomenon generates faradaic current. The reaction kinetics for this reaction is described by the Butler-Volmer equation (Equation 2.7) [103]. The voltage-current relationship described by the equation is non-linear, which is beyond the conventional circuit theory.

$$i = k_0 n F \left[c_O e^{\frac{\alpha_a n F (v - v_{eq})}{RT}} - c_R e^{-\frac{\alpha_c n F (v - v_{eq})}{RT}} \right]$$

$$= k_0 n F \left[c_O e^{\frac{\alpha_a n F \eta}{RT}} - c_R e^{-\frac{\alpha_c n F \eta}{RT}} \right]$$

(Equation 2.7)

- i = current density A/m², going from solution to electrode
- k_0 = electron transfer rate constant (m/s)
- n = number of electrons involved in reaction
- c_O, c_R = electrode surface concentration of oxidised and reduced species, respectively (mol/m³)
- α_a, α_c = anodic and cathodic charge transfer coefficient, respectively. The sum of the two is always 1.
- F = Faraday's constant
- R = Universal gas constant
- T = temperature (K)
- v = applied electrode potential (V)
- v_{eq} = equilibrium potential (V)
- $\eta = v - v_{eq}$ = electrode overpotential (V)

The Butler-Volmer equation can be simplified if the concentrations of oxidised and reduced species are the same ($C = c_O = c_R$), and the anodic and cathodic charge transfer coefficient are equal ($\alpha_a = \alpha_c = 0.5$). In addition, the exponential relationship can be linearised when the applied electrode potential is small. The result is the following simplified equation.

$$i = k_0 n F C \left[\left(1 + \frac{0.5 n F \eta}{RT} \right) - \left(1 - \frac{0.5 n F \eta}{RT} \right) \right]$$

$$= \frac{k_0 C n^2 F^2 \eta}{RT}$$

(Equation 2.8)

Differentiating the equation to find $\frac{d\eta}{di}$ yields the charge transfer resistance R_{ct} .

$$R_{ct} = \frac{d\eta}{di} = \frac{RT}{k_0 C n^2 F^2}$$

(Equation 2.9)

A larger charge transfer resistance leads to a larger semicircle on the electrode impedance Nyquist plot.

2.2.4. Diffusion impedance Z_d

2.2.4.1. Mathematical model

The charge transfer redox reaction depletes reactants and generates products at the electrode surface. These must be replenished or removed for the reaction to continue (Figure 2.3). There are a number of different phenomena and corresponding physical laws that contribute to the movement of electroactive molecules in electrochemical systems. However, the dominating process that controls the mass transfer is by diffusion, which is driven by the Brownian motion of molecules in a concentration gradient. Electrostatic effects can be ignored when non-electroactive ions of the supporting electrolyte are in excess of the electroactive molecules, which shields the effect of electric field that would otherwise exert on the electroactive species. The diffusion process is mathematically described by Fick's second law. Its time domain (Equation 2.10) and frequency domain forms (Equation 2.11) are shown below. This movement of the electroactive molecules introduces the diffusion impedance component in the faradaic current path.

$$\frac{\partial c}{\partial t} = \nabla \cdot D \nabla c$$

(Equation 2.10)

$$j\omega c = \nabla \cdot D \nabla c$$

(Equation 2.11)

c : concentration ($\text{mol.m}^{-3} \equiv \text{mM}$)

t : time (s)

D : diffusion coefficient ($\text{m}^2.\text{s}^{-1}$)

ω : angular frequency of excitation signal (radians.s^{-1})

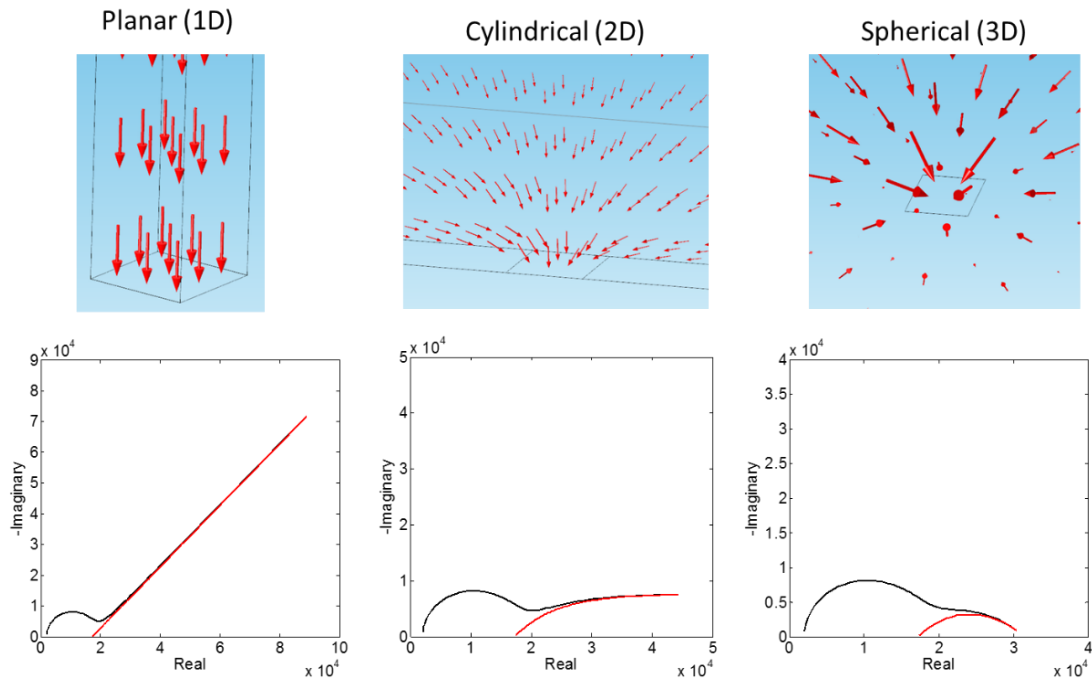


Figure 2.4. Top: graphical representations of planar, cylindrical, and spherical diffusion patterns. Red arrows depict the diffusion flux. Bottom: the corresponding electrode impedance Nyquist plot for each situation. The red line depicts the diffusion impedance component.

The diffusion impedance is distinguishable for different diffusion patterns. For instance, the diffusion impedance is different for planar, cylindrical, and spherical diffusion patterns (Figure 2.4). The diffusion impedance for a semi-infinite planar diffusion is also known as the Warburg element.

Fick's second law can be solved analytically for the semi-infinite planar diffusion pattern, for which all the diffusion happens in the direction normal to the electrode surface. In this case, the problem can be reduced to a one-dimensional problem by symmetry and the analytical solution for the diffusion impedance is the Warburg element Z_{Warburg} (Equation 2.12). A derivation of Warburg element is shown in the book by Bard & Faulkner [104]. Jacobsen et al. [105] derived the diffusion impedance for

the general case of planar diffusion in the presence of absorbing or blocking boundaries. Warburg element can be reached from their general solutions by defining infinite distance between the boundaries and the electrode surface, such that the diffusion pattern becomes semi-infinite. One can observe that the diffusion impedance of a semi-finite planar diffusion pattern has equal magnitudes for both the real and imaginary components. Therefore, the diffusion impedance spectrum for a Warburg element appears as a unity-sloped (45°) straight line in the complex plane.

Semi-infinite planar diffusion impedance (Warburg element)

$$\begin{aligned}
 Z_{Warburg} &= \left[\frac{v^2 RT}{(nF)^2 c^*} \right] \frac{1}{\sqrt{D} \sqrt{j\omega}} \\
 &= \left[\frac{v^2 RT}{(nF)^2 c^*} \right] \frac{1}{\sqrt{D} \sqrt{2\omega}} (1 - j)
 \end{aligned}$$

(Equation 2.12)

R: gas constant

T: temperature (K)

n: number of electrons involved in the charge exchange equilibrium

F: Faraday constant

v: stoichiometric number

c^{*}: bulk concentration of the electroactive species (mol.m⁻³)

*Z*_{Warburg} has unit Ωm²

The analytical solutions for diffusion impedances with cylindrical or spherical diffusion patterns can be reached similarly by exploiting their rotational symmetry [105]. Their equations are shown below.

Semi-infinite cylindrical diffusion impedance

$$Z_{cylindrical} = \left[\frac{v^2 RT}{(nF)^2 c^*} \right] \left(\frac{r_0}{D} \right) \frac{K_0[\psi_0]}{\psi_0 K_1[\psi_0]} \quad (\text{Equation 2.13})$$

$$\psi_0 = r_0 \sqrt{\frac{j\omega}{D}} \quad (\text{Equation 2.14})$$

r_0 : radius of the cylindrical electrode.

K_x : x^{th} order modified Bessel function of the second kind.

Semi-infinite spherical diffusion impedance

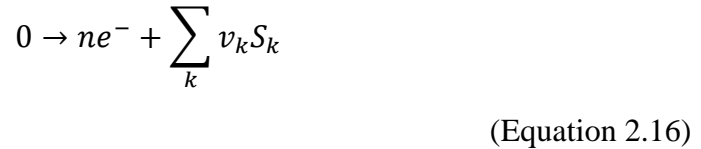
$$Z_{spherical} = \left[\frac{v^2 RT}{(nF)^2 c^*} \right] \left(\frac{r_0}{D} \right) \frac{1}{1 + \psi_0} \quad (\text{Equation 2.15})$$

r_0 : radius of the spherical electrode.

The definition for ψ_0 is the same as the cylindrical case (Equation 2.14).

2.2.4.2. Warburg element for a redox couple

Equation 2.12 shows the Warburg element contribution for one electroactive molecule species. For charge transfer reactions that simultaneously involve more than one chemical species S_k , described by the chemical equation in Equation 2.16, the diffusion impedance contribution for species S_k is the expression in Equation 2.17.



$$Z_{Warburg\ k} = \left[\frac{v_k^2 RT}{(nF)^2 c_k^* \sqrt{D_k}} \right] \frac{1}{\sqrt{j\omega}} \quad (\text{Equation 2.17})$$

v_k : stoichiometric number of species k in the redox reaction

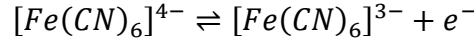
Subscript k indicates the parameters are for chemical species S_k

Assuming the diffusion of all chemical species occurs on one side of the electrode (i.e. in the solution and not in the electrode), the overall diffusion impedance is the sum of the individual impedance contribution of each species (Equation 2.18).

$$Z_{Warburg}^{total} = \sum_k Z_{Warburg\ k} \quad (\text{Equation 2.18})$$

A common case of the charge transfer reaction involves the transfer of one electron with the electrode by consuming one reactant and generating one product in a reaction equilibrium. The reactant diffuses toward the electrode while the product diffuses away. An example of this reaction is the ferrocyanide/ferricyanide redox pair (IUPAC nomenclature: hexacyanoferrate (II/III)) (Equation 2.19). The total impedance is the

sum of their individual contributions with $-v_R = v_o = 1$ and $n = 1$ (Equation 2.20). The subscripts R and O denote parameters for the reduced and oxidised species of the redox couple, respectively. In this case, Equation 2.20 can be simplified to Equation 2.22.



(Equation 2.19)

$$Z_{Warburg}^{total} = \left[\frac{v_R^2 RT}{(nF)^2 c_R^* \sqrt{D_R}} \right] \frac{1}{\sqrt{2\omega}} (1 - j) + \left[\frac{v_o^2 RT}{(nF)^2 c_o^* \sqrt{D_o}} \right] \frac{1}{\sqrt{2\omega}} (1 - j)$$

(Equation 2.20)

$$Z_{Warburg}^{total} = \frac{RT}{F^2 \sqrt{2}} \left(\frac{1}{c_R^* \sqrt{D_R}} + \frac{1}{c_o^* \sqrt{D_o}} \right) \frac{1}{\sqrt{\omega}} (1 - j)$$

(Equation 2.21)

$$Z_{Warburg}^{total}(\omega) = \frac{A_W}{\sqrt{\omega}} (1 - j)$$

(Equation 2.22)

$$A_W = \frac{RT}{F^2 \sqrt{2}} \left(\frac{1}{c_R^* \sqrt{D_R}} + \frac{1}{c_o^* \sqrt{D_o}} \right)$$

(Equation 2.23)

The constant A_W is also known as the Warburg coefficient. Because the diffusion of both redox couple species happen simultaneously upon a sinusoidal excitation in impedance spectroscopy, it is impossible to distinguish between the diffusion coefficients of each species from the impedance spectrum. If the bulk concentrations of both species are the same ($C^* = c_R^* = c_o^*$), the Warburg coefficient can be simplified to the following with an observed overall diffusion coefficient D_s .

$$A_W = \frac{RT\sqrt{2}}{(nF)^2 C^* \sqrt{D_S}}$$

(Equation 2.24)

$$\sqrt{D_S} = \frac{2\sqrt{D_R D_O}}{\sqrt{D_R} + \sqrt{D_O}}$$

(Equation 2.25)

2.2.4.3. Diffusion distance

An active excitation signal applied to the electrode causes a perturbation in electroactive species concentration. This perturbation propagates from the electrode surface until the effect dissipates and stabilises at the bulk concentration. The perturbation in concentration creates the concentration gradient that drives the diffusional movement of the molecules. The diffusion distance is a measurement for the extent of this phenomenon. It is related to how far away from the electrode surface the diffusion occurs, and determines the extent of the region above the electrode that is reflected by measurements of diffusion impedance.

$$\lambda = \sqrt{\frac{D}{\omega}}$$

(Equation 2.26)

For semi-infinite planar diffusion, the characteristic diffusion distance λ [106] of a electroactive molecule is related to the frequency of the excitation and the diffusion coefficient of the species (Equation 2.26). The diffusion distance increases with lower frequency excitation signal, and the impedance measurements convey information from within a greater distance away from the electrode surface. The typical characteristic

diffusion distances for the frequency range and experiment parameters used in biosensing are in the micrometre range.

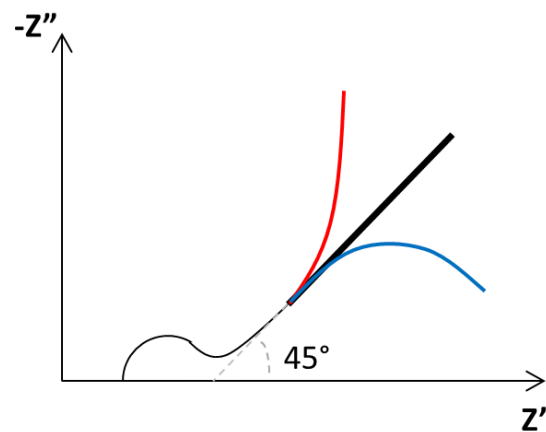


Figure 2.5. Nyquist plots of diffusion impedance in the presence of a blocking boundary (red) and an absorbing boundary (blue). The pattern for semi-infinite diffusion is also shown for comparison (black)

2.2.4.4. Blocking and absorbing boundaries

The presence of a barrier that blocks or absorbs diffusion flux can also affect the diffusion pattern and the diffusion impedance (Figure 2.5) [105, 106]. A blocking boundary is a surface that stops all molecule flux. An example of this boundary is the walls of the sensor's fluidics channel. On the other hand, an absorbing boundary is one where the concentrations of electroactive molecules are invariable. A real life situation for this component is the slipping plane of a moving solution where molecules are constantly recycled.

Diffusion impedance is capable of conveying information about the environment near an electrode's surface depending on how the diffusion pattern and diffusion properties of the electroactive molecules are modified. Similarly, it is anticipated that obstructed diffusion, due to the presence of immobilised analyte bound on the electrode

surface of a biosensor, would alter the diffusion pattern and thus the diffusion impedance. This is the model basis used to characterise the performance of different three-dimensionally shaped electrodes in this work, which exhibits different diffusion patterns and properties due to their distinct geometry.

2.3. Geometric optimisation of impedance biosensor

2.3.1. Electrode geometry and sensor performance

Most of the research in the sensitivity improvement of impedance biosensors has focused on using different electrode constructs so far. This includes the materials that are used to fabricate the electrode and the surface biofunctionalisation [37, 42, 107-109]. The idea that the geometric design of the electrode can affect the performance of an electrochemical biosensor started to get recognised around 1998 with the emergence of advanced micro- and nano-fabrication technologies.

Coplanar interdigitated electrode has been a popular electrode geometry design for electrochemical biosensors [30, 39, 96, 110-113]. The average distance between electrodes can be reduced tremendously by using two comb-like electrodes that interlock with each other. This has a positive effect particularly for non-faradaic mode electrochemical biosensors. Electrical current in a non-faradaic electrochemical system is influenced heavily by the electric field distribution between the two electrodes. The reduced separation of the two interdigitated electrode terminals therefore decreases the overall resistance. Thereby, this increases the overall current throughput of the system, meaning a greater reduction in current can be observed when the analyte of interest binds to the sensor's surface and disrupts the electric field. In addition, interdigitated electrodes have more edges for the same electrode area. Electric field is stronger on

these sharp edges, which means interdigitated electrodes have more binding locations that exhibit strong current density which can enhance the sensor's response [114, 115].

The paper by Van Gerwen et al. was one of the first to formally describe and evaluate the idea of geometric optimisation for electrochemical biosensor with interdigitated electrode using mathematical modelling [111]. They used Schwarz-Christoffel conformal mapping [116] to theoretically calculate the expected current distribution between two coplanar interdigitated electrodes. It was proposed that by concentrating the current flow to the surface of the sensor within a certain height, one can maximise the sensor's sensitivity by maximising the disruption of current path in the presence of bound analytes. They found that, with equal electrode width and inter-electrode spacing, 92% of the total current is confined within a height that is 80% of the width of the electrode. Therefore, smaller electrode dimensions mean the majority of the current is concentrated within a smaller height above the sensor's surface. This indicates the electrode dimensions should be in a similar scale or smaller than the size of the target analyte to achieve near maximal sensitivity.

Laczka et al. applied the same ideas in the development of interdigitated microelectrode biosensor for the bacteria *Escherichia coli* and *Salmonella typhimurium* by probing a change in the non-faradaic current [117]. They fabricated four different interdigitated electrodes of varying electrode width and separation distance, from 30 μm down to 10 μm . They found the smallest electrode dimensions, 10 μm wide electrodes with 10 μm separation, had the best sensitivity in their result. This agreed with the concepts discussed by Van Gerwen et al. Since bacteria are about 0.5 μm in size, electrode should have a similar dimension or smaller to generate the maximal signal change induced by the captured cells. However, the electrodes used in their experiment were at least an order of magnitude bigger. The smallest electrode

dimension was 10 μm , which was closest to the size of the bacteria and thus it exhibited the best sensitivity.

Hoyos-Nogués et al. investigated the detection of periodontopathogenic bacteria *Streptococcus sanguinis* using electrochemical impedance spectroscopy with flat and three-dimensional interdigitated electrodes with non-faradaic mode measurement [118]. The geometry of the three-dimensional electrode consisted of 4 μm high insulating barriers separating the digits of the two electrode terminals. The idea was the electric field between the two terminals would travel more closely to the surface of the raised barriers, which served as binding sites for the bacteria. This means a greater change in impedance can be expected when bacteria are captured. Their experiment results agreed with this theory, demonstrating that the three-dimensional interdigitated electrode gave greater impedance response in comparison to the flat counterpart.

Chen et al. fabricated gold electrode surfaces with pores 500 nm in diameter [119]. The pores were created by embedding the gold surface with silica nanobeads which were later etched away. The electrode was experimented by sensing C-reactive protein using faradaic mode measurement. It was claimed that the macroporous electrode provided a greater surface area that improved the sensor performance by enhancing its conductivity, activity, and binding capacity. However, the performance of the macroporous electrode was not compared to a flat electrode of equivalent surface area.

2.3.2. Finite element method modelling in impedance biosensor research

More advanced fabrication techniques have been developed in the recent decade which allowed researchers to create more complex sensor geometries to further improve their sensor designs. The unique and complicated sensor geometries usually mean the lack of appropriate mathematical models to assist in the characterisation and

optimisation of the sensor designs. Numerical simulation is usually the alternative approach to approximate the properties of the sensors under these situations. The finite element method (FEM) has been particularly popular among researchers of electrochemical devices [120, 121]. FEM is used to solve partial differential equations that describe the physical phenomena of interest on a defined sensor geometry. Instead of analytically solving the problem solution, which is a continuous function of the problem dimension, the method discretises the solution domain into a finite number of element. The model then calculates the solution at each of the elements, and the results are combined together to form the numerical solution of the complete model. An approximation very close to the actual analytical solution can be achieved using sufficiently small elements. The method is particularly efficient for problems involving complex and irregular geometries because the element size can vary across the problem space. A smaller element size can be used to more accurately approximate the solution at locations where the geometry and model solution are more variable, while larger elements are used at invariable positions to solve the problem more quickly. The availability of commercial software packages like COMSOL Multiphysics makes FEM simulation more accessible to researchers [122, 123]. However, expertise is still required from the user to avoid the use of inappropriate modelling configurations and interpreting simulation outputs incorrectly.

Singh et al. designed a three-dimensional interdigitated electrode setup by raising the electrode above the sensor's surface [124]. This created nanometre sized channels between the electrodes. This small separation created very strong current density between the two electrode terminals, and the analytes bind in the cavity to maximise the sensor's response upon immobilisation. They applied FEM simulation to characterise the current density for varying electrode dimensions and found the gap

separation was the main determinant for current density. They used this knowledge to design a sensor and validated its sensing capability by the detection of C-reactive protein.

Das et al. investigated the effectiveness of four different coplanar electrode patterns for macroporous silicon biosensor for *Escherichia coli* detection using non-faradaic electrochemical impedance spectroscopy [125]. Each electrode geometry was evaluated using FEM simulation, and the experimental result aligned with the numerical simulation. They concluded that interdigitated pattern was the optimal electrode geometry and reported a detection limit of 100 CFU/ml for *Escherichia coli*.

The microsquare nanoband electrode was developed by Schmuesser et al. and the electrode was characterised using FEM simulation [49]. The electrode was a nanometre sized band that encircles the bottom edges of a micron-sized square cavity. Fabrication was achieved by laying down a nanometres thick platinum layer sandwiched between silicon compounds. Then a square-shaped cavity was etched into the substrate to reveal the cross-section which has the nanometres wide band of platinum that can be used as the electrode. The fabrication process of the nanoelectrode was said to be reproducible, which is usually very challenging for electrodes of those dimensions. They showed that a relatively large faradaic current can be obtained with a small total electrode area. They attributed this observation to edge diffusion that is prominent for electrodes of such small dimensions. They proposed the use of such electrodes for a sensitive electroanalytical device due to the enhanced reagent diffusion to the electrodes. The sensor design also had low noise levels as noise signals are correlated with the total electrode area.

Some researchers include the immobilised analytes as a part of the numerical simulation. Webster et al. used FEM to simulate the effects of immobilised bacteria on

electrode surfaces for non-faradaic impedance biosensors. They explicitly modelled the captured bacteria electrically using a two-shell model. The bacteria were modelled as a dielectric material with different dielectric permittivities for its cell wall, cell membrane, and cell cytoplasm. Their FEM simulation also suggested a smaller electrode dimension that is close to the size of the bacteria resulted in greater impedance change, agreeing with previous models based on the conformal mapping approximation of the electric field distribution. They also simulated the effects of different permittivity of the suspension medium has on the sensor signal. They observed that suspension medium of lower permittivity may result in a greater signal change in the presence of bacteria. This was mainly because the bacteria model in their simulation had relatively high permittivity. Since the bacteria displace the suspension medium in the current path between the electrode terminals upon immobilisation, the greater difference in permittivity between the bacteria and the suspension medium created a greater change in current signal.

A sensor for distinguishing between viable and dead *Escherichia coli* cells was developed by de la Rica et al. using interdigitated electrodes. The principle of the detection was based on the change in bacteria cell volume after death. The content of the bacteria cell cytoplasm leaks after death, causing the cell to shrink. The smaller volume dead cells disrupts less of the current flow in comparison to the viable cells. Selecting the appropriate electrode geometry allowed 80% of the electric field to be confined within 3 μm above the sensor surface, which enabled the sensor to distinguish between live and dead bacteria. They also characterised the sensor using FEM modelling by simulating the bacteria as rod-shaped dielectric and found good agreement between simulated impedance change and experiment data. One limitation of the method was that the cell concentration of the sample must be known, as a

shrinkage in cell volume due to cell death or the lowering of total cell concentration would both produce a decrease in impedance that is indistinguishable from each other.

Wang et al. investigated the effects of electrode geometry for single-cell measurement microfluidics devices for the HeLa cells [126]. They used FEM simulation to evaluate four electrode geometries based on criteria including electric field uniformity, variations in impedance due to cell position on the electrode, and the overall sensor sensitivity. They selected two electrode designs based on the simulation results and performed experimental validation. They found the experimental findings agreed with the theoretical simulations, supporting numerical modelling as an effective characterisation tool in electrochemical sensor design.

The faradaic electrochemical impedance spectroscopy has shown to be an effective technique in biosensing. However, research in electrode geometric optimisation for electrochemical biosensors has focused mainly on the non-faradaic mode measurement, and similar studies for the faradaic mode measurement have been lacking so far. Additionally, how different three-dimensional electrode shapes affect impedance and sensor performance has not been explicitly compared between different designs. The research reported in this work focused on addressing these knowledge gaps and provide insights to how three-dimensional electrode designs may provide improved biosensor performance.

2.4. Faradaic current in sensing and the effects of three-dimensional electrode geometry

The faradaic process of the electrochemical system has been effectively utilised in biosensing applications [34, 110]. Recognition of target analyte is achieved through their immobilisation on the sensor surface using target specific probes. Typically, this event is correlated with an increase in the measured faradaic impedance. This is explained by the physical obstruction of the electrode surface to the access of electroactive molecules, thus reducing the rate of charge transfer reaction which drives the faradaic current. The faradaic process is modelled by two separate components in the Randles circuit (Figure 2.1), specifically the charge transfer resistance R_{ct} and the diffusion impedance Z_d .

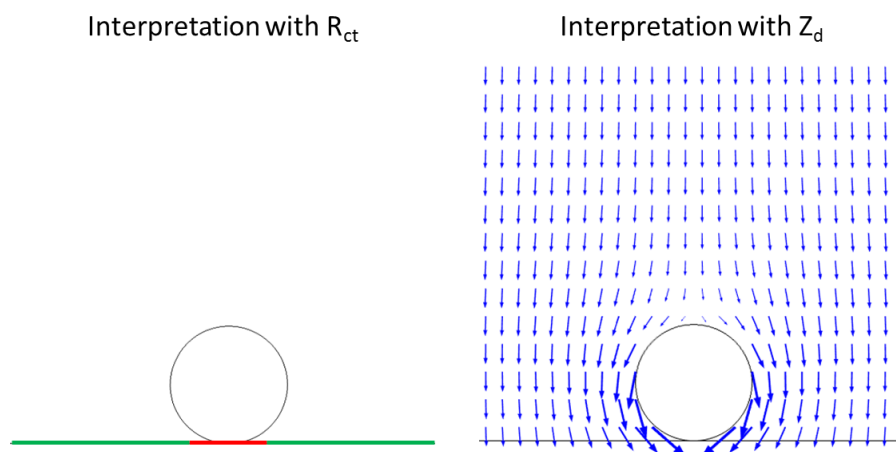


Figure 2.6. Graphical depiction of how charge transfer resistance (R_{ct}) and diffusion impedance (Z_d) models the impedance change upon analyte binding. Left: the presence of analyte blocks access of electroactive molecules to area of electrode highlighted in red. Right: the presence of bound analyte hinders the mass transfer of electroactive molecules shown as blue arrow.

Conventionally, the increase in the R_{ct} component has been used to model and explain the observed impedance increase in response to target immobilisation on the sensor's surface [34]. The component is associated with the transfer of electrons at the surface of the electrode with electroactive molecules that are in close enough proximity to initiate this charge exchange. From Equation 2.9, it can be seen that R_{ct} is dependent on the concentration of electroactive molecule at the electrode surface and also the effective electrode area. Consequently, the increase in R_{ct} upon analyte binding can be explained in two ways. First, the immobilised target analyte causes a decrease in electrode area that is accessible for the faradaic reaction to occur (Figure 2.6, left). Second, the presence of the captured analyte displaces the electroactive molecules and thus decreases the average concentration of the molecules near the electrode surface. Either approach of explanation leads to decreased faradaic reaction rate and increased faradaic impedance.

The charge transfer process is an interfacial process; it describes the rate of charge movement across the electrode-solution interface, which is a two-dimensional plane. A possible way of applying this component in predictive modelling for sensing applications is by assigning an area of influence per bound analyte. Each unit of bound analyte causes a specified area of the electrode to lose its electroactivity. However, this creates limitation in simulating processes that happen beyond the electrode surface. Electrode geometry has effects on the diffusion pattern of molecules in the three-dimensional space beyond the electrode surface. Electrodes with the same area in the same chemical environment will theoretically have the same charge transfer rate. However, the efficiency of diffusion may change when the electrode geometries are different. This can modulate the overall rate of the faradaic process, despite having the same electrode area. For instance, it is known that electrodes with micrometre and

nanometre dimensions exhibit enhanced current in comparison to macro electrodes on a per unit area basis. The reason for this observation is the more efficient radial pattern of charge movement that operates within sub-micron electrodes, which is a phenomenon that happens beyond the electrode-solution interface and cannot be adequately modelled with charge transfer resistance. Another example is the effect of electrode three-dimensional geometry on the faradaic current investigated in this work. Different electrode geometries can exhibit different rates of faradaic process due to the different diffusion patterns associated with it, despite having the same electrode area. Therefore, the previously described modelling approach using charge transfer resistance does not encapsulate the effects of electrode geometry has on diffusion rate. An alternative modelling approach is needed for this purpose, and the most obvious option is to use the diffusion impedance.

The diffusion impedance component has been largely ignored in research related to biosensing applications so far. It has not been used to explain the change in electrode impedance upon analyte binding. Usually, a standard diffusion impedance model may be used as a part of the data fitting procedure, but changes in the diffusion impedance are never interpreted as a part of the result. A possible physical explanation involving the diffusion component may be the presence of analyte blocks the movement of electroactive species from the bulk solution to the electrode surface (Figure 2.6, right). This in turn decreases the amount of electroactive molecules reaching the electrode surface to initiate electron exchange and thereby decreases the faradaic current.

Most electroactive species used in biosensing are hydrophilic and therefore are expected to be unable of penetrating, for example, the cell membranes of bacteria. This means the diffusion of the electroactive species would be blocked by such target analytes [110]. A complication is that some cells can exhibit redox proteins in their

cytoplasmic membrane, which can convert the redox molecules to the reduced form [127-129]. This can potentially change the redox mediator concentrations in the vicinity of the cells. However, this effect is beyond the scope of this work.

The diffusion of molecules occurs over space, and the flux of molecules can be conveniently modelled in three-dimensional geometries. Models of the electroactive molecules diffusion have been done previously in the analyses for micro-electrodes [49, 130]. The radial diffusion patterns observed with these electrodes are advantageous for electroanalytical applications due to the enhanced rate of faradaic process. These are example showing how electrode geometry can affect the faradaic process via change in diffusion property. Therefore, we sought to investigate how different diffusion patterns associated with different electrode geometries have an influence in biosensing applications.

Diffusion impedance is dependent on a physical process that is distinct to charge transfer resistance. Therefore, the preliminary investigation in this study was done on how diffusion impedance is involved and whether its model can be applied in biosensing applications. The study considers target analyte of micrometre scale. Real world examples of micron-sized analytes include whole cells of common bacteria. In addition, polystyrene microbeads are often used in electrochemical biosensors [69, 131]. Finite element method was employed as the numerical modelling technique to assist with understanding how the diffusion process is involved in sensing. Subsequently, this knowledge is applied in investigating the effects of three-dimensional electrode geometry in biosensing.

3. Modelling Diffusion Impedance in the Detection of Micron-sized Targets

3.1. Introduction

The change in charge transfer resistance is the conventional indicator for analyte recognition in faradaic impedance biosensors, however, it is not sufficient in reflecting the influence of three-dimensional electrode geometry on the faradaic process. Therefore, an alternative model based on the diffusion impedance is to be developed. This chapter details the investigation of how the diffusion of electroactive molecules contributes to the change in electrode impedance upon analyte immobilisation. The effect of such process in biosensing applications has not been explored in research thus far. The model developed in this chapter would be used to characterise and study the influence of three-dimensional electrodes on faradaic mode impedance biosensors.

The model system selected for this purpose was a flat electrode in semi-infinite bulk medium. Micron-sized polystyrene (PS) bead was the target analyte of the model. Firstly, numerical simulation of the effects of surface immobilised beads on diffusion impedance is presented to provide a general understanding about the underlying process and impedance change. Subsequently, experimentally collected impedance data are analysed and compared to the simulation for model validation.

3.2. Finite element simulation

Theoretical investigation into the effects of blocked diffusion due to immobilised micro-particles was performed by analysing the change in impedance. This was done by solving Fick's second law of diffusion to simulate the diffusion impedance in the

presence of different densities of surface immobilised beads. The results were compared to the Warburg element, i.e. the diffusion impedance of bare electrode without any obstruction. A numerical approach was taken to solve for the diffusion impedance as the complex geometry involved in the model made it impossible for the solution to be obtained by analytical means. Finite element method (FEM) was selected for this purpose, which was useful for models with complex geometries such as the ones involved in this study.

COMSOL Multiphysics software package and its Electroanalysis module were used to facilitate the modelling process. The goal was to provide a qualitative understanding of how diffusion impedance changes in response to immobilised micro-particles on the electrode surface.

3.2.1. FEM model setup

3.2.1.1. Calculating the diffusion impedance using FEM simulation

FEM was used to calculate the diffusion impedance by solving Fick's second law of diffusion (Equation 3.1). The numerical method solved for the concentration profile of chemical species k at user specified excitation frequencies. The excitation was setup as a harmonic voltage perturbation v of 10 mV amplitude, implemented as a boundary condition at the electrode surface.

$$\nabla \cdot -D_k \nabla c_k(\mathbf{r}, \omega) = \nabla \cdot \mathbf{J}_k(\mathbf{r}, \omega)$$

(Equation 3.1)

c_k : concentration of chemical species k ($\text{mol} \cdot \text{m}^{-3} \equiv \text{mM}$)

D_k : diffusion coefficient of chemical species k ($\text{m}^2 \cdot \text{s}^{-1}$)

\mathbf{J}_k : molecule flux density vector of chemical species k ($\text{mol} \cdot \text{m}^{-2} \cdot \text{s}^{-1}$)

\mathbf{r} : position in model space

ω : angular frequency of excitation signal ($\text{radians} \cdot \text{s}^{-1}$)

$$i(\omega) = \frac{nFJ_k^0(\omega)}{\nu_k}$$

(Equation 3.2)

J_k^0 : total flux of chemical species k at the electrode surface ($\text{mol} \cdot \text{s}^{-1}$)

i : total current generated at the electrode boundary (A)

F : Faraday constant

n : number of electrons involved in the charge transfer reaction

ν_k : stoichiometric number of chemical species k in the redox reaction

$$Z(\omega) = \frac{v(\omega)}{i(\omega)}$$

(Equation 3.3)

The calculated concentration profile allowed the molecular flux density J_k at any point in the model space to be determined from concentration gradient. The total flux through the electrode J_k^0 could be obtained by integrating the flux through the electrode surface over the entire electrode area. This total flux was converted to an equivalent electrical current (Equation 3.2). Assuming there is only one redox reaction equilibrium involved in the system, the diffusion flux for one of the redox species only is needed to calculate the total current. This is because the simultaneous diffusion of all species (reactants and products) drives the transfer of n electrons. This resulting current i is the simulated current response upon the 10 mV amplitude sinusoidal voltage excitation. The impedance is therefore the ratio between the specified voltage excitation v and the simulated current response i (Equation 3.3).

3.2.1.2. Model setup and parameters

The electroactive chemical species considered in this study was the ferrocyanide/ferricyanide redox couple ($n = 1$, $v_R = -1$, $v_O = 1$). The diffusion coefficient for both molecules were approximated to $7.5 \times 10^{-10} \text{ m}^2 \cdot \text{s}^{-1}$ for simplicity [132]. The bulk concentration for both were specified as $5 \text{ mol} \cdot \text{m}^{-3}$ (equivalent of 5 mM). All instances of temperature values in equations or model parameters were approximated with a room temperature of 293.15 K (20°C).

The target PS particle was modelled as a micron-sized sphere in the FEM simulation. The PS particles are dense and exclude most water, the electroactive molecules are not able to freely move through them. Therefore, the spheres were implemented as impenetrable to the movement of electroactive molecules. The spheres had a diameter of 0.7 μm .

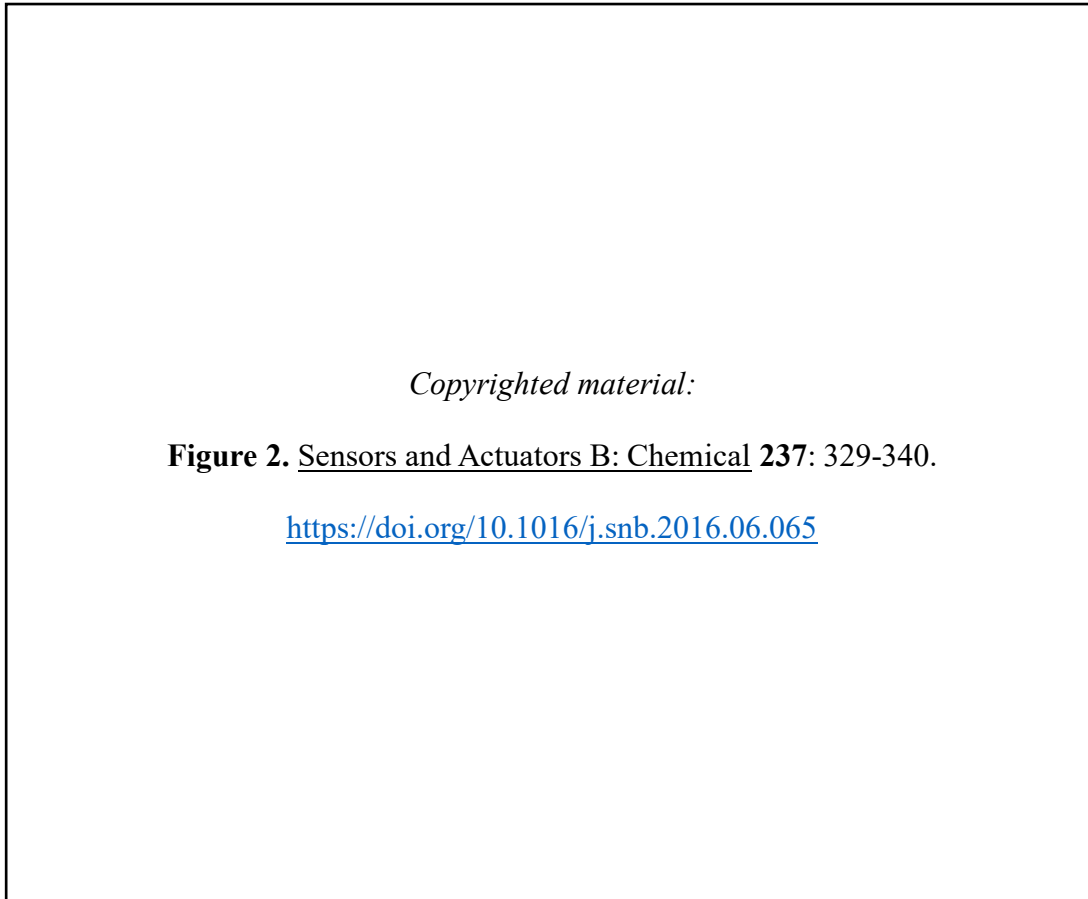


Figure 3.1. A) The modelled geometry of the electrode (bottom plane) and bound particles (spheres). B) Plot showing the sum of magnitude of diffusion flux density in the x and y directions $|J_x| + |J_y|$ at the xy plane 0.35 μm above the electrode surface (0.5 Hz excitation). C) Diagram illustrating the calculation of surface coverage. All values and variables have unit in μm . D) The actual geometry used in the FEM simulation after model space reduction by symmetry.

The spherical particles were positioned evenly across the electrode surface as depicted in Figure 3.1A. The model assumed the condition of semi-infinite bulk volume above the electrode in the z direction. The ceiling boundary had fixed ferrocyanide and ferricyanide concentrations equal to their bulk concentrations to simulate the bulk solution. The lowest simulated frequency of excitation was 0.1 Hz, which corresponded to a characteristic distance of $\sim 35 \mu\text{m}$. Consequently, the modelled space extended 500 μm above the electrode surface to minimise any absorbing boundary effect imposed by the ceiling boundary. This was to uphold the assumption of semi-infinite diffusion.

Symmetry was exploited to simplify the modelled space. The diffusion pattern around each analyte particle was identical due to their regular distribution, therefore the simulation could be done for one unique section (unit cell) and the result extended to a greater area of the same particle coverage density. Figure 3.1B shows that there is no diffusion of electroactive molecules in the x and y directions at midpoints between each particle, as denoted by the dark blue colour in the figure. This means simulation could be performed as depicted in Figure 3.1C since the region represented a geometry that was repeated over the whole model. The newly created model boundaries (periodic boundaries) as a result of simplifying the model from Figure 3.1A to Figure 3.1C would be positioned at these planes that had no diffusion in the x or y directions. Therefore, the new boundaries could be implemented as blocking boundaries without changing the diffusion pattern after model reduction. The rotational symmetry around each particle allowed for further simplification down to a quadrant as shown in Figure 3.1D. The simplification significantly reduced the size of the model space, which allowed for more accurate solutions to be obtained with lower degrees of freedom and a shorter simulation time.

Simulation of diffusion impedance was performed with different percentages of particle coverage on the electrode surface ($X\%$). The diffusion impedance for a specific coverage is symbolised as $Z_d X\%$. Coverage was defined as the ratio between the maximum horizontal cross-sectional area of the spherical analyte and the electrode area as depicted in Figure 3.1C. The model space dimension L was varied according to the percentage coverage modelled. A higher percentage coverage was equivalent to a higher density of bound particles.

The simulation also required configuration of parameters that defined the relationship between electrode potential and the rate of charge transfer. Since an arbitrary finite electron transfer rate constant (7×10^{-5} m/s) was used, this created a charge transfer resistance component that was included within the final simulation output. As the charge transfer resistance was not a part of this investigation, its value ($7.6043 \times 10^{-4} \Omega \text{m}^2$) was determined from the arbitrary reaction coefficient using Equation 2.9 and subtracted from the simulation output.

3.2.1.3. Model verification

The accuracy of finite element models is strongly influenced by its mesh [122]. Therefore, mesh refinement is of critical importance for obtaining reliable simulation results. Both h-refinement and p-refinement were performed. H-refinement involves improving solution accuracy by using finer mesh, while p-refinement uses higher order polynomials to more fittingly approximate the solution. Firstly, h-refinement study was performed with linear tetrahedral elements by halving the size of the mesh elements at the electrode surface until the changes in simulated impedance values were less than 0.5% at all frequencies between refinement steps. Next, p-refinement was attempted using quadratic tetrahedral elements. However, the simulation using higher order

tetrahedral elements did not change the simulated result very much. Therefore, the final mesh setup after mesh refinement study consisted of linear tetrahedral elements of smaller than 10 nm in size on the electrode surface and grew at a rate of 1.03 towards the bulk solution.

The FEM generated numerical solutions were verified against the analytical solutions for semi-infinite planar diffusion pattern (Warburg element) and radial diffusion patterns (cylindrical and spherical [105]) to ensure the implemented model was accurate. The deviations between the numerical solutions and the analytical equations were less than 0.5% at all simulated frequencies.

Copyrighted material:

Figure 5A. *Sensors and Actuators B: Chemical* **237**: 329-340.

<https://doi.org/10.1016/j.snb.2016.06.065>

Figure 3.2. Nyquist plot of diffusion impedances of the bare electrode and particle bound electrodes with different percentages of coverage (10%, 25%, and 50%).

3.2.2. FEM simulation results

3.2.2.1. FEM simulation of diffusion impedance with micro-particle obstruction

The simulated diffusion impedance $Z_{d,X\%}$ at three different percentages of electrode coverage ($X\%$) are plotted with the diffusion impedance of the bare electrode (Warburg element) in Figure 3.2. The plot shows that the diffusion impedance does not change significantly at high frequencies (bottom left of the Nyquist plot), but shows a general increase in the real component with higher particle coverage at lower excitation frequencies.

The differences in the real ($\Delta Z_{d\ x\%}'$) and imaginary ($\Delta Z_{d\ x\%}''$) components of the diffusion impedance with particle obstructions from those of the Warburg element (Z_{Warburg}' and Z_{Warburg}'') are shown separately in Figure 3.3. The differences are calculated according to Equation 3.4. The data are plotted for frequencies below 100 Hz, as this is the typical frequency range where the diffusion impedance is observable in experimentally measured impedance spectra. The real component appears to have a relatively even increase in magnitude within this frequency range for each percentage of coverage. In contrast, the increase in the magnitude of the imaginary component shows a positive correlation with frequency. The real component demonstrates greater difference than the imaginary component in general, however, the change in the imaginary component becomes more significant towards higher frequencies.

$$\begin{aligned}\Delta Z_{d\ x\%}'(\omega) &= Z_{d\ x\%}'(\omega) - Z_{\text{Warburg}}'(\omega) \\ \Delta Z_{d\ x\%}''(\omega) &= Z_{d\ x\%}''(\omega) - Z_{\text{Warburg}}''(\omega)\end{aligned}$$

(Equation 3.4)

Copyrighted material:

Figures 5B (top) & 5C (bottom).

Sensors and Actuators B: Chemical **237**: 329-340.

<https://doi.org/10.1016/j.snb.2016.06.065>

Figure 3.3. $\Delta Z_{d \ x\%}'$ (top) and $\Delta Z_{d \ x\%}''$ (bottom) for different particle coverage densities for frequencies below 100 Hz.

3.2.2.2. The effects of diffusion distance in sensing

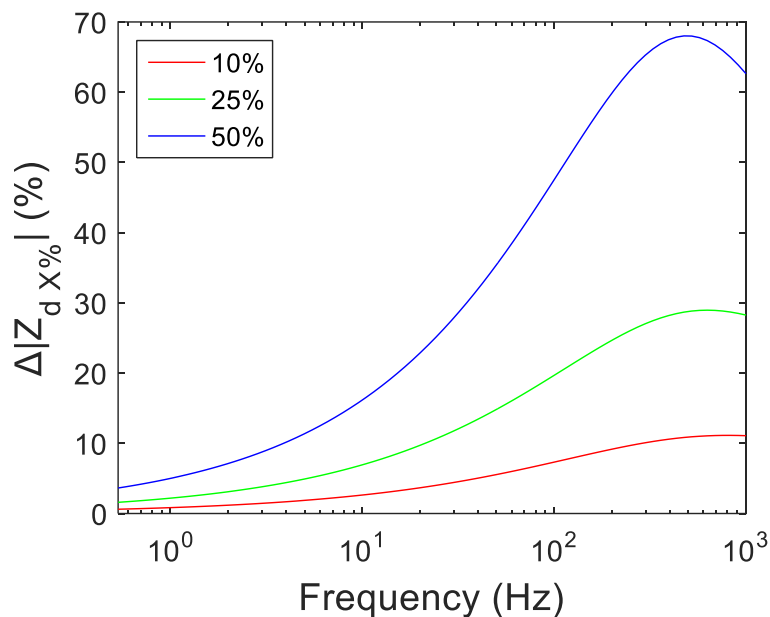


Figure 3.4. The percentage change in the magnitude of the diffusion impedance for different percentages of particle coverage from the Warburg element. The data is plotted for frequencies 1 kHz and below with the frequency axis in log scale.

Figure 3.4 shows the percentage change in the magnitude of the diffusion impedance in response to different percentages of particle coverage. The maximum relative change in the magnitude as seen from the plot is around 500 Hz. This frequency equates to a characteristic distance of around 0.49 μm , which is comparable to the size of the modelled PS bead with diameter of 0.7 μm . This is because a greater proportion of the diffusion pattern is obstructed when the diffusion distance matches with the dimensions of the analyte particle. However, diffusion impedance is normally unobservable at such high frequencies due to the dominating non-faradaic current path under such condition. Therefore, a more sensitive sensor signal in response to the presence of immobilised analyte is expected to be obtainable from analysing the

electrode impedance at the highest frequency where the diffusion impedance can be observed reliably.

Figure 3.5A illustrates the diffusion pattern in the presence of particle obstructions at low excitation frequency. The long diffusion distance at low frequency means the majority of the diffusion occurs above the immobilised beads and are undisturbed. The increase in the magnitude of the real component dominates over the imaginary component in this situation. This increase in the real component of the diffusion impedance is analogous to the increase in charge transfer resistance used conventionally to interpret the data for faradaic mode impedance biosensors. The two models appear especially similar when the high frequency part of the diffusion impedance is unobservable due to the parallel non-faradaic process dominating in the sensor readout. Therefore, either the increase in charge transfer resistance or the change in diffusion impedance may be used to fit the same experiment impedance spectrum adequately when the higher frequency section of the faradaic impedance is obscured by the non-faradaic component.

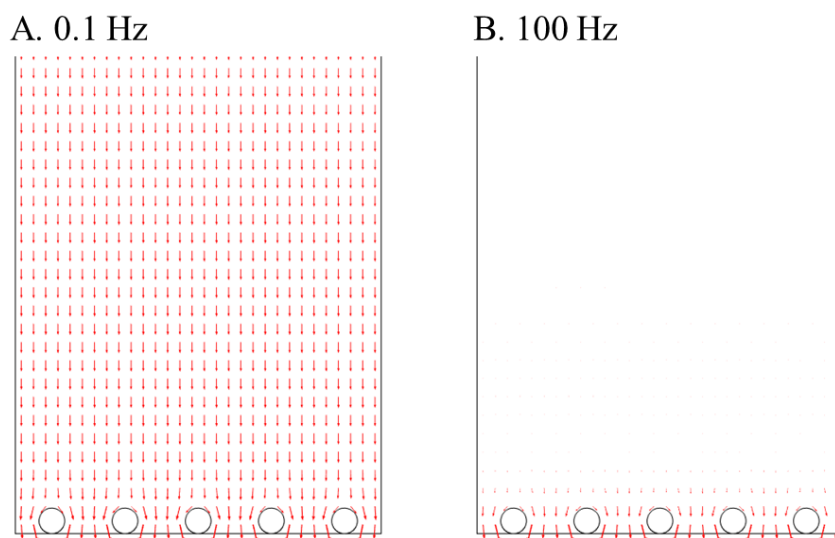


Figure 3.5. The diffusion patterns for 0.1 Hz (A) and 100 Hz (B) excitatioin signals

In contrast, the shorter diffusion distance at higher excitation frequency means the majority of the diffusion occurs at a similar scale to the size of the analyte (Figure 3.5B). The diffusion impedance at this higher frequency range shows the more intricate changes, which reflect the disturbed diffusion pattern due to the presence of PS beads. The change in diffusion distance is no longer dominated by a simple increase in the real component at these higher frequencies, implying that the conventional model of increase in charge transfer resistance alone cannot be used to fully replace the diffusion impedance change suggested by the simulation. In reality, both components may contribute to the overall change in the electrode impedance in the presence of surface bound micro-particles.

The observations from the theoretical simulated diffusion impedance in response to micron-sized particle obstructions are compared to experimentally acquired impedance data for model validation in the next section.

3.3. Experimental impedance measurement in the presence of polystyrene beads

3.3.1. Experiment procedure

3.3.1.1. Experiment design

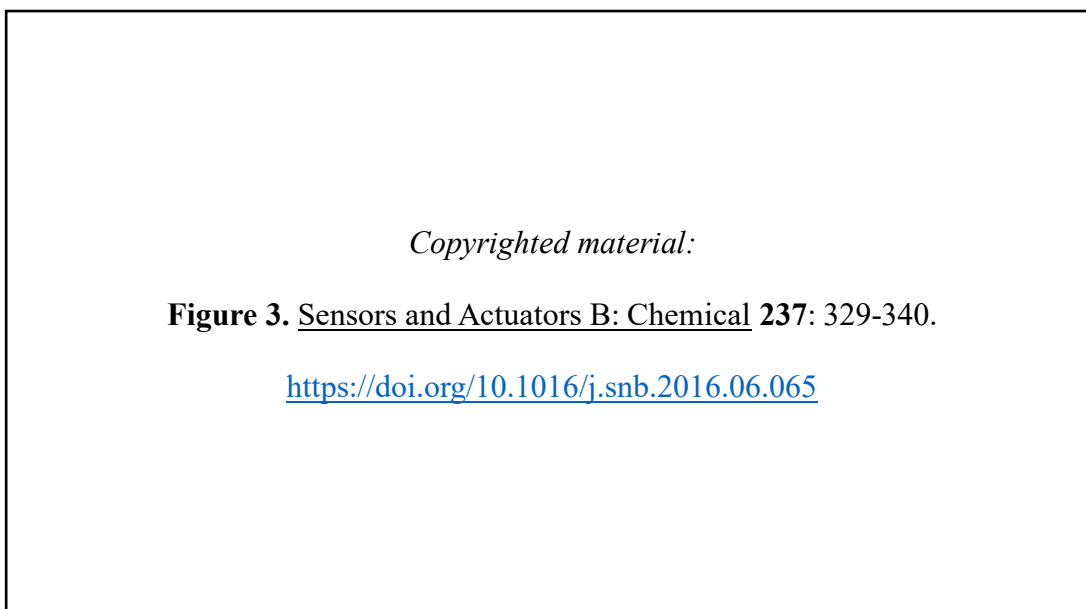


Figure 3.6. Graphical illustration of the experiment setup. Components are not drawn to scale

Sensing experiment was performed to validate the numerical model presented in the previous section. The gold working electrode was fabricated by sputter coating a gold layer onto flat polyethylene terephthalate glycol-modified (PETG) substrates using Nano36 sputtering system (Kurt J. Lesker Company). A fluid compartment was created above the working electrode by clamping down a Teflon well to the gold surface and sealed by a rubber O-ring in between as shown in Figure 3.6. The rubber O-ring had an inner diameter of 9 mm, which gave a circular working electrode with an area of ~ 64 mm². All electrochemical experiments were performed in the three-electrode

configuration, involving the gold working electrode, a Ag/AgCl reference electrode (eDAQ), and a platinum counter electrode (eDAQ). All reported working electrode potentials are relative to the Ag/AgCl reference electrode.

Since the faradaic component was the focus of this study, a relatively faster faradaic process would allow the diffusion impedance component to be extracted from the total electrode impedance unambiguously up to higher frequencies. This would improve the confidence of the analysis on the diffusion impedance. Polypyrrole conducting polymer was chosen as the functional layer due to its high charge transfer rate across the surface-solution interface with the ferrocyanide/ferricyanide redox couple [37, 42, 133, 134]. Previous work has suggested that the charge transfer resistance of the electrodes reduced after deposition of polypyrrole conducting polymer on glassy carbon electrodes, possibly owing to its rough surface for providing a greater surface area for faradaic charge exchange to occur.

Biotin-coated PS micro-particle was the target analyte. Avidin-biotin interaction was used to immobilise the PS beads onto the electrode surface [135]. The gold working electrode was deposited with carboxylic acid group functionalised polypyrrole conducting polymer, which allowed for the anchoring of avidin probes on the polypyrrole polymer surface using carbodiimide crosslinking chemistry. This provided a surface for binding the biotin-coated PS beads.

3.3.1.2. Preparation of polypyrrole conducting polymer

The gold working electrode surface was rinsed with ethanol at the start of each experiment. Next, the electrode underwent electrochemical cleaning by potential cycling between -0.4 V and 1.8 V in 0.5 M nitric acid until a stable reduction peak was obtained [136].

Deposition of the polypyrrole conducting polymer on the cleaned gold electrode surface followed the reported process in [37]. The pyrrole monomer solution was made up with a mixture of 50 mM poly(styrene sulphonate) dopant, 5 mM distilled pyrrole, and 0.5 mM pyrrole-3-carboxylic acid (PCA) diluted in deionised water. This gives a pyrrole to PCA monomer ratio of 10:1. The monomer solution was then sparged with nitrogen gas to remove oxygen. Electropolymerisation of the monomers on the gold electrode surface was induced by applying a constant potential step of 0.8 V for 0.5 seconds while submerged in the monomer solution.

3.3.1.3. Attachment of avidin probe and immobilisation of PS beads

Avidin probes were covalently attached to the carboxylic acid functional groups of the conducting polymer layer using carbodiimide crosslinking chemistry. Activation of the carboxylic acid groups on the polypyrrole conducting polymer was achieved by incubating the polymer surface with 50 mM EDC (1-ethyl-3-(3-dimethylaminopropyl)-carbodiimide) and 25 mM NHS (N-hydroxysuccinimide) in phosphate-buffered saline (PBS) (Sigma-Aldrich) adjusted to pH 5.6 for 1 hour in room temperature. Next, the activated surface was rinsed with PBS and then incubated with avidin (Sigma-Aldrich) at a concentration of 0.5 mg/mL in PBS (pH 7.4) in room temperature for 1 hour. The unattached avidin was washed away with PBS afterwards. The immobilisation of analyte was performed by incubating the probed electrode surface with the biotin-coated PS beads (Spherotech, mean diameter 0.74 μm), suspended in PBS (pH 7.4) at the desired concentration, for 1 hour in room temperature. Impedances were recorded before and after incubation of the PS beads to assess how the presence of surface immobilised beads changed the electrode impedance.

Impedance drift over time creates problems with the reliability of data interpretation for electrochemical impedance sensors [74]. Therefore, the impedance data for each experiment were collected with a new electrode each time with the identical incubation steps, i.e. the same electrode was not incubated with incrementing beads concentrations to collect multiple data points. This minimises the contribution of impedance drifts over time when comparing between data points.

3.3.1.4. Impedance measurement and beads coverage estimation

SP-300 potentiostat from Bio-logic was used to measure impedance. All impedance measurements were performed in a solution containing 5mM/5mM potassium ferrocyanide/ferricyanide redox couple in PBS supporting buffer (pH 7.4). The applied sinusoidal voltage excitation had 10 mV amplitude and a DC bias potential equalled to the open-circuit potential of the electrode system, which was typically around 230 mV. The main electrolyte in PBS were Na⁺ and Cl⁻ ions at the concentration of 140 mM each. This concentration was much higher than that of the ferrocyanide/ferricyanide redox couple, and the ions were non-electroactive. Thus, the mass transport of the electroactive molecules was approximated with a purely diffusion process, ignoring any electrostatic effects.

Each electrode was inspected with scanning electron microscopy after the sensing experiment to inspect the immobilised micro-beads. The surface coverage by PS beads for each electrode was deduced by counting the number of bright pixels in the image, which reflected the bound PS beads (Figure 3.7A). This was performed automatically with an implemented software with adjustable brightness threshold. An area of ~1000 μm^2 was analysed for each electrode to calculate an approximation for the averaged beads coverage. Noises in the image were removed by ignoring lone bright pixels, i.e.

those without other bright pixels immediately adjacent to them. The estimated surface coverage for each incubated PS beads concentration is summarised in Figure 3.7B.

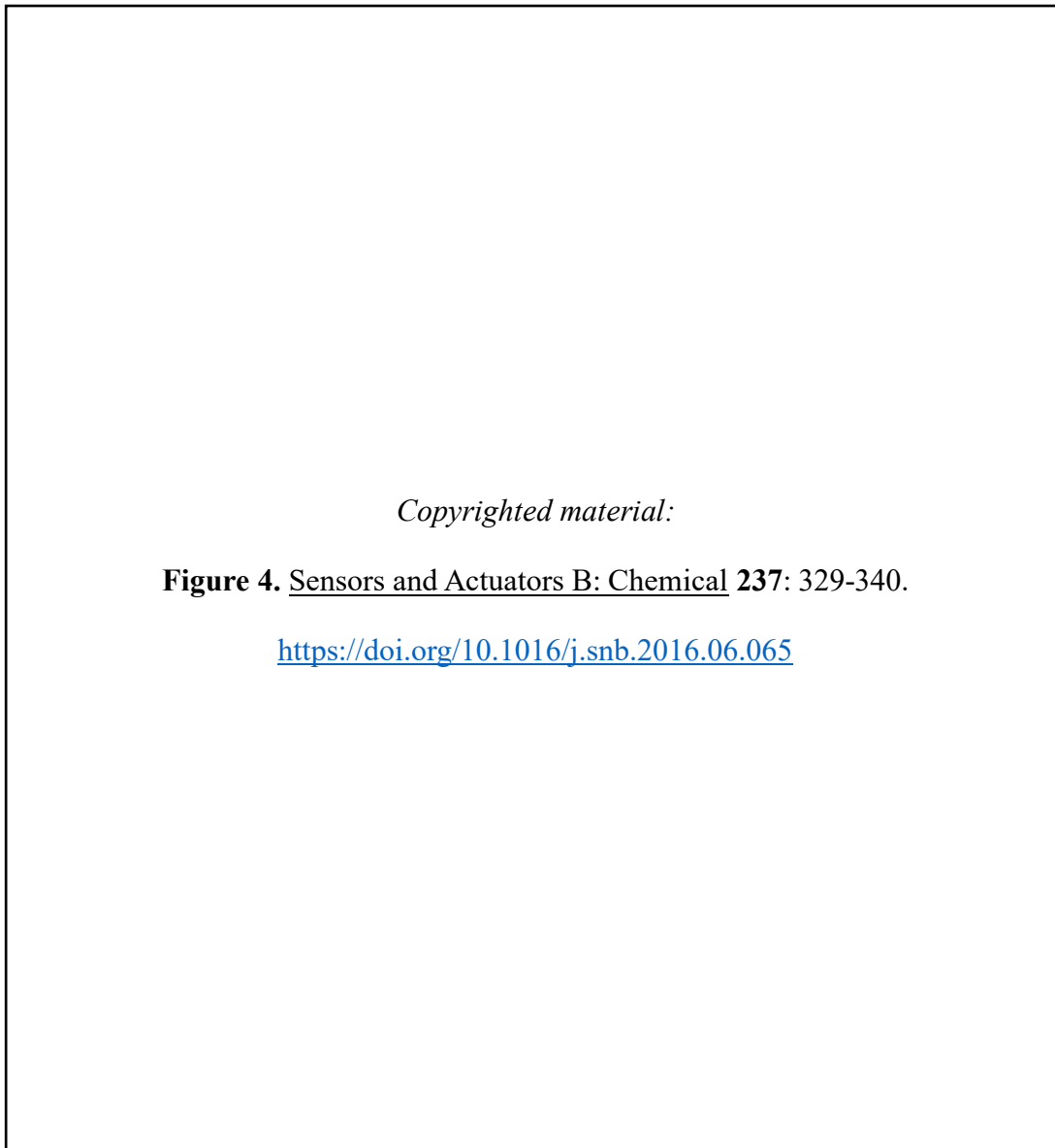


Figure 3.7. A) An example of the implemented software deducing the surface coverage of an electrode after PS beads incubation. Red pixels demarcate regions recognised as PS beads. This electrode had a coverage of 10%. B) The relationship between percentage of electrode coverage and incubated PS beads concentration. The error bars are 95% confidence intervals based on Student's t-distribution of sample size 3.

3.3.1.5. Verifying the probe attachment and analyte binding chemistry

The probe attachment and analyte binding chemistry was checked by performing the following experiments with the result summarised in Table 3.1. Firstly, the polypyrrole conducting polymer was deposited using 10:1 pyrrole/PCA ratio, and carbodiimide crosslinking chemistry was conducted to attach the avidin probes. The electrode surface was incubated with 0.05% w/v biotin-coated and non-coated PS beads. Only the biotin-coated PS beads bound to the surface, suggesting the biotin was necessary for the binding chemistry. Secondly, the surface was prepared without attachment of the avidin probes. Neither biotin-coated nor non-coated PS beads were captured on the sensor's surface in this case, suggesting a requirement for the avidin probes. Lastly, the process was performed with a polymer composed of pure pyrrole without carboxylic acid functional group. Again, the result showed no binding of either biotin-coated or non-coated PS beads, suggesting that the carboxylic acid functional groups were necessary for the attachment of the avidin probes. These evidences taken together suggested that the probe attachment and probe-analyte binding chemistry worked as expected.

TABLE 3.1. IMMOBILISATION OF POLYSTYRENE BEADS FOR DIFFERENT ELECTRODE BIOFUNCTIONALISATION

	Non-coated PS beads	Biotin-coated PS beads
Pyrrole/pyrrole-3-COOH copolymer (ratio 10:1) Deposited avidin probes		
Pyrrole/pyrrole-3-COOH copolymer (ratio 10:1) No avidin probe		
Polypyrrole polymer Deposited avidin probes		

3.3.2. Model validation

3.3.2.1. Model fitting with Warburg element (planar diffusion)

The experimentally collected impedance spectra before and after the immobilisation of PS beads were fitted to different models of diffusion impedance. The electrode used in the experiment was flat, and its dimension (9 mm diameter) was much greater than the characteristic diffusion distances involved in the experiment (<50 μm). This meant the majority of diffusion pattern was semi-infinite planar diffusion, except at the edge of the electrode due to imperfect 90° wall created by the rubber O-ring seal.

The deposited polypyrrole film thickness was estimated using the total charge passed during electrodeposition [37, 137]. The nominal film thickness was determined to be in the order of ~1 nm. This meant the surface roughness created by the conducting polymer would be in a similar scale, which was much smaller in comparison to the size of the PS beads and the diffusion distances involved in the experiment. Therefore, the roughness of the conducting polymer layer was assumed to not invalidate the assumption of a flat electrode surface, as the majority of the diffusion would occur far beyond the polymer layer. Similarly, the avidin probes on the polymer surface had size in the order of a few nanometres [138], which was not expected to significantly influence the planar diffusion pattern.

$$Z_{Randles}(\omega) = [Z_{dl}(\omega)|(Z_{Warburg}(\omega) + R_{ct})] + R_{sol} \quad (\text{Equation 3.5})$$

$$Z_{dl}(\omega) = \frac{1}{(j\omega)^\alpha Q_{dl}} \quad (\text{Equation 3.6})$$

Copyrighted material:

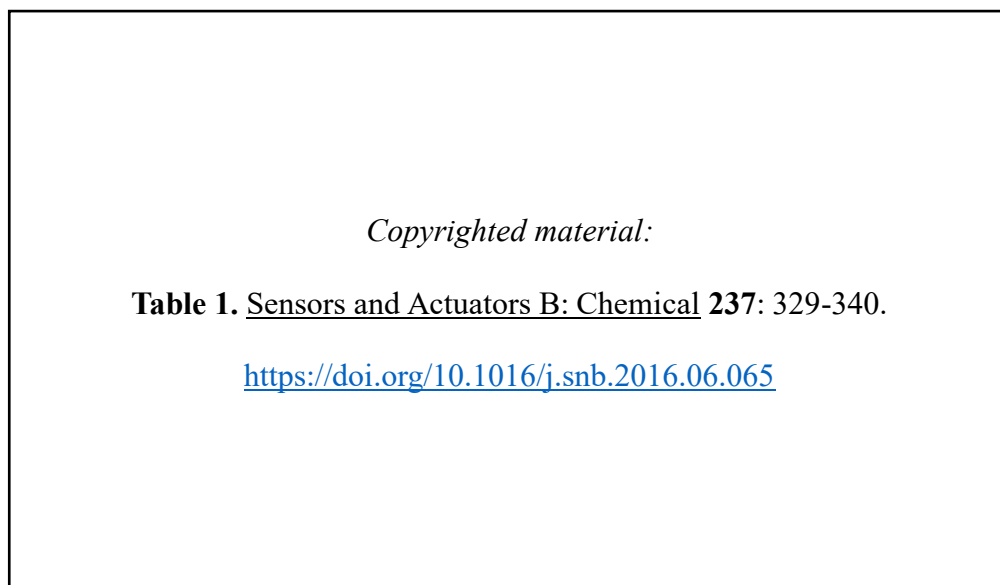
Figure 6. Sensors and Actuators B: Chemical **237**: 329-340.

<https://doi.org/10.1016/j.snb.2016.06.065>

Figure 3.8. Model fitting of Randles circuit, using Z_{Warburg} as diffusion impedance, to the impedances of an electrode measured before (A) and after (B) PS beads incubation. This electrode had a coverage of 47% after PS beads incubation. The frequency range of the Nyquist plots is 10 kHz to 0.5 Hz.

A representative impedance for an electrode with deposited polypyrrole conducting polymer and avidin probes on its surface is shown in Figure 3.8A. The impedance spectrum was fitted to a Randles circuit model using the Warburg element as the diffusion component. The non-linear curve fit function in MATLAB was used to perform the model fitting according to the circuit equation described by Equation 3.5. The parallel double layer capacitance of the non-faradaic current path was modelled with a constant phase element Z_{dl} (Equation 3.6) instead of an ideal capacitance [102]. The use of polypyrrole functional layer resulted in having more than 90% of the total current through the faradaic path at frequencies below 100 Hz, as estimated from the component values of the fitted Randles circuit (Table 3.2). The large faradaic current allowed the diffusion impedance to be observed unambiguously.

TABLE 3.2. RANGLES CIRCUIT MODEL FITTING TO EXPERIMENTAL IMPEDANCE USING $Z_{WARBURG}$ OR FEM SIMULATED $Z_{D47\%}$ AS DIFFUSION IMPEDANCE



The impedance spectrum exhibited the 45° sloped line at the low frequency section, which was representative of a diffusion impedance that was governed by the semi-infinite planar diffusion of electroactive molecules. The result of model fitting (Table

3.2) gave an observed D_s of $7.6 \times 10^{-10} \text{ m}^2 \text{ s}^{-1}$, which was comparable to the diffusion coefficient values reported for the ferrocyanide/ferricyanide redox couple from other sources (5.1×10^{-10} – $7.8 \times 10^{-10} \text{ m}^2 \text{ s}^{-1}$) [132, 139]. The variations in the value could be the result of different ions species and concentrations of the supporting electrolyte. These observations taken together suggested that the electrode impedance observed at low frequencies was governed primarily by the semi-infinite planar diffusion of the ferrocyanide/ferricyanide redox pair. The close fit between experiment data and the Randles circuit model using Warburg element as the diffusion impedance component (residual sum of squares RSS = 0.92) suggested the diffusion pattern was indeed semi-infinite and planar as far as observable from the recorded electrode impedance. The avidin and polypyrrole layers did not have a significant effect on the diffusion pattern at the frequencies where diffusion impedance was observable.

After confirming that experimental diffusion impedance reflected semi-infinite planar diffusion of the ferrocyanide/ferricyanide redox couple, we examined how well the Warburg element agreed with the diffusion component of the observed electrode impedance in the presence of captured PS beads. The impedance of the same electrode after incubation with biotin-coated PS beads is shown in Figure 3.8B. This electrode had a surface coverage of 47%. This electrode impedance with immobilised PS beads was fitted to the same Randles circuit using Warburg element as the diffusion impedance. The result of the model fitting gave much poorer fit with an RSS value of 9.64 (Table 3.2). This observation suggested that Randles circuit with Warburg element as the diffusion component was insufficient in fully describing the impedance change in response to surface immobilised PS beads.

3.3.2.2. Method of model fitting with FEM simulated diffusion impedance

$$Z_{Randles}(\omega) = [Z_{dl}(\omega)(Z_{d\ x\%}(\omega) + R_{ct})] + R_{sol}$$

(Equation 3.7)

Next, we attempted to include the FEM calculated diffusion impedance, which simulated the effects of surface immobilised beads, into the Randles circuit model to examine whether this would improve the agreement between the model and experiment data. The Warburg element component in the Randles circuit was replaced by the FEM simulated diffusion impedance at $X\%$ of PS beads coverage $Z_{d\ x\%}$ (Equation 3.7). The percentage coverage used in the FEM simulation was equal to the coverage estimated from scanning electron microscopy photos of the electrode for which the impedance data was fitted to. The diffusion coefficient of the simulated diffusion impedance was allowed to vary for data fitting in a similar fashion as when Warburg element was used.

FEM models the diffusion impedance at a particular user defined diffusion coefficient D value. As there is no analytical equation to describe the altered diffusion impedance in the presence of PS beads, to obtain the impedance at different D values for model fitting normally involves performing the simulation repeatedly at different D values until an adequate data fit can be obtained. This approach is clearly very inefficient. Therefore, an alternative and more efficient method was applied, which exploited the mathematical relationship between diffusion impedance and the diffusion coefficient D .

$$Z_{d\ x\%}^D(\omega) = \frac{Z_{d\ x\%}^{Dref}(\omega / (D/D_{ref}))}{(D/D_{ref})}$$

(Equation 3.8)

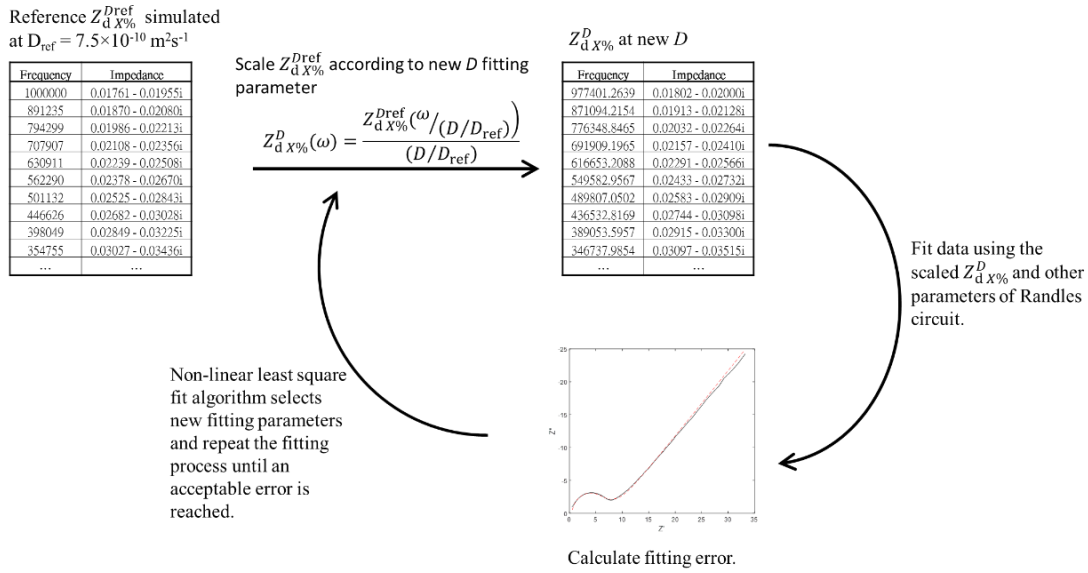


Figure 3.9. Flow diagram depicting the fitting algorithm for diffusion impedance with variable diffusion coefficient D .

Equation 3.8 shows the dependency of diffusion impedance on the diffusion coefficient D for each unique diffusion pattern. For example, the planar (Warburg element), cylindrical, and spherical diffusion patterns are all unique to each other. The diffusion pattern for each different percentage of electrode coverage are also unique. The mathematical relationship in Equation 3.8 can be seen in the analytical equations for Warburg element, as well as the diffusion impedances for cylindrical and spherical diffusions [105]. Furthermore, FEM simulated diffusion impedances of the same percentage of electrode coverage at different D also align with the relationship. This means the diffusion impedance for a particular percentage coverage ($Z_{d X\%}^{D_{ref}}$) can be simulated at an arbitrary reference diffusion coefficient D_{ref} , and the diffusion impedance for the same percentage of coverage at a different D ($Z_{d X\%}^D$) can be calculated using Equation 3.8 instead of having to perform the whole simulation again. Therefore, simulation only needs to be done once at the D_{ref} for each percentage of

beads coverage for data fitting purpose. This model fitting process is summarised in Figure 3.9 and explained in more detail in the following paragraphs.

The output of the FEM calculation was in the form of a table containing a list of defined frequencies (20 entries per decade) and the diffusion impedance corresponding to each frequency. These data were stored as a look-up-table (LUT) and used as the $Z_d^{D_{ref}}$ term in Equation 3.8 to calculate the diffusion impedance of the same coverage at any D for data fitting purpose. Diffusion coefficient of $7.5 \times 10^{-10} \text{ m}^2\text{s}^{-1}$ was the D_{ref} used to simulate and generate the LUT, which was selected to be close to the diffusion coefficient expected from the experiment data. The significance of this was to minimise the scaling of LUT required for fitting, which would reduce the errors introduced by the scaling process.

The $\omega/(D/D_{ref})$ term in Equation 3.8 meant the frequency values scaled as D varied for data fitting. Therefore, the frequency entries in the LUT after scaling was not the same as the frequencies of the fitted impedance data. Therefore, to get the diffusion impedance value at the particular frequencies required for fitting but not available in the LUT, an estimate was obtained by interpolating the data from the two adjacent frequency entries. The proportional relationship between impedance and frequency observed in Warburg element $Z_d(\omega) \propto 1/\sqrt{\omega}$ was used for interpolation.

This relationship between diffusion impedance and diffusion coefficient (Equation 3.8) was implemented with the Randles circuit model (Equation 3.7) using MATLAB's scripting functionality and non-linear least square fit. This allowed fitting of the experiment data to the FEM simulated diffusion impedance, while allowing the diffusion coefficient to vary without having to perform the simulation repeatedly at different diffusion coefficient values.

Copyrighted material:

Figure 7. Sensors and Actuators B: Chemical **237**: 329-340.

<https://doi.org/10.1016/j.snb.2016.06.065>

Figure 3.10. Overlay of the same experimental impedance spectra as Figure 3.8, but with the R_{sol} components removed. The red dashed line represents the Randles circuit model that was fitted to ‘Experiment: Avidin-PS beads’ using the FEM simulated $Z_{d\ 47\%}$ as diffusion impedance.

3.3.2.3. Result of model fitting with FEM simulated diffusion impedance

Figure 3.10 shows the overlay of the same recorded impedances before and after PS beads incubation as in Figure 3.8, but with the R_{sol} component removed. The R_{sol} component is governed by the solution conductivity and is independent to the faradaic process that is the focus of this study. The removal of R_{sol} gives a better visual comparison for the faradaic components in response to surface immobilised PS beads.

Randles circuit model with the simulated $Z_{d\ 47\%}$ as the diffusion impedance component was fitted to the experimental impedance spectra for the electrode with 47%

PS beads coverages (Experiment: Avidin-PS beads). The fitted model is shown as red dashed line in Figure 3.10. The result of the Randles circuit model fitting (Table 3.2: Z_d 47%, Avidin-PS beads) suggested an improvement in data fitting when the FEM simulated diffusion impedance was used (RSS = 3.32) in comparison to the use of a Warburg element (RSS = 9.63). The former encapsulated the effect of obstructed diffusion pattern by surface bound particles, while the latter is a model for unobstructed semi-infinite planar diffusion pattern.

The same analysis was applied to all collected data. Figure 3.11 shows the percentage change in RSS from model fitting of the impedances before PS beads incubation (fitted with Randles circuit with Z_{Warburg}) to after PS beads incubation (fitted with Randles circuit with either Z_{Warburg} or Z_d X%). The fitting result showed that the Randles circuit with Z_{Warburg} as diffusion impedance gave a relatively worse fit with higher surface beads coverage, as evident by the rise in the percentage change in RSS with higher percentage of beads coverage. This result suggested the impedance of electrode with surface immobilised PS beads demonstrated properties that cannot be fully described with Randles circuit using Z_{Warburg} as diffusion impedance. In comparison, the Randles circuit model using FEM simulated diffusion impedance, which encompassed the effects of obstructed diffusion pattern by the PS beads, showed lower rise in RSS in contrast to when Z_{Warburg} was used. This difference is more significant at higher percentages of beads coverage.

Copyrighted material:

Figure 8. Sensors and Actuators B: Chemical **237**: 329-340.

<https://doi.org/10.1016/j.snb.2016.06.065>

Figure 3.11. Percentage increase in RSS of Randles circuit fitting of electrode impedance from before PS beads incubation (using Z_{Warburg} as diffusion impedance) to after PS beads incubation (using either Z_{Warburg} (•) or simulated $Z_{\text{d } X\%}$ (×) as diffusion impedance).

These observations suggest that electrodes with higher densities of surface immobilised PS beads show diffusion patterns that deviate more from the semi-infinite planar pattern described by Z_{Warburg} . The conventional treatment of modelling the impedance change with increase in R_{ct} alone cannot fully describe the observations. On the other hand, FEM simulated diffusion impedance, which models the obstructed diffusion of electroactive molecules, can describe the impedance change caused by surface immobilised PS beads more accurately. However, discrepancy still exists between the experiment data and model, as evident by the increase in RSS value even with the use of FEM simulated diffusion impedance. This variation may have been attributed to factors such as variable particle size, variable elevation of bound particle above the electrode surface, and random clustering of PS beads.

These results show that the distortion of diffusion pattern in the presence of surface immobilised micro-particles is significant in causing an observable change in electrode impedance that cannot be modelled by the conventional approach of using a change in R_{ct} alone. This observed impedance change can be partially explained better with the change in diffusion impedance due to immobilised particles obstructing the diffusion of electroactive molecules.

3.3.3. Application of diffusion impedance in sensing

Investigation into the use of diffusion impedance in sensing applications is described in this section. Firstly, a data analysis approach was developed based on altered diffusion impedance. Subsequently, the validity of the method was evaluated by testing the model against experimental data. Lastly, the diffusion impedance-based approach was compared to the conventional charge transfer resistance-based method to assess its advantages and disadvantages.

3.3.3.1. Change in diffusion impedance with electrode coverage

The diffusion impedance dominates the electrode impedance at low frequencies ($Z_{low \omega}$). The impedance at these low frequencies can be approximated with Equation 3.9 when the diffusion pattern is semi-infinite and planar. The equation shows that the imaginary component $Z_{low \omega}''$ is primarily dictated by the diffusion impedance, while the real component $Z_{low \omega}'$ has contributions from R_{sol} and R_{ct} in addition to the diffusion component. Although the model simulation predicted a greater change in the real component of diffusion impedance in response to surface obstructions than that of the imaginary component, it was difficult to unambiguously isolate the real component of the diffusion impedance Z_d' from the R_{sol} and R_{ct} components in the overall electrode

impedance. Therefore, the imaginary component Z_d'' was used instead for further analyses to avoid this complication. The positive association between the magnitude of $Z_{d,x}''$ and frequency seen in Figure 3.3B was utilised as the indicator for the percentage of surface coverage.

$$Z_{low \ \omega}(\omega) \approx R_{sol} + R_{ct} + Z_{Warburg} = \left(R_{sol} + R_{ct} + \frac{A_W}{\sqrt{\omega}} \right) + \left(-j \frac{A_W}{\sqrt{\omega}} \right)$$

(Equation 3.9)

$$\begin{aligned} -\sqrt{\omega} \cdot Z_{low \ \omega}''(\omega) &= A_W && \text{(semi-infinite planar diffusion)} \\ &= iADN(\omega) && \text{(other diffusion patterns)} \end{aligned}$$

(Equation 3.10)

The product of the terms $Z_{low \ \omega}''$ and $-\sqrt{\omega}$ yields the Warburg coefficient A_W when the diffusion pattern is semi-infinite and planar (Equation 3.10), which is frequency independent. However, when the diffusion is obstructed due to surface bound particles, the model simulation predicts the value calculated in the same way would increase with frequency. This distinction is the basis for detecting the presence of surface bound particles. In the following sections, this value is referred to as the apparent diffusion number (ADN), and $iADN$ to signify those derived from the imaginary component of the impedance.

Normalised $iADNs$ were simulated for different percentages of surface particle coverage and the result is plotted against the excitation frequency in Figure 3.12A. Normalisation was performed by dividing $iADNs$ by the A_W for the bare electrode. Simulation predicted that $iADN$ increases with frequency for particle bound electrodes, and greater increase is associated with higher density of particle coverage. All $iADNs$ approached A_W at low frequencies. This is because of the long diffusion distance that

exists when the excitation signal is low frequency, and the majority of the mass transfer of electroactive molecules occurs far above the surface bound particles which is mostly unobstructed planar diffusion.

Copyrighted material:

Figure 9. Sensors and Actuators B: Chemical **237**: 329-340.

<https://doi.org/10.1016/j.snb.2016.06.065>

Figure 3.12. A) Simulated normalised iADN for different percentages of electrode coverage. B) Experimental normalised iADN before and after PS beads incubation calculated from the impedance spectra in Figure 3.8.

3.3.3.2. Experimental result for the relationship between *iADN* and target coverage

The correlation between *iADN* and electrode surface coverage by particles was examined experimentally. Since *iADNs* were expected to approach A_w at low frequencies regardless of the density of bound particles on the electrode, *iADN* for each measurement was normalised using its mean *iADN* at frequencies lower than 1 Hz. This accounted for random experimental errors caused by variables such as electroactive molecules concentration, temperature, and electrode surface area. The gradient of the plot of normalised *iADN* against frequency was approximated with a line of best fit over the range 20-60 Hz (Figure 3.12B), and the change in this gradient after PS beads incubation was tested for a correlation with the percentage of particle coverage. The use of gradient in characterising *iADN* had the effect of averaging the data across multiple frequency points to reduce the influence of random noise. The frequency range used for the analysis corresponded to characteristic diffusion distances in the range of 1.2-2.1 μm , which were similar to the size of the target PS particles while being low enough that the faradaic process dominated the electrode impedance within this examined frequency range. Estimations using component values from Randles circuit fitting suggests non-faradaic current contributed to less than 5% of the total current at 60 Hz.

The normalised *iADNs* of the impedance spectra in Figure 3.8 are presented in Figure 3.12B. The experimental *iADN* before PS beads incubation was not independent of frequency like as in case of semi-infinite planar diffusion. Possible reasons for this observation is the contribution of non-faradaic current and deviations from the ideal semi-infinite planar diffusion of the faradaic process, which increased the imaginary component of the impedance (and therefore *iADN*) towards higher frequencies. Thus, the difference in the gradient between *iADN* before and after PS beads incubation

($S_{20-60\text{Hz}}^{\text{Avidin}}$ and $S_{20-60\text{Hz}}^{\text{Avidin-PS beads}}$, respectively) is used to test for a correlation with electrode coverage (Equation 3.11). The difference in iADN gradient ($\Delta S_{20-60\text{Hz}}$) for all experiments are plotted against their respective particle coverage in Figure 3.13A. The plot reveals a trend of increase in $\Delta S_{20-60\text{Hz}}$ with higher PS particle coverage, which is in agreement with the FEM model predictions. However, the experimental $\Delta S_{20-60\text{Hz}}$ values are higher than that of the model, possibly due to factors such as impedance drifts or the presence of contaminating objects.

$$\Delta S_{20-60\text{Hz}} = S_{20-60\text{Hz}}^{\text{Avidin-PS beads}} - S_{20-60\text{Hz}}^{\text{Avidin}}$$

(Equation 3.11)

Another possible source for increased iADN gradient is increased proportion of non-faradaic current at high frequencies caused by PS beads incubation. This can occur when either R_{ct} or C_{dl} is increased in response to the presence of PS beads. However, impedances for the electrodes with surface immobilised PS beads do not demonstrates a good fit with a Randles circuit using Warburg element as the diffusion component (Figure 3.8B), suggesting this observed impedance change cannot be fully explained by changing R_{ct} or C_{dl} alone.

Copyrighted material:

Figure 10. Sensors and Actuators B: Chemical **237**: 329-340.

<https://doi.org/10.1016/j.snb.2016.06.065>

Figure 3.13. A) $\Delta S_{20-60\text{Hz}}$ against PS beads coverage. B) ΔR_{ct} (%) against PS beads coverage.

3.3.3.3. Comparison with R_{ct} -based model

$$\% \Delta R_{ct} = \frac{R_{ct}^{Avidin-PS} - R_{ct}^{Avidin}}{R_{ct}^{Avidin}}$$

(Equation 3.12)

The iADN data analysis approach developed in the previous section is compared to the conventional R_{ct} -based method. The changes in R_{ct} value were determined from the same experimental impedance spectra using Randles circuit fitting with the assumption of semi-infinite and planar diffusion of the electroactive molecules regardless of PS beads presence, i.e., using $Z_{Warburg}$ as the diffusion impedance component to fit all impedance spectra. The change in R_{ct} due to PS beads presence was normalised against the R_{ct} value before incubation (Equation 3.12) [34, 37]. The data are presented in Figure 3.13B. The plot shows the correlation between the change in R_{ct} and electrode coverage is weaker than that of iADN gradient. Theoretically R_{ct} is inversely proportional to the available electrode area for charge transfer redox reaction to occur. For instance, reduction of the accessible electrode area by 50% would be expected to cause a 100% increase in R_{ct} . However, the observed R_{ct} increase in response to bound particles is relatively small compared to the random variations. An explanation may be the curvature of the PS beads meant there was little actual contact between the PS particles and the sensor surface to have a significant impact on the accessible electrode area, which has led to a less than expected increase in R_{ct} . The random variations observed in R_{ct} can be caused non-specific drifts due to contamination and drifts in the chemical environment of the electrode surface [74]. Diffusion on the other hand relies on a completely separate physical process to the charge transfer reaction and would exhibit different drift properties. However, the

nature of drift and variability in diffusion impedance need to be assessed in more detail in future studies.

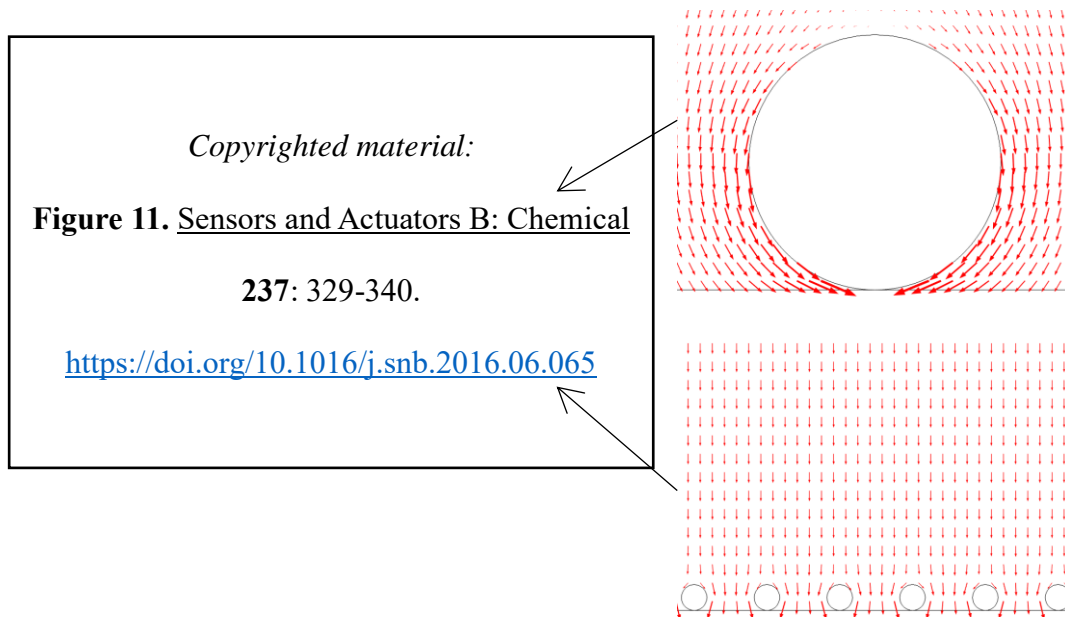


Figure 3.14. Normalised iADN for 0.7 μm and 0.07 μm diameter targets at 50% electrode coverage. The diffusion pattern associated with each analyte size is also present on the right.

The change in the R_{ct} component, used in the conventional data analysis approach, is physically explained by the blocking of accessible electrode surface. The same sensor response should be invoked if the surface coverage is the same, irrespective of the target size. This implies that the sensor reading is susceptible to submicron contamination or chemical inhomogeneity. On the other hand, diffusion is a process that occurs over space; this is in contrast to charge transfer reaction which is an interfacial process occurring on a plane. The distortion in diffusion pattern is minimal when the diffusion distance is relatively large compared to the bound targets. This means the change in

iADN would be lesser in response to smaller analytes, even when the surface coverage is the same. The iADNs for electrode impedances in the presence of particles with diameters of either 0.7 μm or 0.07 μm were simulated at 50% electrode coverage, and the result is presented in Figure 3.14. Simulation showed there is negligible increase in iADN with excitation frequency for the 0.07 μm diameter particles in comparison to its larger counterpart, even though the electrode coverage was equivalent. This theoretical result suggests the capability of diffusion impedance for use in sensing that is selective for analyte size. This also implies that chemical property inhomogeneities or contaminants at submicron scales would have a significant impact on the sensor response. This characteristic is advantageous in the detection of real world samples in which target analytes are often accompanied by a myriad of background molecules of different sizes.

A limitation associated with the implication of target size on diffusion impedance is that the applicable analyte is restricted by the highest frequency at which diffusion impedance can be observed reliably. Diffusion impedance observable at higher frequencies (shorter diffusion distances) is necessary for detecting smaller target analytes, but is prohibited by increased proportion of non-faradaic current with the increase of frequency. This means valid analytes are usually in the micron size or above, such as cells and bacteria, while protein and DNA targets are unlikely to be directly applicable. Other approaches are needed in these cases, such as the use of conventional R_{ct} -based approach or to use of micro-particles to enlarge the size of target entities being observed.

3.4. Conclusion

The contribution of diffusion impedance in biosensing application for micron-sized target analytes was investigated in this chapter. Finite element analysis was used to simulate the effect of micron-sized analyte particles on diffusion impedance for a flat electrode. The model was based on obstructed diffusion of electroactive molecules due to the presence of target particle on the electrode surface, and how this affected the diffusion impedance component. The numerically simulated model was validated against experimentally measured impedance in the presence of bound PS beads, which showed improved agreement in data fitting over the Warburg element that is used conventionally. This model could provide a more precise and profound description of the changes in electrode impedance in response to immobilisation of micron-sized analyte. Further analysis of diffusion impedance led to the proposed use of $iADN$ as the indicator for electrode surface coverage by bound PS particles. The change in $iADN$ showed stronger correlation with the percentage of electrode coverage than the conventional approach using R_{ct} . A possible explanation for this improved correlation may be attributed to the different drift properties of the diffusion process in comparison to the charge transfer reaction. The model developed in this chapter will be applied to evaluate and study the effects of three-dimensional electrode geometry on biosensor performance.

4. Fabrication of Three-dimensional Microelectrodes

4.1. Introduction

Advancements in fabrication technology has made the creation of electrodes at micrometre and nanometre scale possible. On top of that, electrodes with uniquely designed patterns and three-dimensional structures have also been realised with innovative techniques. The sensitivity of electrochemical biosensors generally improves with miniaturisation [58], and the use of different electrode geometries have been shown to influence their properties. Researchers have applied this knowledge to optimise the performance of their sensor devices [111, 117, 118, 124, 125]. In this thesis, electrodes with distinctive three-dimensional geometries were compared for their effects on the performance of faradaic impedance biosensors. This chapter details the fabrication process for creating such electrodes.

The three electrode shapes selected for comparison were flat, ridge-shaped, and trough-shaped digits (Figure 4.1). These structures were selected to represent general cases for flat, protruding, and recessed electrode geometries, respectively. All structures had a cross-sectional electrode surface span of $\sim 10\ \mu\text{m}$, so the different structures had similar dimensions to allow for a fair comparison.

Figure 4.2 shows the summary of the procedures involved in fabricating the three-dimensional electrodes. The overall fabrication process could be divided into four major stages. The first stage was the creation of a master template of the desired structure on a silicon wafer using photoresist. The rounded ridge structure was achieved with the reflowing of photoresist under high temperature after patterning of photoresist channels

using photolithography. Secondly, the template structure was replicated onto nickel stamps using the electroforming technique. Nickel stamps with ridge or trough structures were produced. In the third step, the stamps were used to reproduce the structures on PETG substrates using hot embossing method. Finally in the fourth step, the PETG substrates with the required three-dimensional structures were sputter-coated with gold, and the electrodes were defined with photolithography and wet etching processes. The procedures are described in more detail in the following sections.

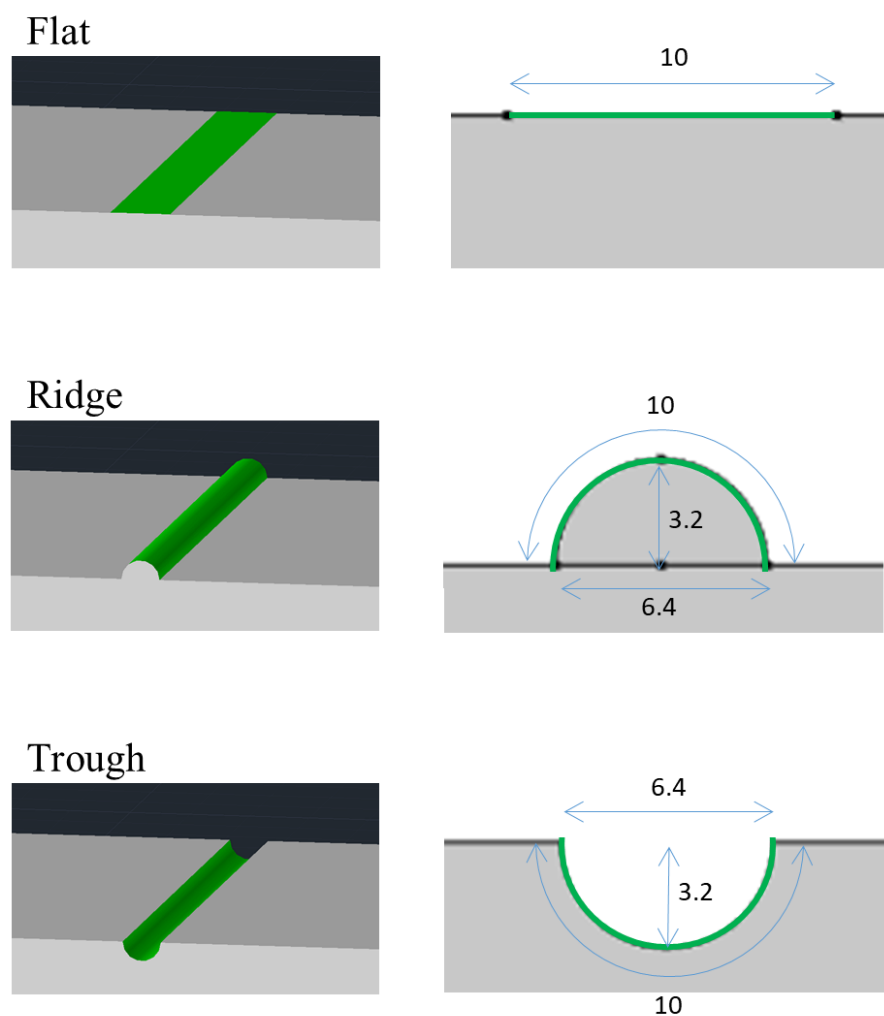
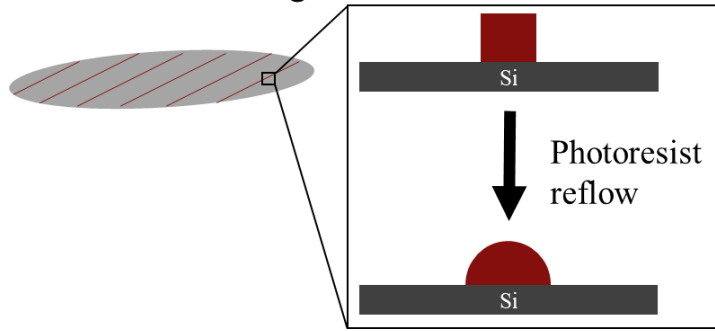
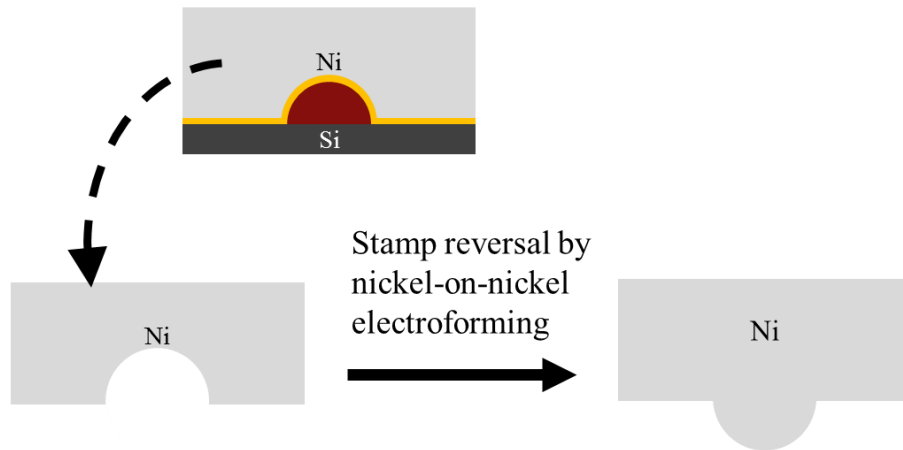


Figure 4.1. The three electrode designs examined in this study. Right: three-dimensional visualisation, left: targeted geometric dimensions. Green colour denotes the electrode surface.

1. Creation of ridge structures on silicon wafer as template



2. Nickel electroforming of gold-coated template



3. Hot emboss to imprint the structures on PETG substrates



4. Gold electrode patterning with wet etch photolithography



Figure 4.2. Summary of the fabrication process for the different electrode shapes.

4.2. Fabrication of the master template using photoresist reflow

4.2.1. Description of the master template

The reflow of photoresist was used to create the curved ridge structures on silicon wafer, which would serve as the master template for downstream processes. The targeted dimensions of the template structure are shown in Figure 4.3. The template consisted of parallel rows of half cylindrical ridges spaced evenly at 5 mm apart on a 3" diameter circular silicon wafer. The targeted half cylinders would have 3.2 μm radius. This gave a cross-sectional length of $\sim 10 \mu\text{m}$ for the curved surface. AZ 1518 photoresist (MicroChemicals) was selected for creating the template ridge structure. This photoresist does not cross-link during its standard photolithography procedure. This is a necessary property that would allow the required rounded structure to form by reflow when the photoresist is subjected to high temperature [140, 141]. Moreover, the standard AZ 1518 photoresist spin coating thickness is close to the height of the required structure. Thicknesses in the 1.5-3.0 μm range is typically achievable with varying spin speeds.

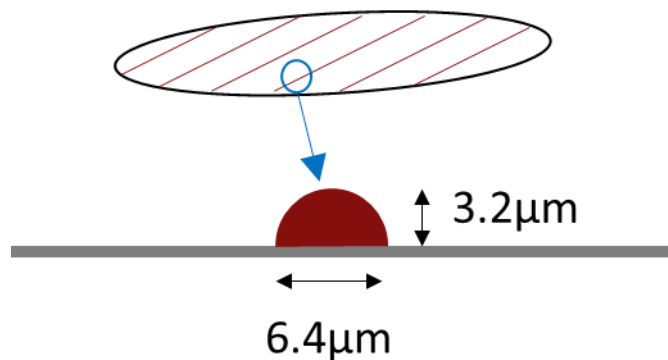


Figure 4.3. The targeted master template structure fabricated using photoresist reflow technique.

4.2.2. Fabrication process for the master template

4.2.2.1. Spin coat and softbake

Firstly, rows of AZ 1518 photoresist were patterned on the silicon wafer using photolithography. Circular silicon wafer (3" diameter) was dehydrated on a heat plate at 110°C for 5 minutes to remove moisture. The removal of surface moisture improved the adhesion of AZ 1518 photoresist to the wafer surface and reduced the occurrence of photoresist structures slipping off from the silicon wafer during the subsequent development step. This problem occurred as the patterned photoresist structures had relatively high aspect ratio with a narrow width (6.4 μm), so there was limited physical interface between the photoresist and the silicon wafer to support an adequate adhesion between the two components. After the dehydration step, the silicon wafer was removed from the heat plate and cooled for 10 minutes before the photoresist was applied.

Next, a thin layer of AZ 1518 photoresist was spread evenly across the whole wafer surface using a pipette. Excess photoresist and air bubbles were removed by pipetting. Special attention was given to ensure no debris or air bubbles were present in the photoresist so that a smooth photoresist layer could be attained after spin coating, which influenced the achievable resolution of the photolithography procedure. The silicon wafer with applied photoresist was spun using a spin coater in a sequence of 500 rpm for 30 seconds followed by 2500 rpm for 60 seconds to achieve the desired photoresist thickness. Afterwards, the silicon wafer with spin-coated photoresist was subjected to softbaking on a heat plate at 95°C for 5 minutes. The softbaking step evaporated the solvent content of the photoresist and allowed the photoresist to be patterned by U.V. exposure. Sufficient solvent must be removed to achieve adequate adhesion between the developed photoresist structures and the silicon wafer. Photoresist structures lifted

off from the silicon wafer during development when a softbake time of less than 4 minutes was used. The nominal photoresist thickness after softbaking was $\sim 2.5 \mu\text{m}$ for a spin coating speed of 2500 rpm, deduced from the spin curve provided by the photoresist manufacturer.

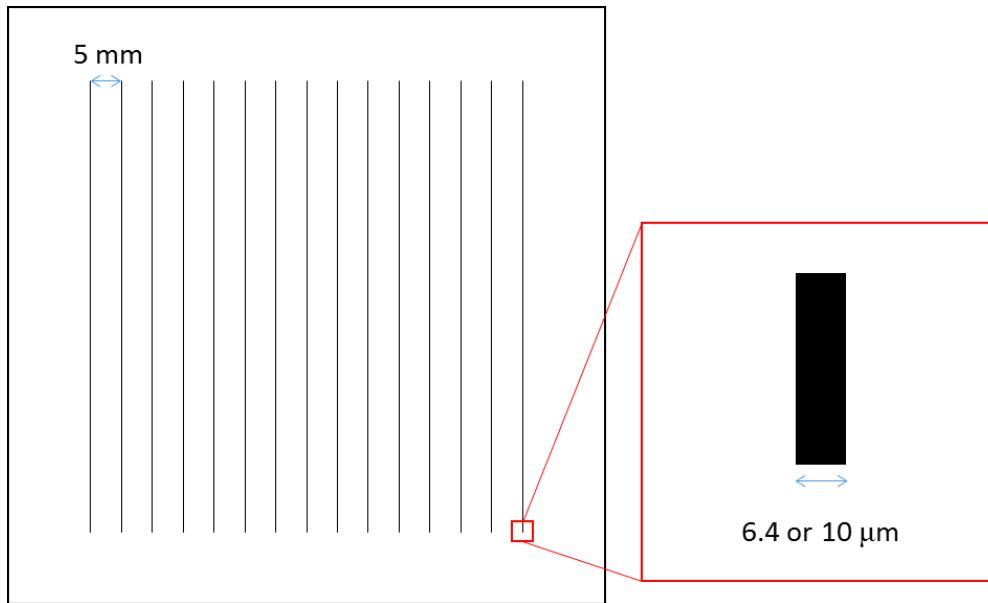


Figure 4.4. Illustration of the photomask pattern and dimensions. There are two masks with line widths of either $6.4 \mu\text{m}$ or $10 \mu\text{m}$.

4.2.2.2. Photolithography

After the softbaking step, the photoresist coated silicon wafer was exposed to U.V. through a brightfield mask illustrated in Figure 4.4 with $6.4 \mu\text{m}$ wide lines. The photomask was purchased from Bandwidth Foundry International. The U.V. exposure was done using the mask aligner Karl Suss MA6. The silicon wafer was placed on the mask aligner stage and hard contact exposure mode was used to secure the silicon wafer against the photomask. In hard contact mode, the movable stage physically pressed the silicon wafer against the photomask on top as depicted in Figure 4.5. The chrome side

of the mask was facing downwards so the patterned chrome mirror was in physical contact with the photoresist, as close as physically allowable.

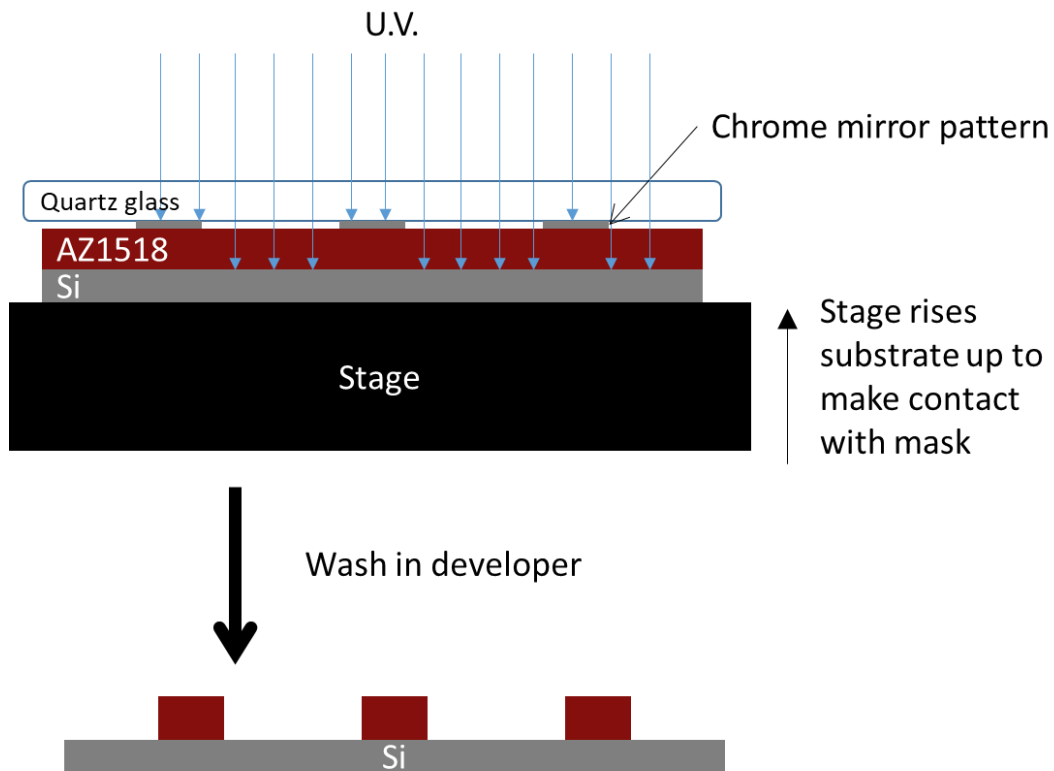


Figure 4.5. Graphical illustration of hard contact mode U.V. exposure and the resultant structure for a positive photoresist

AZ 1518 is a positive photoresist. This meant the photoresist exposed to U.V. was removed in the subsequent development step, while photoresist in areas corresponded to the chrome patterns of the photomask would remain after development (Figure 4.5). The mask aligner had a broad spectrum light source containing g- (wavelength 436 nm), h- (405 nm) and i-line (365nm) emissions. The photoresist AZ 1518 has peak absorption at the i-line emission wavelength. A typical broad spectrum light source consists of ~40% i-line emission. The light source of the mask aligner had a measured intensity of

8.9 mW/cm² for i-line U.V. The photoresist coated substrate was exposed to U.V. for 8 seconds, which gave a total energy of i-line exposure of ~70 mJ/cm².

The exposed substrate was developed by washing in a bath of either AZ 326 MIF or AZ 726 MIF developer solution (MicroChemicals). The wafer was removed from the developer immediately after the photoresist from exposed area of the silicon wafer was completely removed. The wafer was then rinsed with deionised water and dried with an air gun.

It was important that close physical contact was made between the mask and the photoresist surface during U.V. exposure. This was necessary to achieve well defined photoresist structures that closely aligned with the mask patterns. For instance, no debris should be present between the photomask and the silicon wafer, as it could create separation between the two parts during hard contact exposure. Gaps between the chrome mirror and the photoresist would allow the U.V. to diffract and scatter, which adversely affected the achievable structure resolution. The result of U.V. diffraction caused the developed structure to form a trapezoid shape with a base wider than the chrome mask design as depicted in Figure 4.6. Moreover, the edges of the developed photoresist structures became jagged, which is a problem known as a mouse-bite pattern. Furthermore, uneven contact across the silicon wafer with the chrome mask would cause the developed photoresist structure dimensions to vary across the whole silicon wafer.

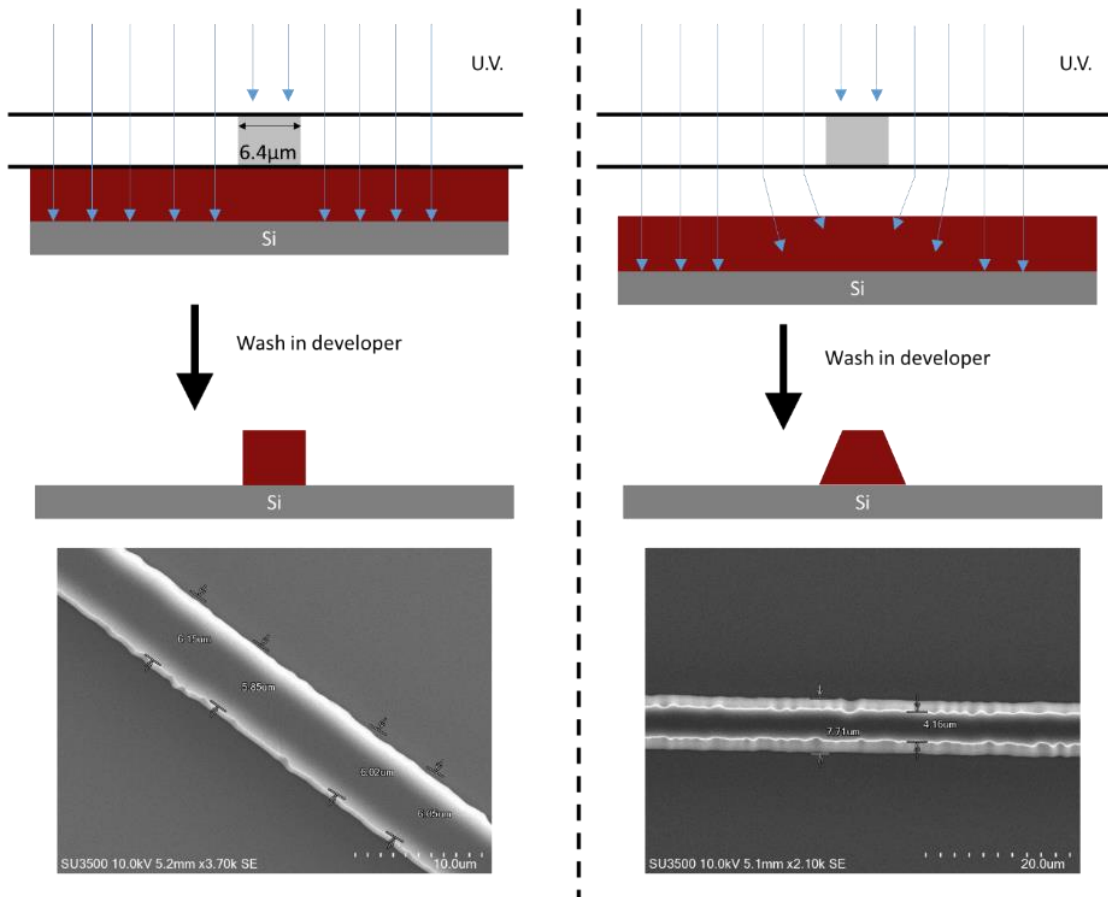


Figure 4.6. The result of good (left) and poor (right) mask-substrate contact during U.V. exposure.

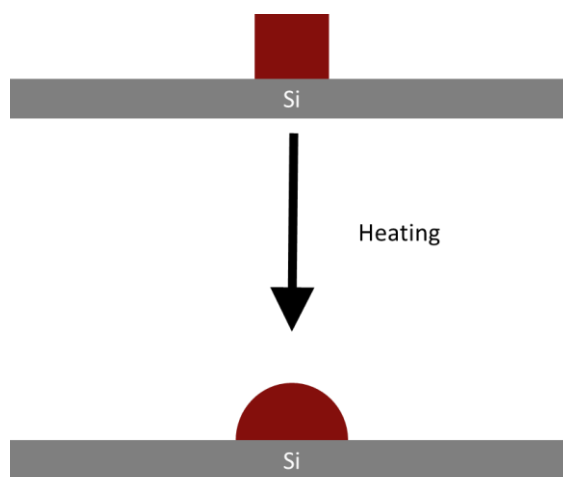


Figure 4.7. Illustration of the effect of photoresist reflow.

4.2.2.3. Reflow of photoresist

After development, the photoresist substrate was immediately placed on a heat plate at 150°C for 3 minutes to cause the photoresist to completely reflow to form ridge structures (Figure 4.7). Delaying the reflow step for too long after development caused a hard shell to form on the outside of the photoresist structure, which did not reflow well. This would lead to the formation of artefacts on the photoresist structure after reflowing as shown in Figure 4.8. The scanning electron microscopy photo of the properly reflowed photoresist is shown in Figure 4.9.

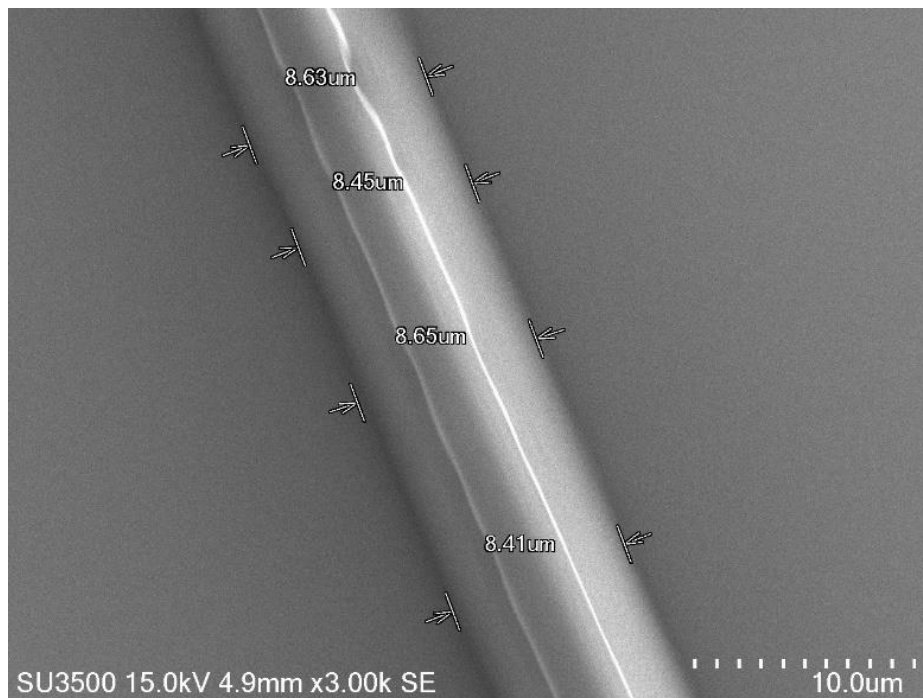


Figure 4.8. Scanning electron microscopy photo illustrating the influence of “shell” formation in the reflow of photoresist.

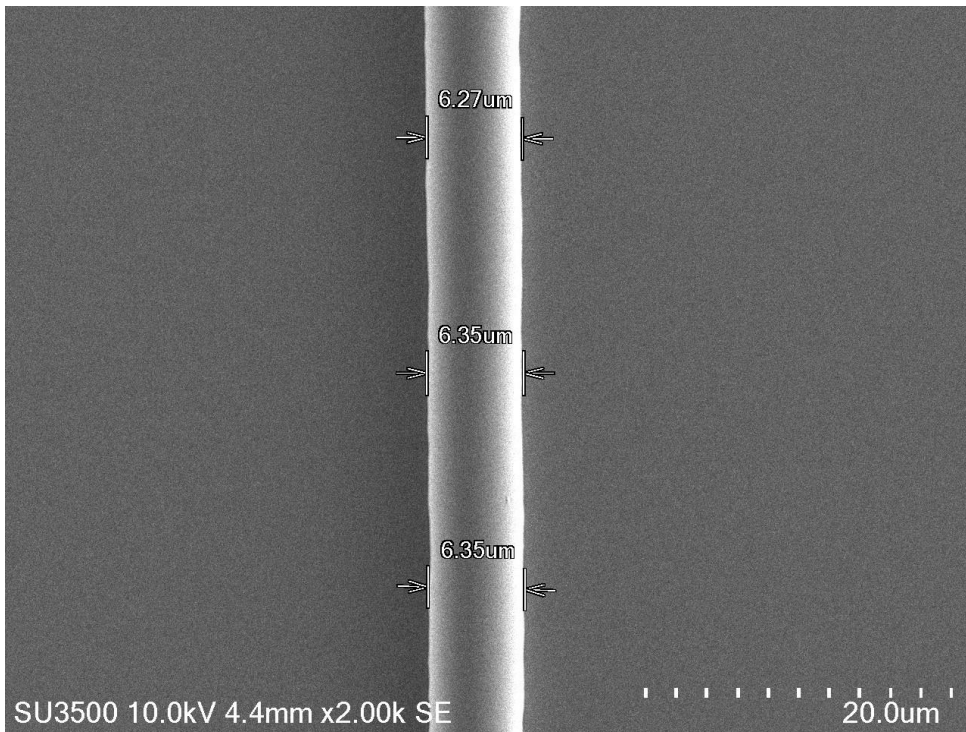
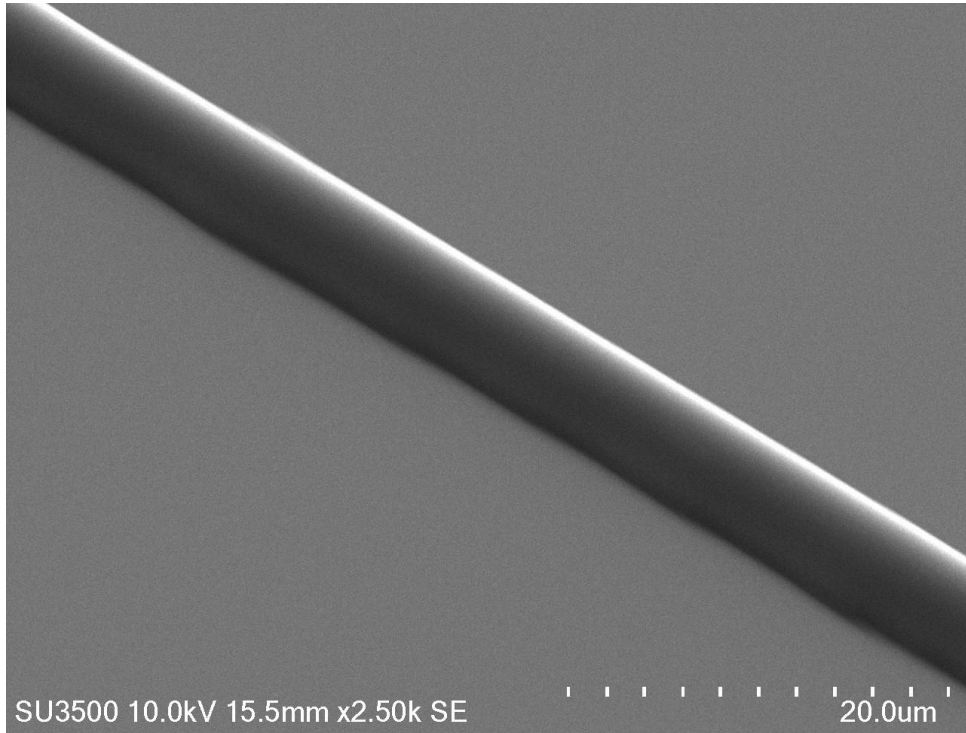


Figure 4.9. Scanning electron microscopy photo of photoresist that was reflowed completely. Top: 45° angle view. Bottom: top-down view.

4.2.2.4. Calibration of process parameters

The thickness of the photoresist was controlled by the speed of spin coating. Understandably, the height of the ridge structures after reflow correlated with the thickness of the coating. However, thick photoresist prevented high resolution features to be achieved with photolithography, as the U.V. must penetrate further into the photoresist to fully expose it. This caused problems such as U.V. diffraction and insufficient U.V. irradiation energy reaching the bottom of the photoresist. The required height of the ridge structures was near the upper limit of the manufacturer's recommended photoresist thickness for AZ 1518. Figure 4.10 shows the height and width of the final ridge-shaped structure after reflow for different spin-coating speeds. The width was measured using a scanning electron microscope, while the height was measured with a stylus profiler (Dektak XT, Bruker). One can see from the graph the produced photoresist structure width deviated more from the desired dimension of 6.4 μm with thicker photoresists at lower spin speeds.

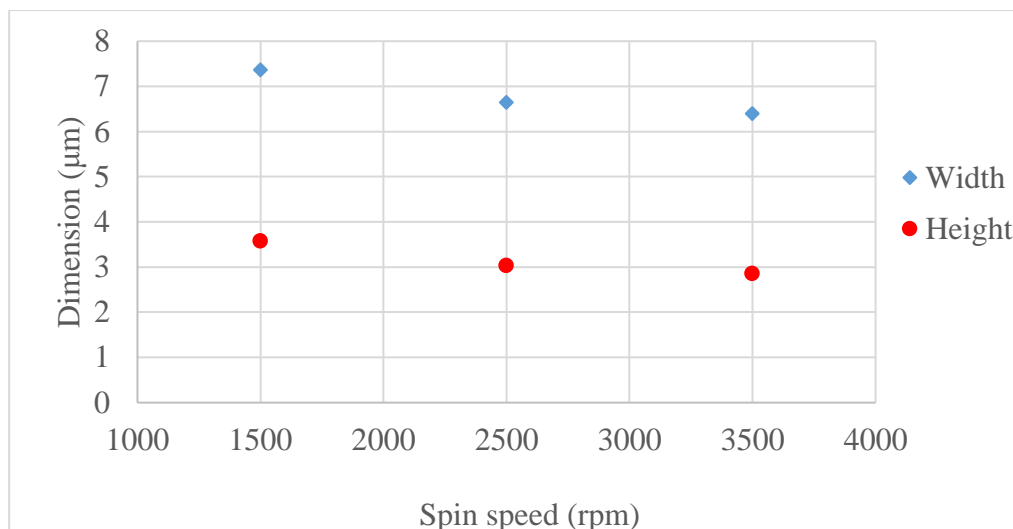


Figure 4.10. Dimensions of ridge photoresist structures produced as a result of different spin speeds during spin coating.

The variation in the amount of U.V. exposure could affect the width of the patterned channels also. Overexposure leads to the removal of more photoresist during development, which creates narrower channels. However, the resolution of the features were found to be not very sensitive to the exposure time. The photoresist thickness and the quality of contact between the chrome mirror and substrate had more significant influence on the resolution of the achieved structure. Exposure time of 8 seconds ($\sim 70 \text{ mJ/cm}^2$) was enough for complete development of the exposed photoresist. Only exposure times of more than 30 seconds ($\sim 270 \text{ mJ/cm}^2$) caused narrowing of the channels by $1 \mu\text{m}$. However, long exposure time also led to the appearance of other problems such as mouse-bite patterns at the edges of the structure. Therefore, the 8 seconds U.V. exposure time was used for photolithography.

Based on the results, 2500 rpm was selected as the width ($6.64 \mu\text{m}$) and height ($3.03 \mu\text{m}$) of the ridge structure resulted in an arc of $\sim 9.9 \mu\text{m}$ in length if the cross-section of the ridge was estimated with a segment of a circle. The working of this calculation is shown below with reference to Figure 4.11.

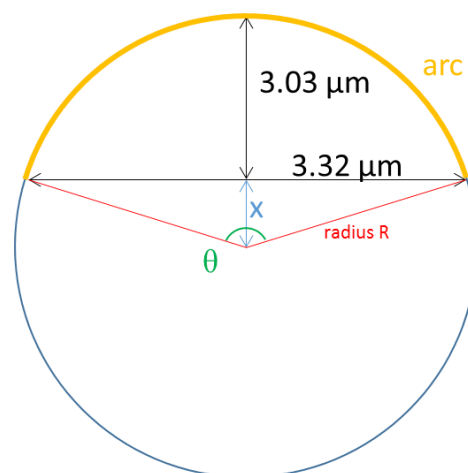


Figure 4.11. Estimating the length of the curved surface of the ridge structure master template.

Calculating the length of the curved ridge surface referring to Figure 4.11.

The following identities could be deduced from the figure.

$$3.32^2 + x^2 = R^2$$

$$R = 3.03 + x$$

Combining the two equations allows the unknown x to be solved to find:

$$x = 0.3039 \text{ and } R = 3.3339$$

Therefore

$$\theta = 2 \cdot \arcsin(x/R) = 2.959 \text{ radians}$$

$$\text{arc} = \theta R = 9.8651 \mu\text{m}$$

4.3. Gold coating the master template

The three-dimensional structures of the fabricated master template was replicated onto nickel stamps using electroforming. The surface to be grown with nickel needed to be conductive. Therefore, the template was vacuum deposited with a gold layer to prepare it for electroforming. As gold has poor adhesion to silicon, the quality of the nickel replica would be adversely affected if the gold layer detached during the electroforming process. Therefore, an intermediate titanium layer between silicon and gold was required as an adhesion layer, while the gold layer itself serves as the highly conductive and stable surface for the electroforming process.

Nano36 magnetron sputtering system (Kurt J. Lesker Company) was used to perform the vacuum deposition process. The titanium target was installed to the radiofrequency power source while the gold target used the direct current power source. The two sputter targets were electrically connected to the cathode of the system. The mechanical shutter for both sputtering targets were closed after installation and the vacuum chamber was cleaned with ethanol. The silicon template was fixed to the stage

overhanging the vacuum chamber facing downwards. The silicon wafer and the stage were electrically connected to the anode of the system. The stage was rotated at 50% speed during the sputtering process to coat the silicon template more consistently.

After the chamber door was sealed, pump down of the vacuum chamber commenced until $<1 \times 10^{-5}$ Torr chamber pressure was reached. Then the pump power was lowered to 50% to allow the chamber to refill with argon gas back to a pressure of 20 mTorr. Argon was the sputtering gas. Positively charged argon plasma was generated when enough voltage was applied across the anode and cathode. The positive argon plasma was attracted to and bombarded the titanium or gold sputtering targets (cathode). This would eject the metal atoms from the target, and some of these atoms would deposit onto the surface of the silicon template.

To sputter coat titanium, radiofrequency power was applied to the titanium target, ramping up at 1 W/s until 100 W was reached. Then the shutter for the titanium target was opened and closed quickly to allow argon plasma to strike and ignite the titanium target. After ignition of the titanium target, the chamber argon gas pressure was lowered to ~ 7.5 mTorr and the radiofrequency power was increased to 140 W at ramp speed 1 W/s. Next, the titanium target shutter was opened for 2 minutes to allow loose titanium atoms to deposit on to the silicon substrate. The shutter was closed and power to the titanium target was turned off at the end of the 2 minutes period to stop the titanium sputtering process.

Deposition of gold layer followed afterwards. The chamber argon pressure was lowered to 3 mTorr. Then direct current power was applied to the gold target for ignition, increasing at 50 W/s until 300 W was reached. Subsequently, the gold target shutter was opened for 3 minutes to deposit the gold layer. Again, the shutter was closed and power to the gold target turned off to stop gold deposition after the 3 minutes period. Finally,

the vacuum chamber was vented and the coated substrate was removed from the stage to complete the coating process.

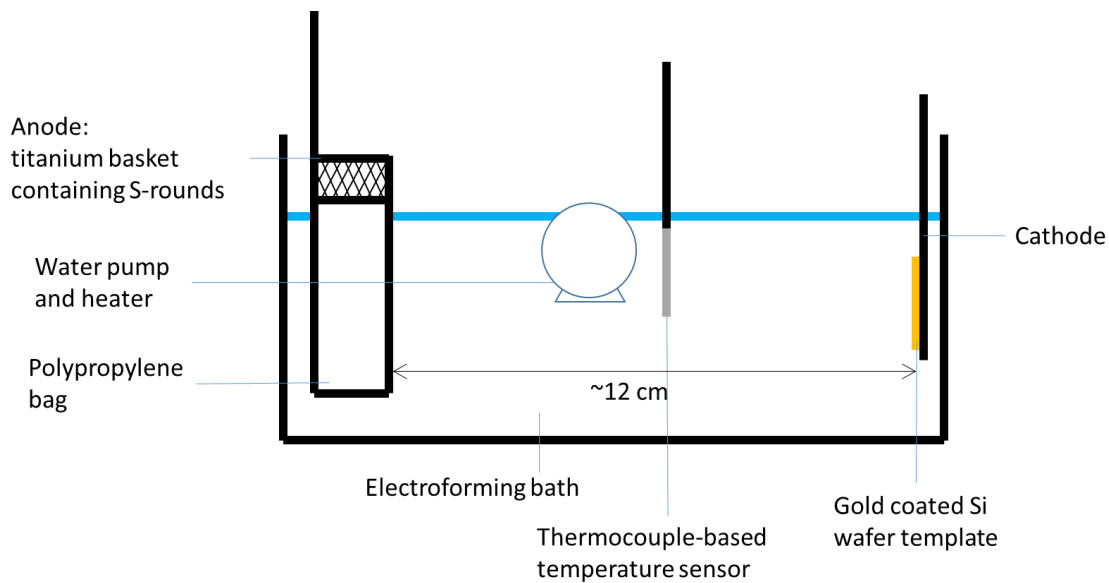


Figure 4.12. Diagram illustrating the electroforming setup.

4.4. Nickel electroforming of the master template

The gold-coated master template with ridge structures was electroformed to produce a nickel stamp with mirrored trough structures. The electroforming process followed the one reported in [142]. The electroforming setup is illustrated in Figure 4.12. A chloride-free nickel sulphamate electroforming bath was used. Typically, chloride ion is included in the bath to increase its conductivity as to increase the nickel deposition rate. However, the formed nickel sheet would usually exhibit internal stress with this approach [143], and this would cause warping and bending of the nickel stamp. Using bent nickel stamp in hot embossing results in a bent embossed substrate. Therefore, a chloride-free bath was selected to minimise deformation of the nickel stamp due to internal stress. This would improve the outcome of the subsequent hot embossing process.

The electroforming bath contained nickel sulphamate (81 g/L Ni²⁺) and boric acid (36 g/L) at a total volume of 10 L. The wetting agent SNAP AM was included in the bath at 4% (v/v) to prevent gas from adhering to silicon wafer during electroforming. The bath pH was adjusted to 4.5 using KOH or sulphamic acid. The bath was kept at a constant temperature of 50°C and actively circulated with a pump to maintain an even distribution of temperature and reagent concentration throughout the bath. The temperature was regulated in a close loop using thermocouple temperature sensor and coiled heater. The bath fluid was filtered with a carbon filter to remove contaminations.

The gold-coated silicon was electrically connected and secured to the cathode of the electroforming power source with copper tape. Subsequently, the whole cathode was covered in insulating tape except for the areas where nickel would grow, i.e. only the gold coated silicon wafer with ridge-shaped three-dimensional structures would be exposed to the electroforming bath. The anode was connected to a titanium basket containing sulphur depolarised nickel S-rounds. The whole basket was wrapped inside a polypropylene bag to prevent nickel debris from entering the bath fluid. The cathode was placed with the silicon wafer facing towards the anode with a separation distance of ~12 cm while completely submerged in the electroforming bath.

The electroforming process was done by supplying a constant voltage between the cathode and anode. The deposition of nickel started with a micro throwing power of 1.5 A/dm² of plating area. Micro throwing preferentially deposited nickel into cracks and cavities of the template's surface, which helped to replicate the small three-dimensional structures at high resolution. The micro throwing power was maintained for 20 minutes before it was increased to 2.5 A/dm² to accelerate nickel deposition. Electroforming continued for another 5 hours at this power before switching off. Afterwards, the produced nickel stamp was peeled off from the silicon wafer and rinsed with water. This

nickel stamp contained trough features, and it imprints ridge structures onto the substrate when used for embossing. The nickel stamp thickness was measured using a calliper to be $\sim 150 \mu\text{m}$. The produced nickel stamp remained relatively flat, indicating a low internal stress. This nickel stamp with trough features was subjected to the same electroforming process in place of the silicon wafer to obtain a nickel stamp with ridge structures, which was used to emboss trough patterns on the embossed substrates.

4.5. Hot embossing

The produced nickel stamps were used to hot emboss PETG sheets to replicate the three-dimensional ridge and trough shapes on the substrate. PETG sheets were cut into roughly $8 \text{ cm} \times 8 \text{ cm}$ squares before hot embossing. NanoImprinter YPL-NIL-SI400 (Wu Xi Imprint Nano Tech. Ltd.) was used to perform hot embossing. The embossing temperature was set to 110°C . The preheat time and press time were both 15 minutes. The embossing plate pressure was approximately 100 N per cm^2 of the PETG substrate area.

PETG substrate and nickel stamp were placed in the embosser's chamber. The nickel stamp was placed on the bottom facing upwards with the PETG substrate placed directly on top. A kapton film was placed at the back of the PETG to keep its back side smooth after the embossing process. All the pieces were sandwiched between two steel plates and placed on the embosser's stage. The chamber door was closed before starting the embossing process. Firstly, the chamber air pressure was pumped down to create vacuum within the chamber. Then preheat delay happened for 15 minutes, which allowed the embosser's press to reach a relatively steady temperature of $\sim 110^\circ\text{C}$. Next, the actual hot embossing happened for the next 15 minutes with the embosser applying pressure between the nickel stamp and the PETG substrate. Finally the chamber was

vented and the vacuum was released. The nickel stamp was carefully peeled off from the PETG substrate to complete the embossing process. Figure 4.13 shows a cross-section of embossed PETG with ridge structure. It can be seen that the ridge closely resembles the segment of a circle.

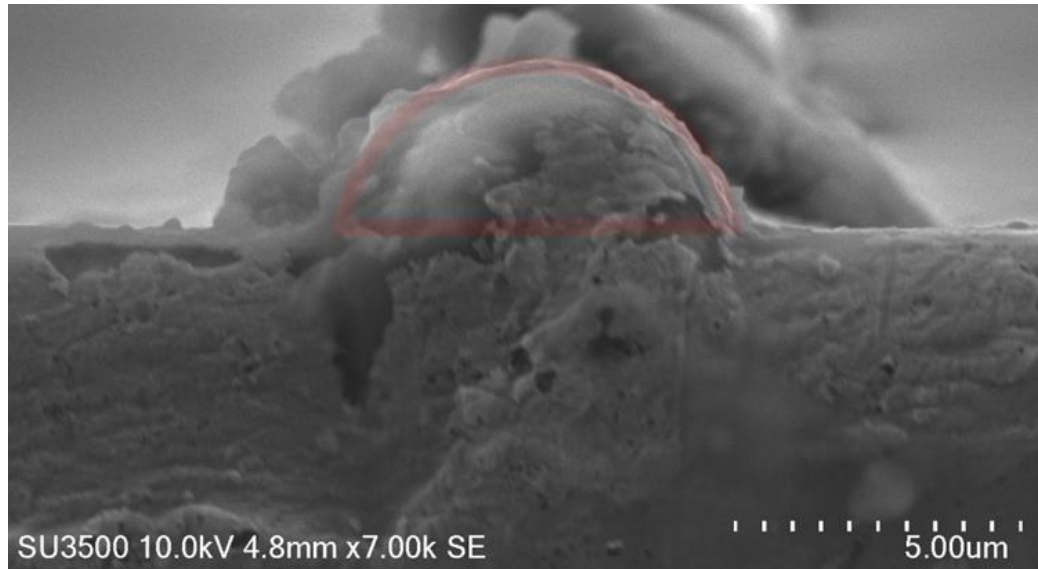


Figure 4.13. A cross-section of the ridge structure of the embossed PETG. The ridge shape closely resembles the segment of a circle (semi-transparent red outline)

4.6. Defining electrodes with photolithography

4.6.1. Gold coating

Gold electrodes were created on the pristine flat PETG and the embossed PETG with three-dimensional structures. Firstly the flat and embossed PETG were gold coated using vacuum deposition as described before in Section 0 except the deposition of titanium layer was omitted. Whole pieces of PETG substrates were coated with gold in this process. Subsequently, photolithography and wet etching were used to define the electrode area.

4.6.2. Spin coat and softbake

AZ 1518 photoresist was used again but this time for wet etch photolithography. The nickel stamp had a smaller area than the embossed PETG sheet. Therefore, hot embossing left raised edges around the outside of the stamp area. The gold-coated PETG substrates were trimmed with a guillotine to remove these raised edges. This was to encourage removal of excess photoresists during the spin coating process, since the higher edge would cause retention of excess photoresist. Because PETG has a very low glass transition temperature ($\sim 80^{\circ}\text{C}$), all the necessary heat treatments in the photolithography process needed to be below this temperature to avoid flowing of the PETG and subsequent tearing of the gold layer.

The PETG substrates were first rinsed with isopropanol followed by water, then the substrates were dried with compressed air and heated on a heat plate at 65°C for 20 minutes to remove moisture. Next, the photoresist AZ 1518 was applied across the whole substrate and made sure no debris or bubbles were present in the photoresist. The substrate was then spun at 200 rpm for 15 seconds followed by 1000 rpm for 60 seconds to remove excess photoresist. After that, the samples were softbaked on a 65°C heat plate for 3 minutes to make the photoresist slightly viscous before cutting them into smaller pieces of about $1.5\text{ cm} \times 2\text{ cm}$, which would be the approximate size of the final sensor unit. This was because cutting the substrates after completion of softbaking causes the photoresist layer to crack. Softbaking of the photoresist coated substrates continued afterwards at 65°C for a further 30 minutes.

The reason for cutting down the sensor into smaller pieces was to improve the contact between substrate and photomask during the next U.V. exposure step. Since the resolution of required features was relatively small (microns scale) a good contact

between the substrate and photomask was necessary to avoid problems such as light diffraction, which would compromise the achievable feature resolution. Better contact could be achieved in two-folds by cutting down the substrates. For one is the removal of photoresist edge beads. The edge beads created raised edges around the spin-coated substrate and prevented a close contact to be achieved between the photomask and substrate during contact photolithography. The other advantage is to minimise the effects of substrate curvature. Even though the bending of nickel stamp was minimised by reducing internal stress using a chloride-free electroforming bath, the stamped PETG substrates still exhibited some bending after hot embossing. Cutting down the PETG substrates into smaller pieces reduced the overall curvature of each sample and allowed more consistent contact to be achieved during contact photolithography. The samples were subjected to photolithography to define the electrode area after softbaking.

4.6.3. Photolithography

4.6.3.1. Photolithography of flat electrode

The brightfield mask with 10 μm wide lines was used to define the 10 μm wide digits that would serve as the flat electrodes. Additionally, the section that would be used to make electrical contact with the potentiostat was created on the mask using non-U.V. transparent kapton tape as shown in Figure 4.14. The tape was stuck to the side of the photomask opposite to the chrome mirror. This was done to avoid the tape causing increased separation between the mask and the substrate during photolithography. As the connector area masked by the tape was a very large area and did not require a high resolution, it was viable to have a large separation between the tape and the photoresist surface (thickness of the quartz glass).

Contact photolithography was performed with the AZ 1518 coated pristine flat PETG samples using the Karl Suss MA6 mask aligner in hard contact mode. The substrates were exposed to the U.V. source for 10 seconds (89 mJ/cm^2 exposed i-line energy).

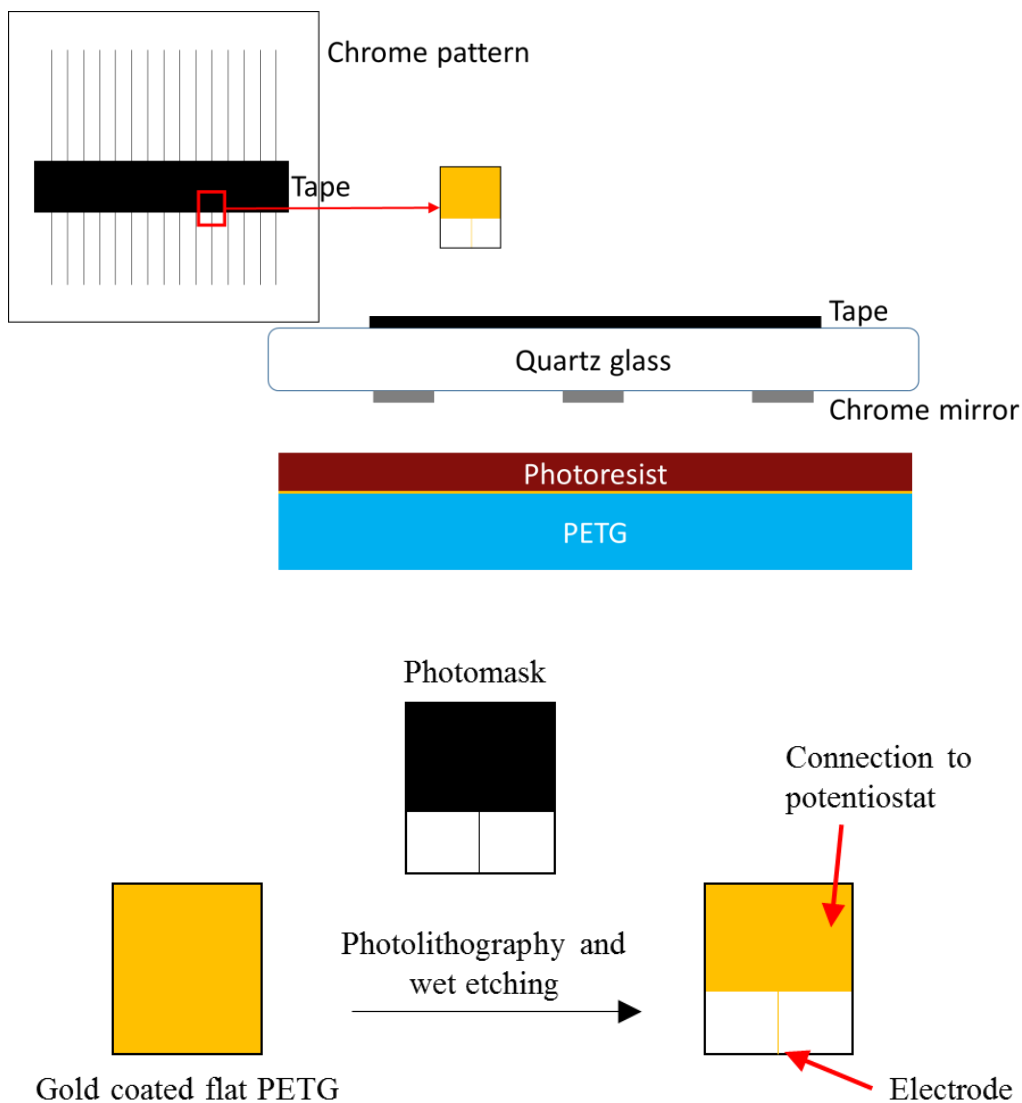


Figure 4.14. Top: brightfield mask and the substrate configuration during hard contact U.V. exposure. Bottom: illustration of the photomask and the resultant flat electrode.

4.6.3.2. Photolithography of trough-shaped electrode

Producing the trough-shaped electrodes did not require a photomask. The method relied on the thicker photoresist over the trough regions. By controlling the U.V. exposure time (and thus the total exposed energy), the photoresist outside of the trough could be selectively removed as shown in Figure 4.15. Only the potentiostat contact area was masked using kapton tape on a piece of clear quartz glass. The UV exposure was calibrated to 9 seconds for optimal result (80.1 mJ/cm^2 exposed i-line energy).

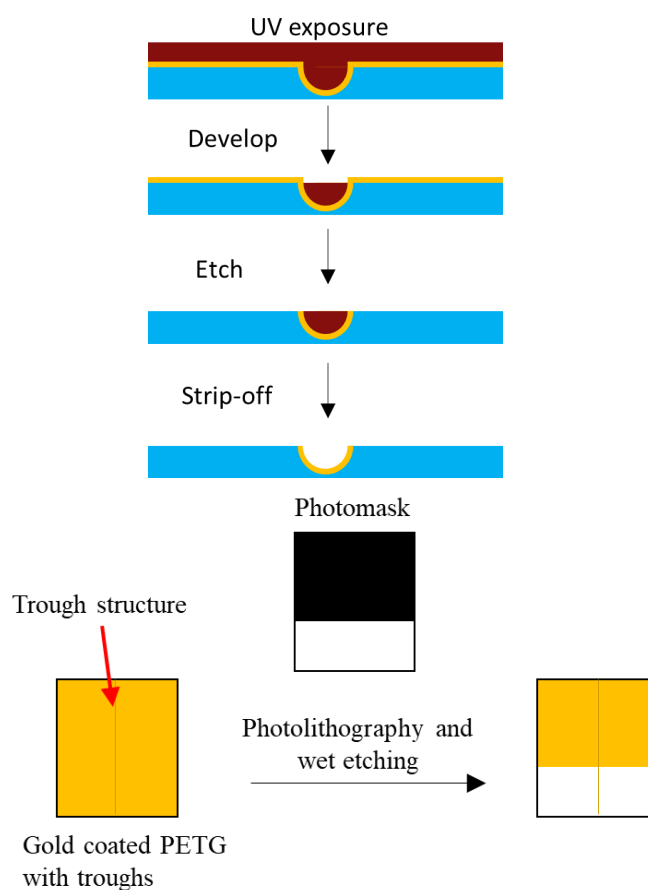


Figure 4.15. Top: illustration of how trough-shaped electrodes were produced without using a photomask pattern. Controlling the U.V. exposure energy allowed selective removal of the photoresist on top while retaining the photoresist inside the troughs. Bottom: illustration of the photomask and the resultant trough-shaped electrode.

4.6.4. Gold etching and photoresist strip-off

The U.V. exposed substrates were developed in AZ 326 MIF or AZ 726 MIF developer bath with continuous agitation. The substrates were immediately removed from the bath and rinsed with water when the U.V. exposed regions were clear of photoresist. At this stage, areas to retain the gold layer were protected with photoresist, while regions of gold to be removed were exposed. Subsequently, the exposed gold were etched in gold etchant (651818, Sigma-Aldrich) with agitation. The gold etchant was diluted 1:2 etchant to water ratio before use. Diluting the gold etchant slowed down the etching speed and allowed better control for the extent of etching to avoid over etching of the gold electrodes. The substrates were removed from the etchant immediately and rinsed with water after the gold on the exposed surfaces were completely removed.

The remnant unexposed photoresist covering the gold electrodes were stripped-off after etching of gold. Since PETG was not very chemically resistant and was susceptible to attack by many solvents, most of the normal strip-off agents such as acetone were not compatible for the substrate. However, 3% NaOH in water (w/w) was found to be capable of removing AZ 1518 photoresist effectively, and it did no visible damage to PETG after being in contact for 1 hour. Therefore, the photoresist was stripped-off in 3% NaOH solution by strong agitation for 5 minutes and rinsed with water afterwards. Figure 4.16 shows a scanning electron microscopy photo of a produced trough-shaped electrode.

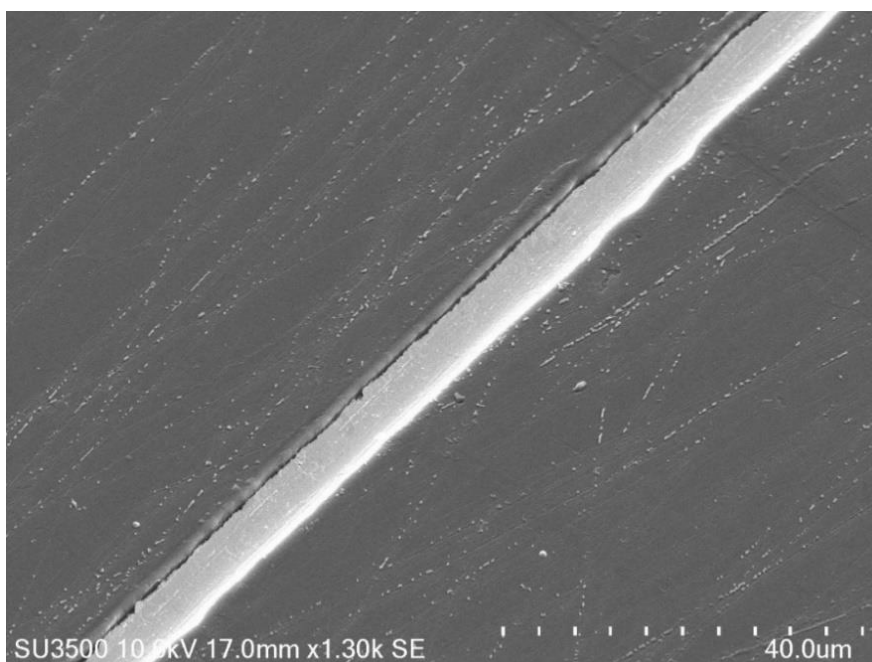


Figure 4.16. Scanning electron microscopy photo of a trough-shaped electrode. The lighter area delineates the gold coating.

The width of the electrodes were measured using scanning electron microscopy, while the depth of trough-shaped electrodes were measured with a stylus profiler (Dektak XT, Bruker). The widths of the flat electrodes were $10.4 \pm 1.1 \mu\text{m}$, and the trough-shaped electrodes had widths of $6.8 \pm 0.1 \mu\text{m}$ and maximum depths of $3.0 \pm 0.1 \mu\text{m}$. The trough geometry had a slightly lower aspect ratio than the targeted semi-circular shape, but these dimensions gave a mean cross-sectional electrode span of $9.91 \mu\text{m}$ which was close to the targeted $10 \mu\text{m}$. The trough-shaped electrodes showed less variation in the dimensions, probably due to the different approaches of wet etch photolithography for producing the two electrodes.

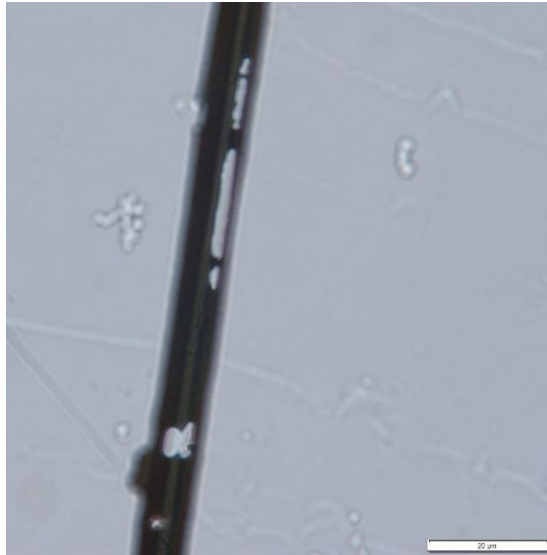


Figure 4.17. Optical microscopy photo of an ridge-shaped electrode digit with deteriorated gold layer. The darker areas delineates the gold coating.

4.6.5. Challenges with ridge-shaped electrodes

Attempts were made to create the ridge-shaped electrodes. Chrome mask with 6.4 μm wide lines was used to mask the gold coated ridge structures during U.V. exposure. The photomask pattern was aligned with the ridge structure using the mask aligner. However, ridge-shaped electrodes were found to be prone to deterioration after etching as shown in Figure 4.17. This may be caused by the thinner photoresist layer on the top and on the sides of the ridge structure after development (Figure 4.18), which was unable to provide adequate protection of the gold layer underneath from chemical etching.



Figure 4.18. Graphical illustration of the photoresist on the ridge structure after development.

To overcome this problem, the use of a very thick layer of photoresist was attempted with spin coating speeds lower than 1000 rpm. However, the same problem of deteriorated electrodes persisted. In addition, the resolution of the developed photoresist structures was severely affected as the spin speed and photoresist thickness were outside of the manufacturer's recommended range. This created overhangs of gold on both sides of the ridge structure as shown in Figure 4.19. This meant the electrode was no longer a completely convexed surface, and it could not faithfully reflect the properties of such electrode.

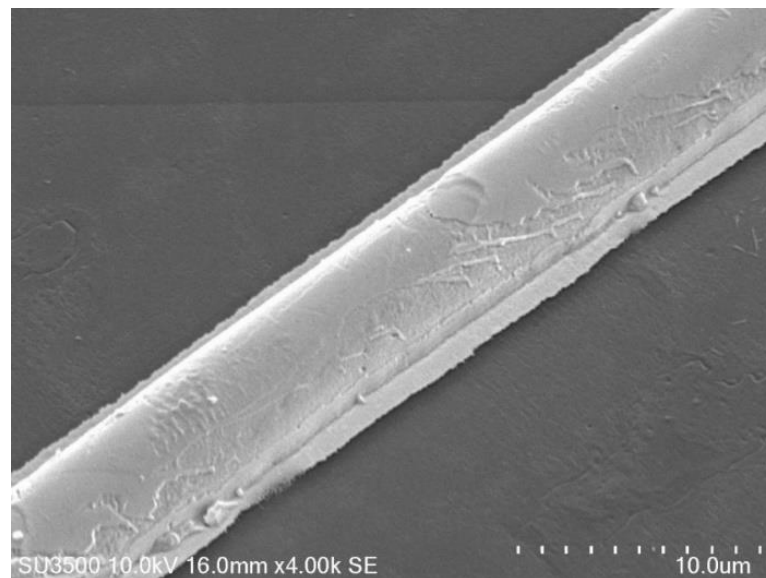


Figure 4.19. Scanning electron microscopy photo of a ridge-shaped electrode showing overhangs of gold on either sides of the ridge.

4.7. Device setup

For the ease of experiment and later data analysis, an experiment setup which expose a known length of the electrode digit to reagents was desirable. The photoresist SU-8 (MicroChemicals) was used to cover the electrode digit and exposed only a small section for experimentation. SU-8 2035 was made by diluting every gram of stock SU-

8 2075 with 0.05g cyclopentanone. A thin layer of SU-8 2035 was spread as evenly as possible on the PETG gold electrode chips and spin-coated with a sequence of 500 rpm for 30 seconds followed by 4000 rpm for 1 minutes. Then the coated substrates were placed on the heat plate at 65°C for 3 minutes to make the SU-8 photoresist more viscous. This was to allow trimming of the substrate edges to remove SU-8 edge beads with a guillotine. Cutting after complete softbake of the SU-8 would cause the photoresist to crack. After the removal of excess photoresist the samples were softbaked for a further 45 minutes.

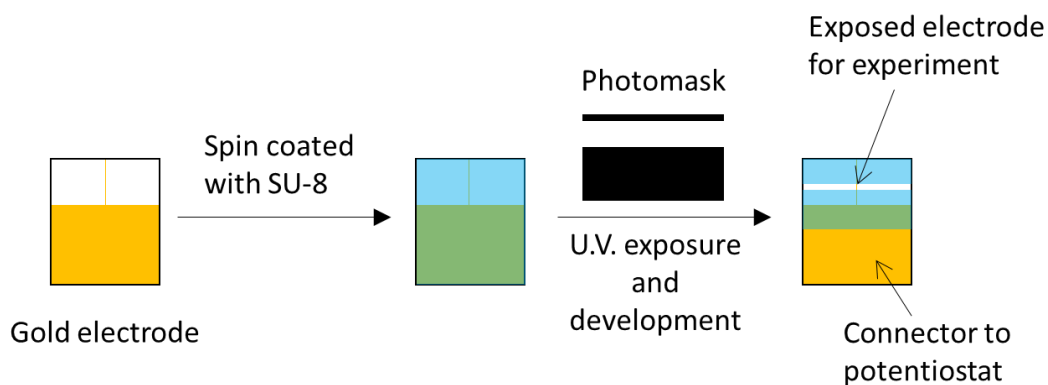


Figure 4.20. Illustration of the photolithography steps for creating SU-8 channels.

The softbaked substrates were exposed to U.V. using a photomask to define the exposed section of electrode digit. SU-8 is a negative photoresist, which means areas exposed to U.V. would remain on the substrate after development. The photomask was made by printing a $\sim 350 \mu\text{m}$ wide line on a transparency film with a laser printer, and the pattern was copied onto a chrome mask by photolithography with AZ 1518 photoresist and chrome etching. The photomask and the final SU-8 photoresist pattern are illustrated in Figure 4.20. The photoresist was exposed to U.V. through the photomask in hard contact mode. Exposure was done for 45 seconds at 8.9 mW/cm^2

(400 mJ/cm²). After the U.V. exposure step, post exposure bake was done by heating the substrate on a heat plate at 65°C for 45 minutes.

Finally the baked samples were developed to remove the unexposed photoresist. The standard SU-8 photoresist developer is PGMEA (propylene glycol monomethyl ether acetate). However, it was not suitable here due to the weak chemical resistance of PETG to this solvent. A brief exposure of PETG to PGMEA caused dissolution of the plastic. Although the gold electrode was able to protect the PETG underneath it from attack, the solvent could still attack the PETG substrate from the exposed area. This could potentially damage the electrode from the edges (Figure 4.21). A SU-8 developer alternative to PGMEA was sought after. It was found that diacetone alcohol does not corrode PETG after soaking the plastic in the solvent for 30 minutes, and the solvent functions as an alternative SU-8 developer without major difficulty except for a slightly longer development time. Therefore, diacetone alcohol was the ideal SU-8 developer when working with PETG substrates. The sensor substrates were developed in diacetone alcohol for 5 minutes after post exposure bake to ensure the unexposed photoresist was completely removed from inside the channel. The width of the SU8 channels were measured using scanning electron microscopy to be $360.0 \pm 10.2 \mu\text{m}$.

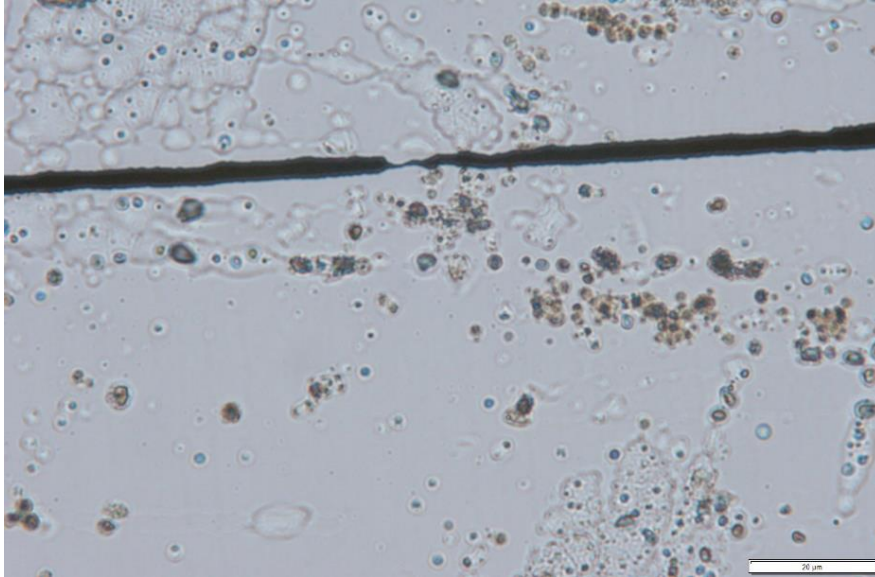


Figure 4.21. Optical microscopy photo of the effects of PGMEA on PETG substrate. The dark band on the photo was a flat electrode digit.

The fabricated sensor was fixed in a setup illustrated in Figure 4.22. A chamber for holding fluid over the exposed electrode digit was created by clamping down a piece of PDMS (polydimethylsiloxane) with a hole punched in the middle, sandwiched between two pieces of PMMAs (poly(methyl methacrylate)). This setup was used to perform experiments with the different electrode designs.

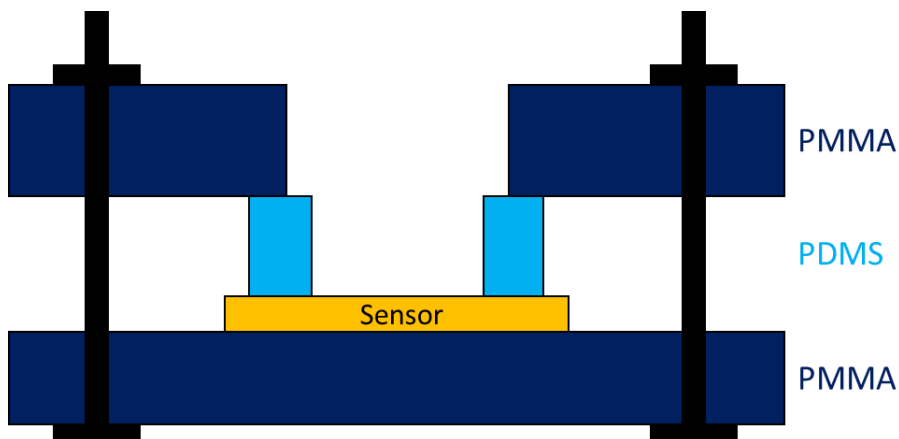


Figure 4.22. Graphical illustration of the device setup for conducting experiments.

4.8. Conclusion

This chapter provided a detailed account of the developed fabrication process for flat and trough-shaped digit electrodes. The fabrication of ridge-shaped electrode was attempted, although difficulties relating to deterioration of the electrode were encountered. Photoresist reflow was used to create the required three-dimensional shapes on silicon wafer which would serve as the master template. The structures of the template was replicated onto nickel stamps using electroforming technique. The nickel stamp was used to imprint trough structures on PETG substrates with hot embossing. Finally, the substrates were sputter coated with gold and electrodes were defined using wet etch photolithography. Both of the flat and trough-shaped electrodes had a cross-sectional length of $\sim 10\ \mu\text{m}$, allowing them to be dimensionally comparable in the subsequent experimentation for their performance in biosensing application.

5. Effects of Three-dimensional Electrode Geometry on Sensor Performance

5.1. Introduction

This chapter details the investigation of the effects of three-dimensional electrode geometry on the sensitivity of faradaic mode electrochemical impedance biosensors. The description and fabrication of the three selected electrode shapes for comparison (flat, ridge, and trough) are detailed in Chapter 4. The effect of electrode geometry on sensor performance was first examined theoretically with numerical simulation. The simulation used the model developed in Chapter 3, in which the mechanism of signal transduction was based on the increase in faradaic impedance due to obstructed diffusion of electroactive molecules by immobilised analytes on the electrode surface. Micron-sized polystyrene (PS) bead was used as the model analyte as in Chapter 3. Subsequently, the fabricated electrodes were subjected to sensing experiments to validate the theoretical results.

5.2. Finite element model

5.2.1. FEM model setup

FEM simulation was used to solve Fick's second law to provide a theoretical understanding of the underlying diffusion process associated with the different electrode geometries. The same modelling approach and parameters developed in Chapter 3 was applied here. The numerical model simulated one finger of each of the three electrode shapes enclosed by vertical walls with zero diffusion flux (Figure 5.1A).

The ceiling boundary was implemented with fixed ferrocyanide/ferricyanide redox couple concentration of 5mM/5mM to emulate the bulk solution. The dimensions for each of the different electrodes used in the simulation were the same as those described in Figure 4.1. Again, the model assumed the condition of semi-infinite diffusion. The lowest excitation frequency simulated was 1 Hz, which had a corresponding characteristic diffusion distance of $\sim 11 \mu\text{m}$ [106]. Therefore, the limits of the model space were at least 500 μm away from the electrode to minimise any effect of blocking or absorbing boundaries.

The characteristic diffusion distance for the electrode digits are approximations only as the definition (Equation 2.26) is for planar diffusions pattern. The electrode digits of this chapter exhibit mostly a cylindrical diffusion pattern. The diffusion distance for cylindrical diffusion are shorter in comparison to planar diffusion due to the radial pattern. However, the diffusion pattern for electrode digits approaches the planar pattern at high excitation frequency, where the diffusion distance is relatively short in comparison to the dimensions of the electrode digits.

PS beads were distributed evenly on the surface of the electrode as illustrated in Figure 5.1B to simulate the effect of their presence on diffusion impedance. The number of beads in each row along the y-axis was varied to simulate the diffusion impedance in response to different densities of bound analyte. The same applied to ridge and trough-shaped electrodes with the beads distributed evenly on the curved surface.

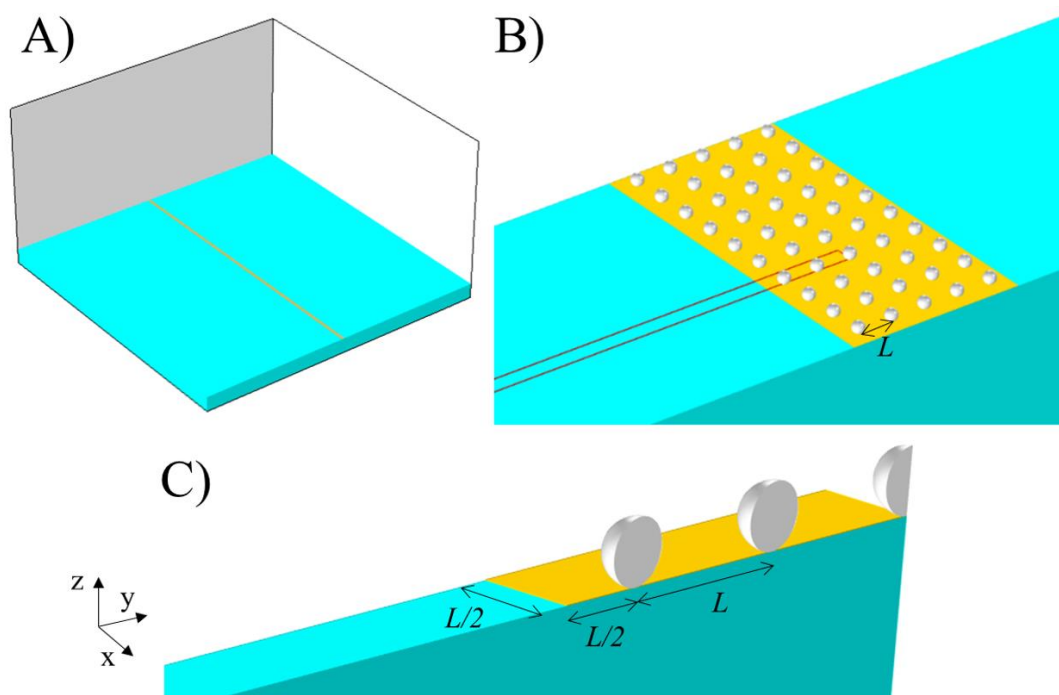


Figure 5.1. Graphical representation of the geometry simulated with finite element method. Gold colour denotes the electrode surface, cyan represents the underlying PETG sensor substrate, and white sphere represents the PS beads model analyte. A) a digit of a flat electrode. B) the even spread of PS beads on the electrode surface. C) the actual geometry simulated after space reduction. The PS beads are spaced evenly by distance L .

The model space could be simplified significantly by exploiting the symmetry in the geometry of the simulated model. The area delineated by the red lines in Figure 5.1B was the only unique section in the model space. This section could be used to recreate the whole model by copy translation and reflection. Therefore, simulation of the diffusion pattern could be performed in the specified unit cell (Figure 5.1C) and the result directly scaled to electrodes of longer lengths. The newly created periodic boundaries in the xz and yz planes due to space reduction could be implemented as

blocking boundaries without changing the diffusion pattern since there were no diffusion in the y or x directions, respectively, at those planes.

Flat and trough-shaped electrodes exhibited sharp edges at their borders. The local diffusion flux at these edges was infinite, creating singularity points (infinite flux on an infinitely small point). FEM simulation approximated the flux at these positions with a very large but finite value. The simulated molecule flux at singularities does not converge with smaller element size during mesh refinement but increases indefinitely. This was a source of error in the finite element model. However, singularities only generated localised errors, and the molecule flux integrated over the whole electrode surface was used to calculate the diffusion impedance. The integrated value of a singularity becomes a finite value (integration of infinite value over a volume approaching zero), and so it does not contribute greatly to the total molecule flux in each model. Therefore, the simulated diffusion impedance of the overall model was able to converge through mesh refinement studies, despite the singularity points, to give a reliable model solution and does not affect subsequent analysis.

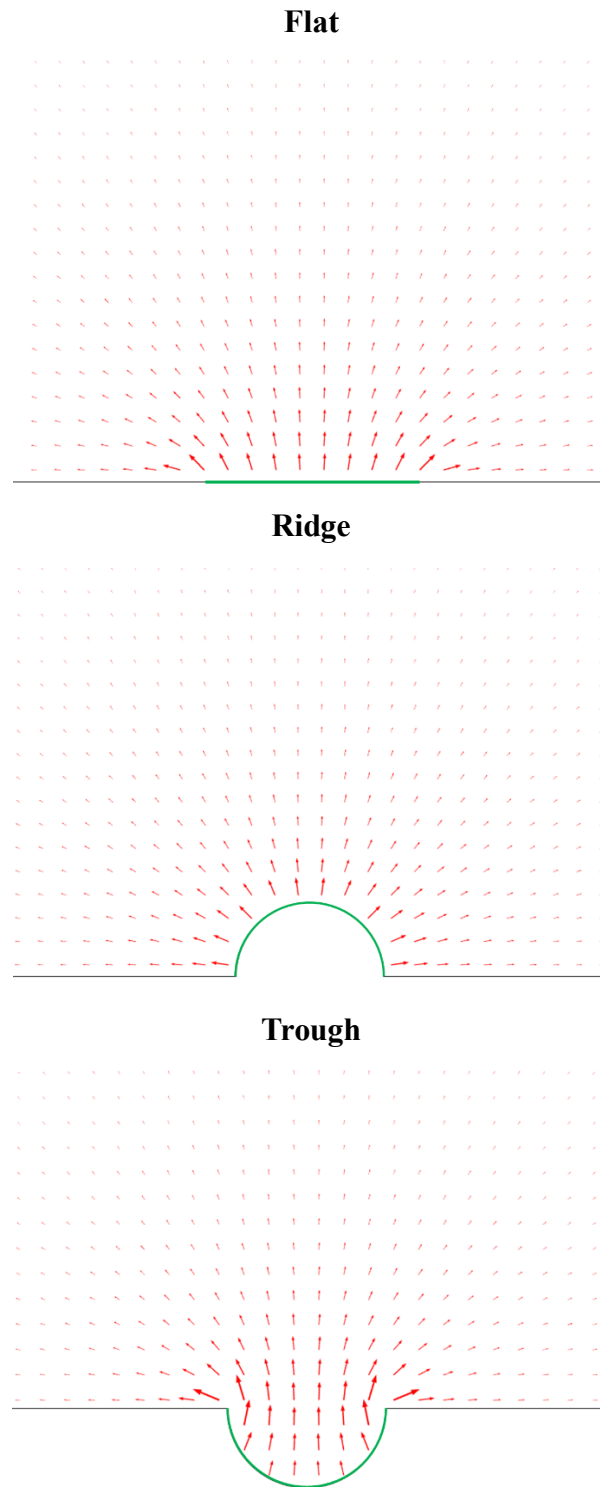


Figure 5.2. The diffusion pattern associated with flat, ridge, and trough-shaped electrodes. Red arrows are showing the direction of diffusion flux. Green colour denotes the electrode surface.

5.2.2. FEM simulation results

5.2.2.1. *Effects of electrode shape on diffusion*

Figure 5.2 shows the diffusion profile of electroactive molecules upon an electrical excitation for each electrode geometry in the absence of surface obstructions. It can be observed that radial diffusion is the dominant pattern for flat and ridge-shaped electrodes. On the other hand, the diffusion in trough-shaped electrode is constricted through the narrower opening above, and then radial diffusion pattern takes over beyond the opening. The diffusion pattern is reflected by the diffusion impedance of the respective electrodes (Figure 5.3). The diffusion to and from the electrode surface of the ridge-shaped electrode is the most efficient, indicated by the lowest diffusion impedance out of the three being studied. This is because the convex shape of the ridge electrode facilitates the more efficient radial diffusion pattern. In contrast, the constricted diffusion path in trough-shaped electrode means its diffusion impedance is the highest. The diffusion efficiency of the flat electrode is somewhere between the other two designs but very similar to that of the ridge-shaped electrode.

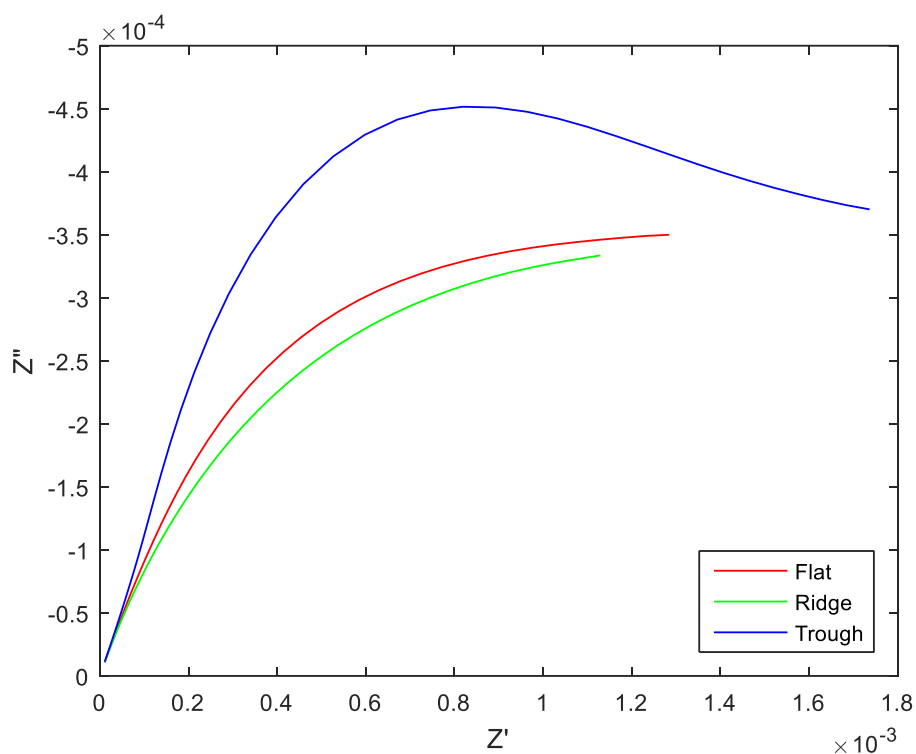


Figure 5.3. Nyquist plot of the diffusion impedance of bare electrodes for the three electrode geometries in this study. The plotted frequency range is 0.1 Hz to 10 kHz.

Diffusion distance is the propagation distance of the concentration perturbation of electroactive species upon an electrical excitation. It dictates the extent from the electrode surface where diffusion would occur. The diffusion distance increases with lower excitation frequency. The length of diffusion distance relative to the electrode dimensions has an impact on whether the electrode geometry is relevant in causing a difference in diffusion pattern. The idea is illustrated in Figure 5.4 for trough and flat electrodes, but the same concept can be extended to the ridge electrode. All three electrode shapes would behave essentially as flat electrodes when the diffusion distance is very short in comparison to the electrode geometry (Figure 5.4, 1000 Hz), and most of the diffusion pattern can be considered planar. This effect can also be observed in the diffusion impedance Nyquist plot (Figure 5.3), as the diffusion

impedances for all geometries overlap at the high frequency region (bottom left). On the other hand, the majority of the diffusion happens far above the electrode at very low frequencies (Figure 5.4, 0.1 Hz). In the extreme case of very long diffusion distances, all electrodes can be approximated by a two-dimensional line with a pure cylindrical diffusion pattern. This causes the diffusion impedances of all electrode geometries to converge at low frequencies. The electrode geometry has the most significant effect on the diffusion pattern at some intermediate diffusion distance between these two extreme cases (Figure 5.4, 50 Hz), where flat electrode shows mostly planar diffusion, trough electrode shows constricted diffusion, and ridge electrode shows radial diffusion.

Figure 5.5A shows that the various electrode geometries in this study have an effect on the diffusion process at frequencies below 100 Hz. The magnitude of the diffusion impedance diverges between the three electrode designs below this frequency. Figure 5.5B shows that the relative difference in diffusion impedance is at maximum around 4 Hz, with the trough-shaped electrode showing a positive peak difference and the ridge-shaped electrode showing a negative peak difference in comparison to the flat electrode. These corresponds to characteristic diffusion distances of roughly 1.1 μm (100 Hz) and 5.5 μm (4 Hz). These distances are in a similar scale to the size of the PS beads (diameter of 0.7 μm), which is a preferred criterion for selecting a suitable frequency range for sensing the target analyte (Section 3.2.2). Therefore, the analysis of the diffusion impedance for sensing focused in this frequency range, which means the effect of electrode geometry on the diffusion pattern of the electroactive molecules remains relevant.

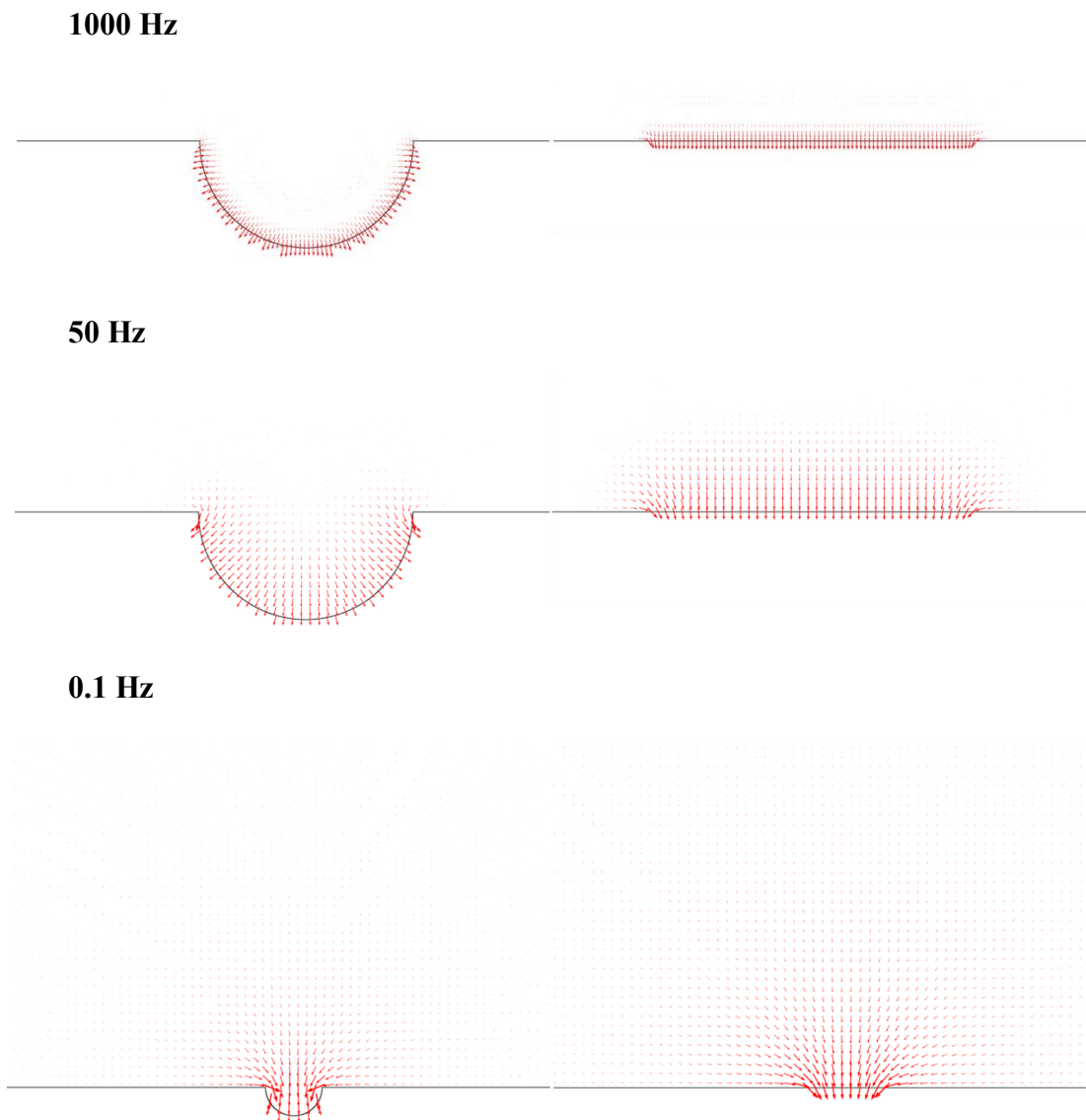
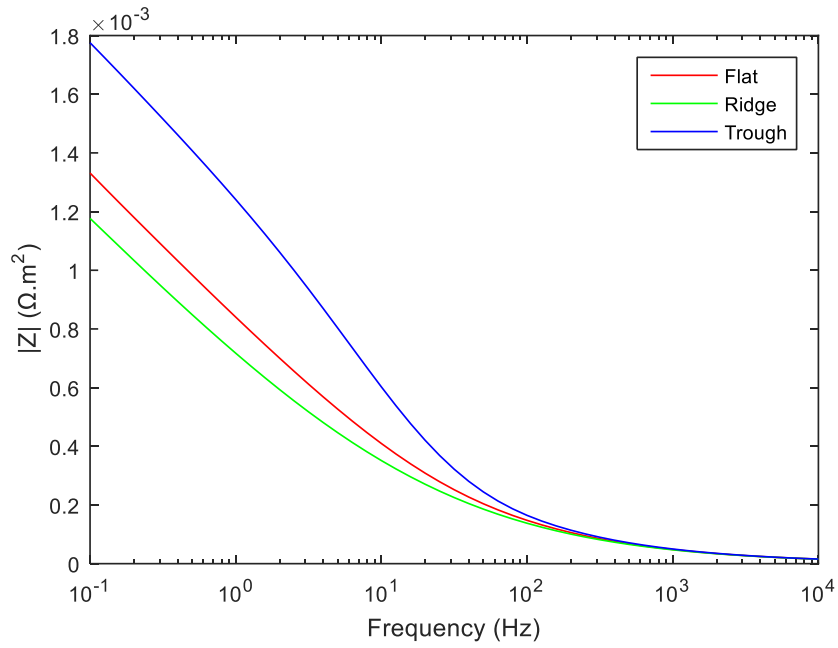


Figure 5.4. The diffusion pattern for trough-shaped (left) and flat (right) electrodes at various excitation frequencies. The arrows represents the diffusion flux. The dimensions for each electrode geometry are the same across the different frequencies and are not drawn to scale.

A.



B.

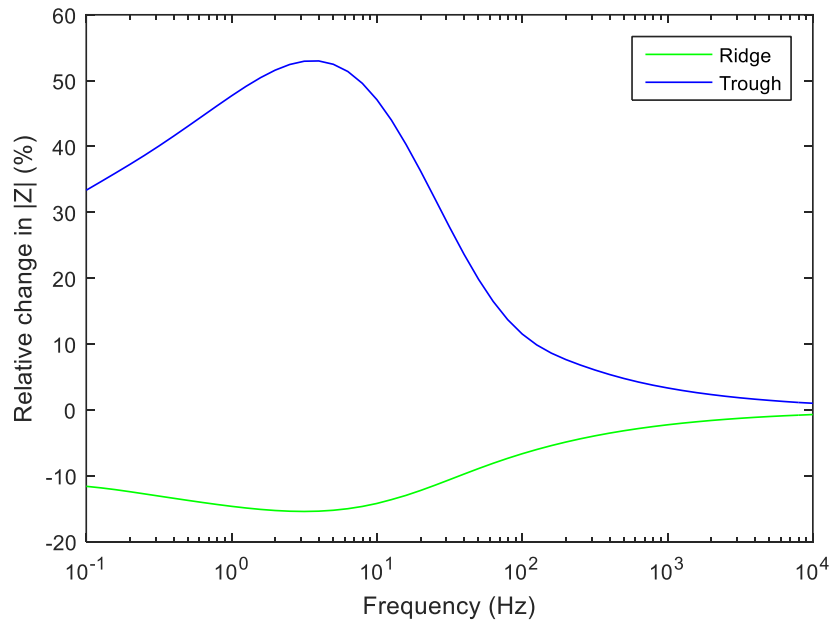


Figure 5.5. A) magnitude of diffusion impedance $|Z|$ for the three electrode geometry. B) the percentage difference in $|Z|$ of the trough and ridge electrodes relative to the flat electrode.

5.2.2.2. *Effects of bound polystyrene beads for different electrode shapes*

Diffusion impedances in the presence of different densities of surface bound PS beads were simulated. The absolute increase in real and imaginary components of the diffusion impedance from the bare electrode of the corresponding geometry are plotted in Figure 5.6. The simulated diffusion impedance is greater in the presence of higher density of bound particles. In general, the real component of the impedance shows greater absolute change in comparison to the imaginary component. From the simulation, trough-shaped electrode is predicted to have the largest impedance change in the presence of immobilised beads, while those for flat and ridge shapes are lower and somewhat comparable. A physical explanation for this observation is that the diffusion in trough-shaped electrode is concentrated due to the concaved geometry, so each immobilised bead obstructs a larger proportion of molecule movement. On the other hand, the radial diffusion patterns seen in flat and ridge-shaped electrodes allow easier bypass of the blockages caused by the immobilised beads.

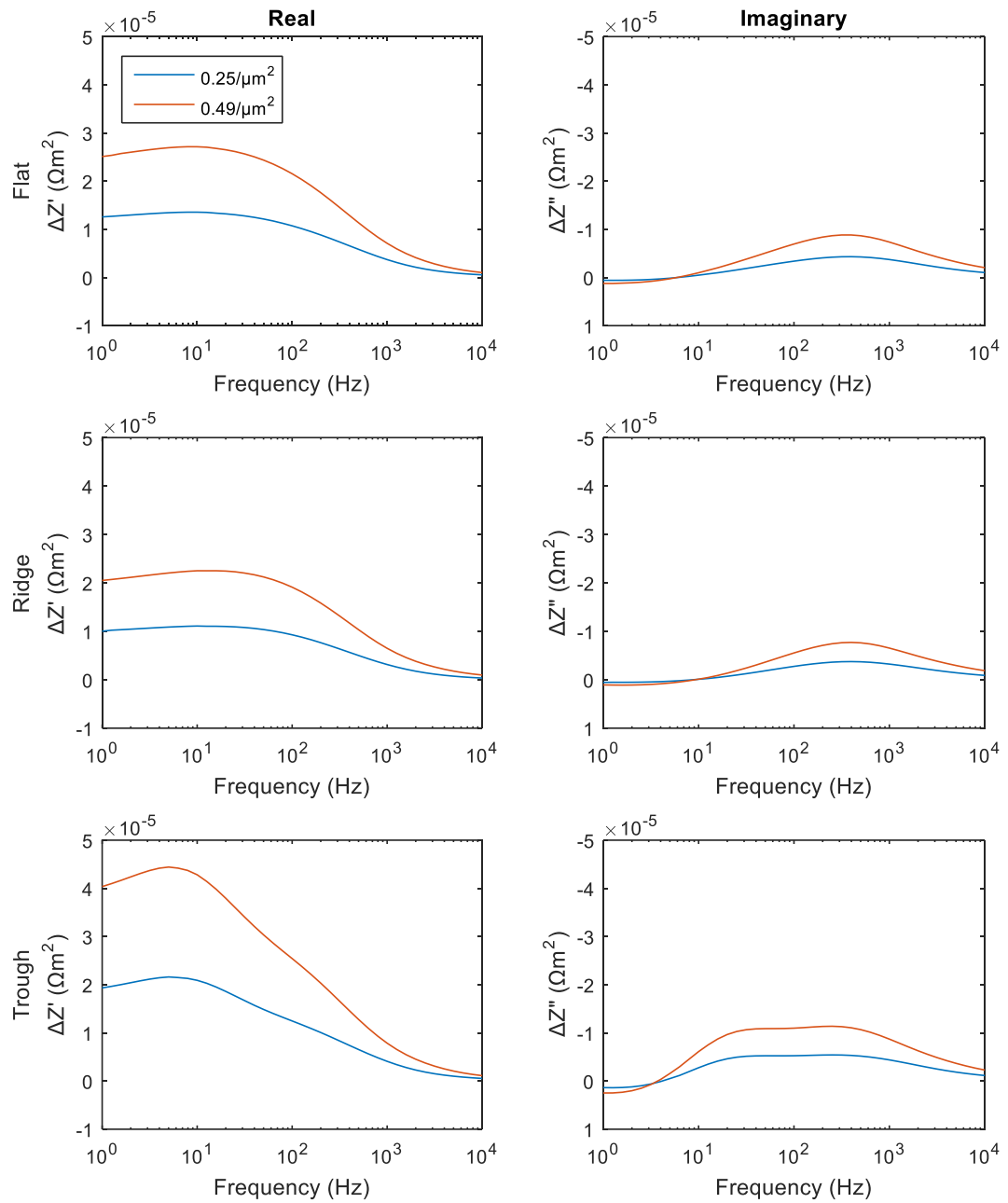


Figure 5.6. Simulated absolute change in diffusion impedance in response to different density of bound PS beads (beads per μm^2) for the different electrode geometries (in order of top to bottom rows: flat, ridge, trough). Left column: change in the real component of the diffusion impedance. Right column: change in the imaginary component of the diffusion impedance.

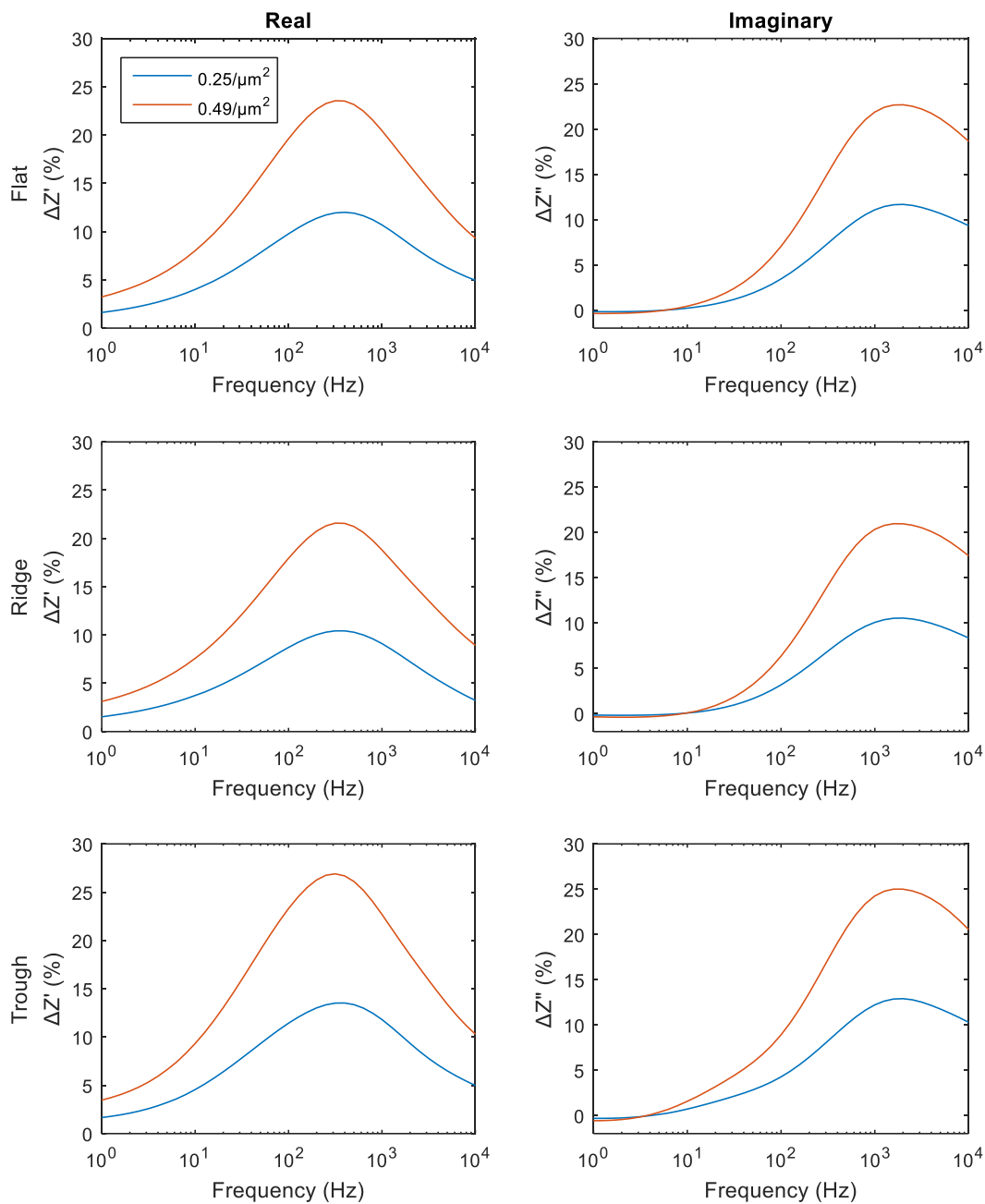


Figure 5.7. Percentage increase in the real or imaginary components of diffusion impedance against the bare electrode for the corresponding electrode shapes for different bound beads densities.

Typically, the relative change in impedance is used in sensing applications in order to normalise the variations between individual sensors. The relative changes in the real and imaginary components are shown in Figure 5.7. The maximum relative change in response to bound PS beads is around 300 Hz for the real component and 1 kHz for the imaginary component. These correspond to characteristic diffusion distances of $\sim 0.6 \mu\text{m}$ and $\sim 0.3 \mu\text{m}$, respectively, which are close to the size of the PS beads analyte. A larger proportion of the overall diffusion profile is disrupted when the diffusion distance matched with the target analyte size, hence the greater change in impedance. However, diffusion impedance is typically observable only at frequencies below 100 Hz for actual electrode impedance measurements.

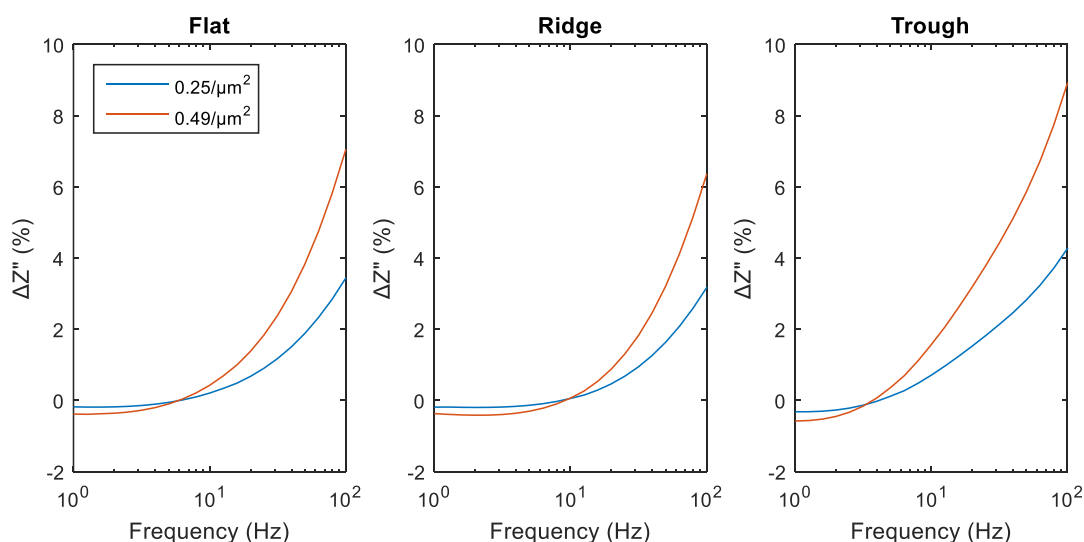


Figure 5.8. Percentage increase in the imaginary components of diffusion impedance against the bare electrode for frequencies 100 Hz and below.

The imaginary component of the impedance was used in further analysis as the indicator for analyte binding. This was to isolate the diffusion component from other circuit components of the electrochemical system as discussed in Section 3.3.3.1. The

simulated percentage change in the imaginary component from Figure 5.7 is plotted again but for the frequency range of 1-100 Hz (Figure 5.8), as this is the typical range where diffusion impedance is observable in experimental data. The simulation shows that the relative change increases with frequency in this range, and a greater change is associated with higher beads density. It is also observed this relative change in the imaginary component persists at lower frequencies for the trough-shaped electrode, while the change quickly drops towards zero with decreasing frequency for the flat and ridge-shaped electrodes. Again, the trough-shaped electrode exhibits greater impedance change in response to analyte binding in this frequency range when compared to the flat and ridge-shaped electrodes, which can be explained by the concentrated or radial diffusion patterns associated with the different electrode shapes. This relative imaginary component change was used as the sensor readout to assess the sensitivities of the different electrode shapes in actual experiment.

Numerical modelling predicted limited performance advantage with the ridge-shaped electrode over the flat geometry. Additionally, difficulties were encountered with the fabrication of ridge-shaped electrodes. Consequently, the ridge-shaped electrode was not subjected to experiment testing, and the sensitivities of flat and trough-shaped electrodes were compared experimentally with the sensing of immobilised PS beads.

5.3. Experimental validation

Electrodes were functionalised with a polypyrrole conducting polymer and avidin probes in the same process described in Section 3.3.1. Subsequently, the functionalised electrodes were incubated with biotin-coated PS beads in PBS at the concentration of

1% w/v for 30 minutes to immobilise the analyte on the electrode surface. The impedance was also recorded in the same manner as in Section 3.3.1.

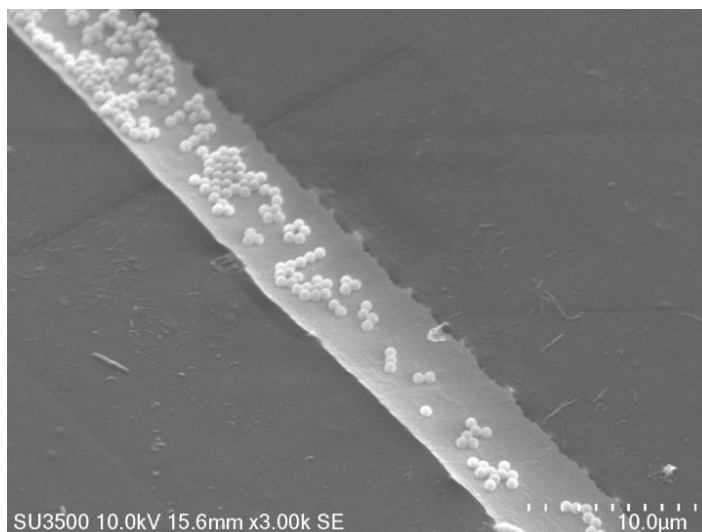


Figure 5.9. Scanning electron microscopy photo of immobilised PS beads on trough-shaped electrode.

5.3.1. Polystyrene beads binding on the microelectrodes

Each electrode was examined under a scanning electron microscope to count the number of immobilised beads at the end of the experiment (Figure 5.9). The binding density was not determined in the same way as percentage of coverage as in Section 3.3.1. This was because the curved surface of the trough-shaped electrode meant it was difficult to measure the percentage coverage accurately using microscopy. Therefore, the number of beads were counted instead, ignoring the variations in size of each PS bead. The densities of bound PS beads were found to be on average 0.37 beads per μm^2 of electrode area. No significant difference was found in the binding density between the flat and trough-shaped electrodes.

Typically a higher rate of target immobilisation would be expected for electrodes with faster rate of diffusion, as the analyte would approach the sensor surface at a higher rate to be captured due to the random Brownian movement. So flat electrode in this

case might be expected to exhibit more binding. However, the PS beads used in this study did not diffuse freely, but sank to the bottom of the solution and onto the electrode surface. Additionally, the relatively high beads concentration used for incubation probably caused saturation of PS beads binding to the electrode surface. Under these circumstances, the binding kinetics between the avidin probe and the beads' biotin coating was the main determinant for the immobilisation of the particle, which was indifferent for both electrode shapes. Since the PS particle binding rate was the same, the sensor response between the two electrode designs could be compared directly without adjusting for analyte binding efficiency.

The binding rate of 0.37 beads per μm^2 translates to a coverage of roughly 14%. This binding rate is significantly lower than the macro flat electrode used in Chapter 3, which has a coverage rate of close to 50% when incubated with the same beads concentration of 1% w/v. A reason for this observation may be the fabrication process of the microelectrodes interfered with the biofunctionalisation of the electrode with polypyrrole conducting polymer and the avidin probes, leading to a reduced number of avidin probes and active surface area available to capture the PS beads.

5.3.2. Impedance and sensor response of three-dimensional microelectrodes

Figure 5.10 shows the Randles circuit model fitting of the impedance spectrum of a flat microelectrode deposited with polypyrrole conducting polymer and avidin probes. The experiment data was fitted to Randles circuit using the FEM simulated diffusion impedance for a bare flat electrode digit using the same method developed in Section 3.3.2.2. The fitted model parameters are summarised in Table 5.1. The fitted diffusion coefficient D_S of $7.0668 \times 10^{-10} \text{ m}^2 \cdot \text{s}^{-1}$ is within the range of the expected value [132, 139], although this value is slightly lower than the model fitting of the macro flat

electrode impedance in Section 3.3.2.1. A possible reason for this result is a lower active electrode area, perhaps a result of the fabrication process, which may be connected to the lower PS beads coverage rate observed for the microelectrode in comparison to the macro flat electrode. Nevertheless, the relatively good fitting results with expected parameter values is evidence supporting that the observed impedance at low frequency range is mostly governed by the diffusion of the ferrocyanide/ferricyanide redox couple.

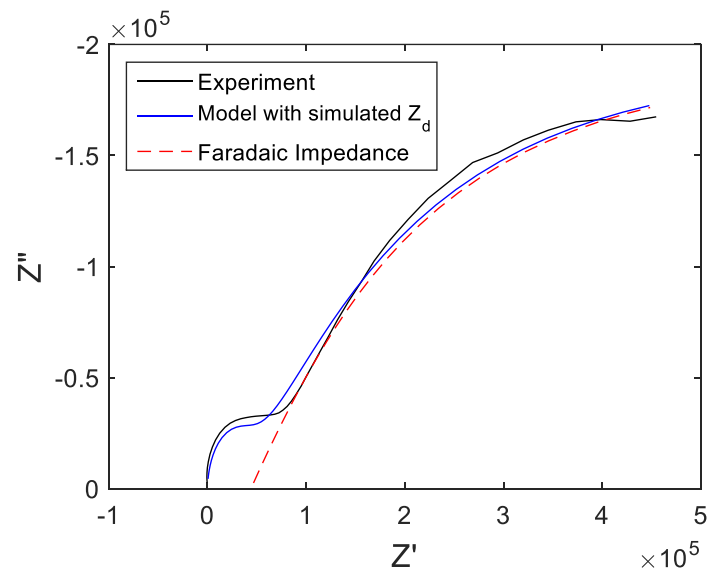


Figure 5.10. Fitting of an experimental flat microelectrode impedance with Randles circuit using FEM simulated diffusion impedance.

TABLE 5.1. FITTING PARAMETERS OF IMPEDANCE FITTING IN FIGURE 5.10

Model parameters	Fitting values
R_{sol}	200.045 Ω
Z_{dl-Q}	6.3125×10^{-10} F
$Z_{dl-\alpha}$	0.9858
R_{ct}	44029.8 Ω
D_S	7.0668×10^{-10} $m^2 \cdot s^{-1}$
RSS	1.64119×10^9

The change in diffusion impedance before and after PS beads incubation were analysed to assess the effects of PS beads immobilisation. The analysis approach using the apparent diffusion number in Chapter 3 was not applicable for the microelectrodes used in this chapter, as the method required the diffusion impedance to be a Warburg element that is associated with planar diffusion pattern observed in large flat electrodes.

Numerical simulation suggested that the imaginary component of the impedance does not change significantly in response to immobilised submicron particles at frequencies below 10 Hz. Therefore, the imaginary component of the impedance at 1 Hz was used to normalise the impedance of each measurements (Equation 5.1) to reduce the effect of random errors caused by factors such as electrode area, temperature, and redox couple concentration. The normalised imaginary component $Z''^{\circ}(\omega)$ is used in the subsequent analyses.

$$Z''^{\circ}(\omega) = Z''(\omega)/Z''_{1Hz}$$

(Equation 5.1)

Z''° : normalised imaginary component

Figure 5.11 shows the percentage change in normalised imaginary component of an experimentally recorded impedance for a trough-shaped electrode after incubation with PS beads. In comparison to the theoretical simulation in Figure 5.8, the percentage change is much greater in the experimentally observed impedance than the simulation. One explanation for this amplified change is non-specific drift in impedance value, as electrodes incubated with only PBS buffer solution also exhibited some increase in the normalised imaginary component. Similar observation was seen with the macroelectrode used in Chapter 3 (Section 3.3.3.2), although to a lesser extent. Another explanation could be that additional PS beads were removed during the process between

impedance acquisition and the counting of the immobilised PS beads under microscopy, leading to underestimation of the beads density at the time of impedance acquisition. Lastly, the actual size of PS beads used in the experiment was slightly larger in diameter ($0.74 \mu\text{m}$) than the dimension used for simulation ($0.70 \mu\text{m}$), which could contribute to a higher change in impedance seen in the experiment. However, the experimental data show a general pattern of increasing difference in the percentage change in normalized imaginary component at higher frequencies, similar to the numerical simulation.

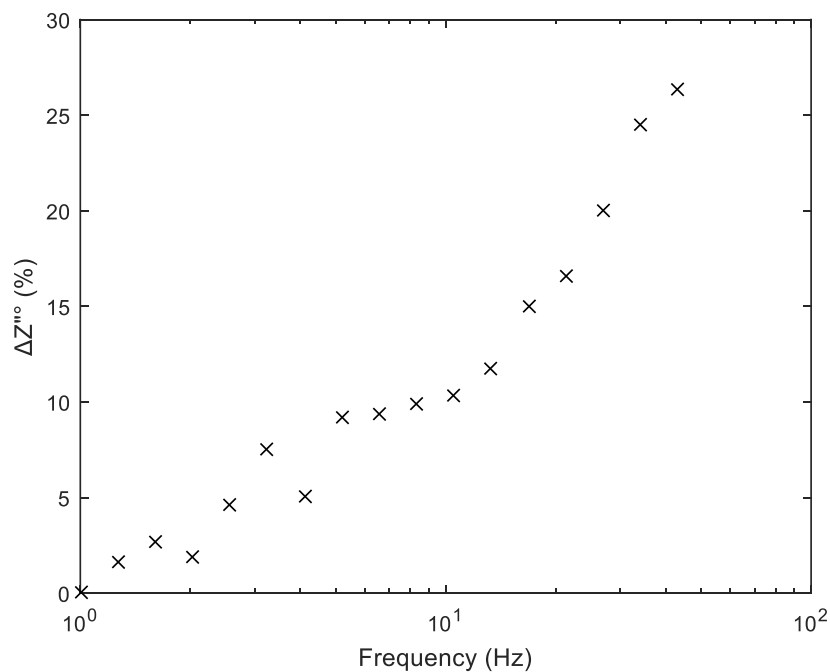


Figure 5.11. The percentage increase in the imaginary component of the electrode impedance against frequency after PS beads immobilisation for a trough-shaped electrode with ~ 0.37 beads per μm^2 coverage.

The percentage change in the normalised imaginary component at 20 Hz after immobilisation of PS beads ($\Delta Z''(20 \text{ Hz})$) was calculated and the data is presented in Figure 5.12. The results showed that trough-shaped electrodes exhibited greater impedance change in response to immobilised PS beads, which agreed with the numerical simulation.

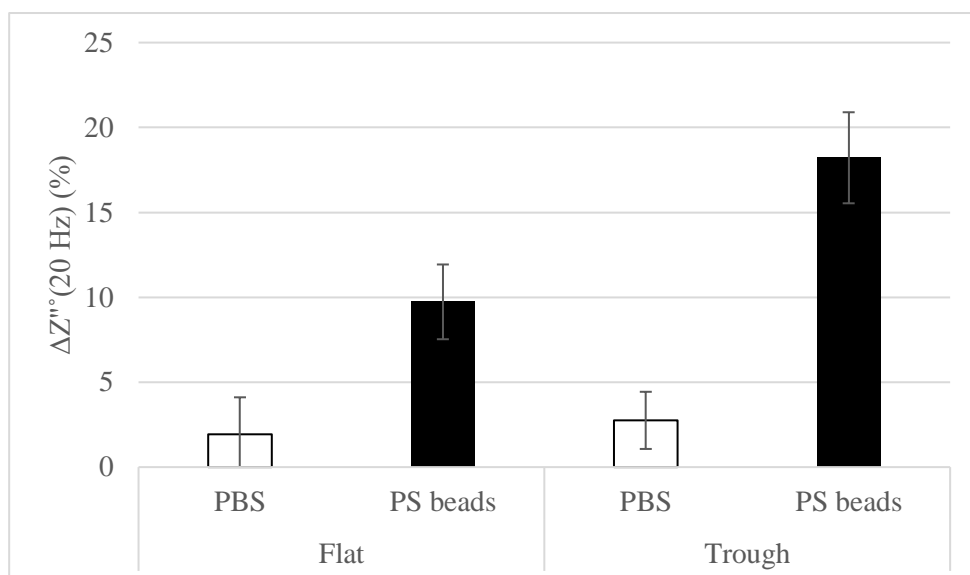


Figure 5.12. Sensor response for flat and trough-shaped electrodes. The signals are expressed as the normalised relative change in imaginary component at 20 Hz after PS beads immobilisation.

5.4. Conclusion

Different three-dimensional electrode geometries, namely flat, ridge, and trough shapes, were investigated for their response sensitivity for analyte recognition. The change in electrode impedance, which reflects captured analyte, was simulated based on blocked diffusion of electroactive molecules. The trough-shaped electrode was predicted to give greater change in impedance in response to immobilised analyte. This was because the concaved shape of trough electrodes caused the diffusion flux to concentrate above the electrode, thus each analyte caused a greater proportion of the diffusion flux to be obstructed. Sensing experiment was performed using the flat and trough-shaped electrodes, and the results agreed with simulations in that trough-shaped electrode demonstrated greater sensitivity.

6. Research Contributions and Future Works

6.1. Significance of findings

The work investigated the effects of electrode three-dimensional geometry on faradaic mode electrochemical impedance biosensors. Electrode geometry affects the faradaic process through modulating the diffusion pattern. The conventional use of charge transfer resistance as the indicator for analyte recognition does not capture this influence on the diffusion pattern. Therefore, an alternative modelling approach using the diffusion impedance for explaining how the faradaic process is involved in electrochemical impedance biosensors was developed.

The popularity of using charge transfer resistance as the indicator for analyte recognition may be because of its trivial concept and simple mathematical description. The charge transfer resistance can be simplified to a single resistance component of a constant and real value, independent of the excitation frequency. In comparison, diffusion impedance is a complex number that change with excitation frequency. Furthermore, the diffusion impedance can vary greatly depending on the specific geometry of the electrode and fluidics involved, and there are no mathematical equations available to describe all the possible situations. This can create difficulties for using the diffusion impedance in more advanced data analysis. Researchers often circumvent this problem by assuming planar diffusion patterns and approximating the diffusion impedance with a Warburg element. This may be a viable approach as all diffusion patterns approach the semi-infinite planar pattern at high frequencies. By focusing the data analysis on the higher frequency range, the diffusion patterns involved may be sufficiently planar for the Warburg element to provide an adequate model fitting.

The lack of appropriate models and analysis techniques also meant the diffusion component of the faradaic process has so far been mostly disregarded in biosensor applications. However, the modelling investigation in this work had suggested that obstructed diffusion due to immobilised analyte can produce an observable change in the diffusion component of the overall electrode impedance. This concept introduces new considerations for biosensor research, one of such example is the effects of electrode geometry investigated in this work.

Diffusion impedance is related to the movement of electroactive molecules, which carries electrons to and away from the electrode to generate current flow. The flux of these molecules can be intuitively modelled in the three-dimensional space around the electrode surface, using numerical approaches such as FEM applied in this work. The FEM model can be used to describe the effects of different electrode geometries on the faradaic process by simulating the diffusion pattern. In addition, the results of this work suggested that captured micron-sized spherical analyte can cause an observable change to the diffusion impedance that can be adequately modelled with FEM. A data fitting approach was developed to fit a numerically simulated diffusion impedance to experimentally observed impedance. The method fit a table of simulated diffusion impedance values to the experiment data by varying the diffusion coefficient according to Equation 3.8 in Section 3.3.2.2. The approach circumvents the requirement for analytical solutions of diffusion impedance to perform data fitting. This method is applicable for fitting any diffusion impedance component with a diffusion pattern known a priori and that can be simulated by numerical methods. This provides a tool to analysing diffusion impedance in situations with more complex sensor geometries. An additional fitting parameter that proportionally scales the impedance may be introduced to consider factors such as electrode area, temperature, and redox molecule

concentration. However, having too many fitting parameters can lead to problems with overfitting a solution, so the data fitting of diffusion impedance in this work was limited to varying the diffusion impedance only.

An important property for diffusion is the diffusion distance, which is dependent on the frequency of the excitation signal in electrochemical impedance spectroscopy. Theoretically it is preferable to have a diffusion distance that is equal to or less than the size of the analyte being detected. This would cause proportionally greatest disturbance to the overall diffusion profile, and thus the greatest proportional change in impedance. This is a similar concept practiced by adjusting the dimensions of interdigitated electrodes for non-faradaic measurements, with the intent to concentrate the electric field in a layer above the electrode surface that matches the height of the detected analyte [111, 117]. As the topic of diffusion has been largely ignored in previous biosensing research, this aspect of the faradaic process has been largely overlooked. This presents a new element of optimisation for faradaic mode impedance biosensors, and this knowledge may be developed in the future for selective sensing of analytes based on size. For instance, by analysing the impedance change at different frequency points (different diffusion distance), one may be able to deduce the impedance change caused by analytes of a certain size. This may help with the exclusion of signals caused by contaminants or background molecules of different sizes compared to the analyte of interest and improve the reliability of sensor readout.

This work investigated how sensor performance is affected by three-dimensional electrode geometry by comparing flat, ridge, and trough-shaped electrodes. The findings suggested the trough-shaped electrode exhibits enhanced sensor sensitivity due to focussing of diffusion flux by the concaved geometry, causing a relatively higher proportion of mass transfer to be obstructed by each captured analyte. This idea is

analogous to the method applied in non-faradaic mode impedance biosensor, in which the concentration of electric field at binding locations of the analyte is used in order to cause a greater current change upon analyte immobilisation.

Analyte sensing can be thought of in two steps. The first is the immobilisation of the target analyte onto the sensor's surface, and the second is the transduction of this binding event to a signal for readout. The restricted diffusion pattern in trough-shaped electrodes enhances the second step by increasing the sensor response upon analyte binding. However, it may be counterproductive for capturing of target analyte in the first step. The smaller opening available for the analytes to diffuse into the trough and bind with the electrodes surface may reduce the analyte capture rate. The lower binding rate may adversely affect the ability of the sensor to capture targets when they are in low concentrations in the sample solution. This creates a trade-off between efficiency of analyte binding and magnitude of signal transduction for achieving improved limits of detection. Methods for mitigating the reduced binding rate may be to use longer sample incubation times or probes with higher affinity.

Previous studies have used porous or rough electrode surfaces for improved sensor sensitivity [42, 107]. The arguments for the improved performance are usually related to the increased surface area allowing more analyte binding and increased baseline current signal. However, the increase in surface area cannot be the only contributing factor, because such explanation would imply a similar effect can be achieved simply by using a larger electrode. In contrast, it is also commonly believed that miniaturisation of electrode provides improved sensitivity. These two point of views contradict with each other. The advantages provided by porous electrodes may be a result of its surface geometry. The rough surface of porous electrodes increases the surface area available for current to conduct for the same sensor area. This has a similar effect as the trough-

shaped electrode in this study in which current originating from a larger electrode surface is concentrated through a smaller space. This increases the current of the overall sensor, but most importantly the presence of an analyte blocks more current in comparison to a flat electrode with the same area. This increases the magnitude of signal response for each recognised analyte and improves the limit of detection of a sensor.

Although the research in this work used electrochemical impedance spectroscopy technique to perform measurements, the finding here also applies to other techniques such as amperometry or voltammetry. Impedance spectroscopy is a technique that represents information in the frequency domain. In contrast, amperometry and voltammetry represents the same information in the time domain. Theoretically, the data from the different techniques can be directly related through mathematical transformation such as Fourier transformation. Impedance spectroscopy was selected for this study because the information for diffusion is presented most clearly in the form of impedance. However, the acquired data are a result of the same physical processes that operate in electrochemical systems for all measurement techniques. The observations of diffusion impedance have equivalent changes in the current plots of amperometry or voltammetry. Since diffusion is a slow process, it dominates at low frequencies in impedance measurements. On the other hand, diffusive current would become the rate limiting process for amperometry at longer time points after the initial perturbation. For instance, the greater impedance increase at low frequencies with trough-shaped electrode upon analyte recognition would imply a greater reduction in measured current at large time points for amperometry measurements.

The basis for analyte detection used in this work was the reduced faradaic current caused by obstructing the electroactive molecules from exchanging electrons with the electrode surface. Another common mechanism of detection is when the target analyte

itself exchanges electron with the electrode upon recognition, thus driving a current flow. The performance for this type of electrochemical sensor relies on how efficiently the target analyte can approach the electrode surface to initiate charge transfer. In this case, trough-shaped electrode would be counterproductive as the diffusion to and from the electrode surface and the bulk solution is less efficient due to the constricted diffusion pattern. In contrast, the ridge-shaped electrodes exhibit faster diffusion rate due to the protruding shape, which promotes radial diffusion. The ridge-shaped electrode would be expected to be a better choice of shape for this alternative detection mechanism.

6.2. Future research directions

The work in this thesis selected three electrode shapes as general representations for electrodes with flat, protruding, and recessed geometry. Dimensions of the electrodes were mostly restricted by the fabrication approach that was employed. Ideally the dimension of the electrodes should be in a comparable scale with the analyte so that discrepancies in diffusion pattern caused by geometrical differences is relevant in the analyte detection. The use of AZ 1518 photoresist in hard contact photolithography provided patterning of the photoresist with resolution of less than 1 μm . This error is acceptable for patterns with 10 μm dimensions. Therefore, a relatively large analyte was selected, which was the polystyrene microbeads. To apply the same knowledge to sensing of proteins or DNAs, methods of fabricating similar structures at nanometre scale is required.

Trough and ridge shapes were selected due to ease of sensor fabrication. To further enhance the effects of geometry on diffusion pattern, dome and pore-shaped electrodes can be applied. These shapes were not used in this study due to the difficult task of

making electrical connection to each isolated dome or pore within the sensor. However, since dome and pore shapes exhibit the geometric effect in one more dimension than the ridge and trough-shaped electrodes, it is expected the effect of electrode geometry on the sensor property will be accentuated.

The use of photoresist reflow for creating the three-dimensional structures limited the variety of geometry that can be achieved. More specific designs can be investigated to further improve the sensor performance. For instance, troughs with higher aspect ratio can be used to focus the flux of molecules originating from larger electrode area through an even smaller opening in attempt to further improve the sensitivity of a sensor. Other shapes, such as triangles, may also be considered.

6.3. Conclusion

In this thesis, we investigated the effects of three-dimensional electrode geometries has on faradaic electrochemical impedance biosensor, based on the principle of modulated diffusion pattern. The model target analyte used in the study was micron-sized polystyrene beads.

In Chapter 3, a finite element model for simulating the change in diffusion impedance in response to the immobilisation of the polystyrene beads was developed based on blockage of diffusion flux. The model predicted an observable impedance change upon analyte recognition. Subsequently, the model was validated with experiment data. In order to compare the model simulation and measured impedance, a method of data fitting was developed to fit experimentally measured impedance to an Randles circuit that used numerically simulated table of diffusion impedance. This method allows data fitting of electrode impedance with any pattern of diffusion that can be simulated. Model fitting of the of experimentally measured impedance with surface

immobilised polystyrene beads showed good agreement with the numerical simulation, suggesting that change in faradaic impedance caused by captured analyte could be understood as blocked diffusional mass transfer of electroactive species. Furthermore, the change in diffusion impedance component could be used as the indicator of analyte recognition in biosensor applications.

Chapter 4 detailed the fabrication process that was developed to create flat, ridge, and trough-shaped electrode digits. Photoresist reflow was used to create a master template of ridge structures. Subsequently, electroforming process was used to copy the image of the master template onto nickel stamps. The nickel stamps were used to replicate the geometries onto PETG substrates by hot embossing. Finally the gold electrode digits were created using wet etching photolithography. Flat and trough-shaped electrodes were successfully created with a transverse width of 10 μm .

In Chapter 5, the diffusion impedance model developed in Chapter 3 was applied in the investigation of the effects of three-dimensional electrode geometries on biosensing. The model simulation predicted that trough-shaped electrodes would exhibit greater impedance response in the presence of analyte blocking the diffusion of electroactive molecules. This was related to the concentration of diffusion flux seen for the concaved trough-shaped electrode. This caused a greater proportion of diffusion flux being obstructed by each unit of immobilised analyte. This theoretical result was validated in an actual sensing experiment with the trough-shaped electrode exhibiting a greater change in impedance upon analyte recognition.

The finding of this work can contribute to a better understanding of the signal transduction in electrochemical impedance biosensor. The knowledge may be applied in future for designing new sensors with improved performances.

Bibliography

- [1] H. Sharma and R. Mutharasan, "Review of biosensors for foodborne pathogens and toxins," *Sensors and Actuators B: Chemical*, vol. 183, no. 0, pp. 535-549, 7/5/ 2013.
- [2] E. C. Alocilja and S. M. Radke, "Market analysis of biosensors for food safety," *Biosensors and Bioelectronics*, vol. 18, no. 5–6, pp. 841-846, 5// 2003.
- [3] H. Vaisocherová-Lísalová *et al.*, "Low-fouling surface plasmon resonance biosensor for multi-step detection of foodborne bacterial pathogens in complex food samples," *Biosensors and Bioelectronics*, vol. 80, pp. 84-90, 2016/06/15/ 2016.
- [4] K.-M. Lee, M. Runyon, T. J. Herrman, R. Phillips, and J. Hsieh, "Review of Salmonella detection and identification methods: Aspects of rapid emergency response and food safety," *Food Control*, vol. 47, pp. 264-276, 2015/01/01/ 2015.
- [5] M. L. Verma, "Nanobiotechnology advances in enzymatic biosensors for the agri-food industry," *Environmental Chemistry Letters*, journal article pp. 1-6, 2017.
- [6] V. Scognamiglio, F. Arduini, G. Palleschi, and G. Rea, "Biosensing technology for sustainable food safety," *TrAC Trends in Analytical Chemistry*, vol. 62, pp. 1-10, 2014/11/01/ 2014.
- [7] A. Ahmed, J. V. Rushworth, N. A. Hirst, and P. A. Millner, "Biosensors for Whole-Cell Bacterial Detection," *Clinical Microbiology Reviews*, vol. 27, no. 3, pp. 631-646, July 1, 2014 2014.
- [8] M. L. Y. Sin, K. E. Mach, P. K. Wong, and J. C. Liao, "Advances and challenges in biosensor-based diagnosis of infectious diseases," *Expert review of molecular diagnostics*, vol. 14, no. 2, pp. 225-244, 02/13 2014.
- [9] B. Bohunicky and S. A. Mousa, "Biosensors: the new wave in cancer diagnosis," *Nanotechnology, Science and Applications*, vol. 4, pp. 1-10, 12/30 2011.
- [10] P.-W. Yen *et al.*, "Emerging Electrical Biosensors for Detecting Pathogens and Antimicrobial Susceptibility Tests," *Current Organic Chemistry*, vol. 18, no. 2, pp. 165-172, // 2014.
- [11] J. Kirsch, C. Siltanen, Q. Zhou, A. Revzin, and A. Simonian, "Biosensor technology: recent advances in threat agent detection and medicine," *Chemical Society Reviews*, 10.1039/C3CS60141B vol. 42, no. 22, pp. 8733-8768, 2013.
- [12] M. U. Ahmed, I. Saaem, P. C. Wu, and A. S. Brown, "Personalized diagnostics and biosensors: a review of the biology and technology needed for personalized

- medicine," *Critical Reviews in Biotechnology*, vol. 34, no. 2, pp. 180-196, 2014/06/01 2014.
- [13] A. Bah, S. K. Balasundram, and M. H. A. Husni, "Sensor Technologies for Precision Soil Nutrient Management and Monitoring," *American Journal of Agricultural and Biological Science*, vol. 7, no. 1, pp. 43-49, 2012.
- [14] V. I. Adamchuk, J. W. Hummel, M. T. Morgan, and S. K. Upadhyaya, "On-the-go soil sensors for precision agriculture," *Computers and Electronics in Agriculture*, vol. 44, no. 1, pp. 71-91, 7// 2004.
- [15] N. Verma and A. Bhardwaj, "Biosensor Technology for Pesticides—A review," *Applied Biochemistry and Biotechnology*, journal article vol. 175, no. 6, pp. 3093-3119, 2015.
- [16] H. E. Indyk, B. D. Gill, and D. C. Woollard, "An optical biosensor-based immunoassay for the determination of bovine serum albumin in milk and milk products," *International Dairy Journal*, vol. 47, pp. 72-78, 2015/08/01/ 2015.
- [17] J. Wang *et al.*, "DNA electrochemical biosensors for environmental monitoring. A review," *Analytica Chimica Acta*, vol. 347, no. 1, pp. 1-8, 1997/07/30 1997.
- [18] M. R. Gartia *et al.*, "The microelectronic wireless nitrate sensor network for environmental water monitoring," *Journal of Environmental Monitoring*, 10.1039/C2EM30380A vol. 14, no. 12, pp. 3068-3075, 2012.
- [19] F. Long, A. Zhu, and H. Shi, "Recent Advances in Optical Biosensors for Environmental Monitoring and Early Warning," *Sensors*, vol. 13, no. 10, p. 13928, 2013.
- [20] J. Barton *et al.*, "Screen-printed electrodes for environmental monitoring of heavy metal ions: a review," *Microchimica Acta*, journal article vol. 183, no. 2, pp. 503-517, 2016.
- [21] L. T. Bereza-Malcolm, G. Mann, and A. E. Franks, "Environmental Sensing of Heavy Metals Through Whole Cell Microbial Biosensors: A Synthetic Biology Approach," *ACS Synthetic Biology*, vol. 4, no. 5, pp. 535-546, 2015/05/15 2015.
- [22] C. Chen *et al.*, "Recent advances in electrochemical glucose biosensors: a review," *RSC Advances*, 10.1039/C2RA22351A vol. 3, no. 14, pp. 4473-4491, 2013.
- [23] M. J. Bradshaw, S. Farrow, R. W. Motl, and T. Chitnis, "Wearable biosensors to monitor disability in multiple sclerosis," *Neurology: Clinical Practice*, vol. 7, no. 4, pp. 354-362, August 1, 2017 2017.
- [24] A. Sonawane, P. Manickam, and S. Bhansali, "Stability of Enzymatic Biosensors for Wearable Applications," *IEEE Reviews in Biomedical Engineering*, vol. PP, no. 99, pp. 1-1, 2017.

- [25] R. L. Caygill, G. E. Blair, and P. A. Millner, "A review on viral biosensors to detect human pathogens," *Analytica Chimica Acta*, vol. 681, no. 1, pp. 8-15, 2010/11/29/ 2010.
- [26] A. Mortari and L. Lorenzelli, "Recent sensing technologies for pathogen detection in milk: A review," *Biosensors and Bioelectronics*, vol. 60, pp. 8-21, 2014/10/15/ 2014.
- [27] K. R. Rogers, "Principles of affinity-based biosensors," *Molecular Biotechnology*, journal article vol. 14, no. 2, pp. 109-129, February 01 2000.
- [28] H. Cao, Y. Zhu, L. Tang, X. Yang, and C. Li, "A Glucose Biosensor Based on Immobilization of Glucose Oxidase into 3D Macroporous TiO₂," *Electroanalysis*, vol. 20, no. 20, pp. 2223-2228, 2008.
- [29] D. Nidzworski, P. Pranszke, M. Grudniewska, E. Król, and B. Gromadzka, "Universal biosensor for detection of influenza virus," *Biosensors and Bioelectronics*, vol. 59, pp. 239-242, 9/15/ 2014.
- [30] S. M. Radke and E. C. Alocilja, "A high density microelectrode array biosensor for detection of E. coli O157:H7," *Biosensors and Bioelectronics*, vol. 20, no. 8, pp. 1662-1667, 2005/02/15/ 2005.
- [31] M. S. Mannoor, S. Zhang, A. J. Link, and M. C. McAlpine, "Electrical detection of pathogenic bacteria via immobilized antimicrobial peptides," *Proceedings of the National Academy of Sciences*, vol. 107, no. 45, pp. 19207-19212, November 9, 2010 2010.
- [32] J. Jantra, P. Kanatharana, P. Asawatreratanakul, M. Hedström, B. Mattiasson, and P. Thavarungkul, "Real-time label-free affinity biosensors for enumeration of total bacteria based on immobilized concanavalin A," *Journal of Environmental Science and Health, Part A*, vol. 46, no. 13, pp. 1450-1460, 2011/11/01 2011.
- [33] A. Singh, S. Poshtiban, and S. Evoy, "Recent Advances in Bacteriophage Based Biosensors for Food-Borne Pathogen Detection," *Sensors*, vol. 13, no. 2, p. 1763, 2013.
- [34] M. Tolba, M. U. Ahmed, C. Tlili, F. Eichenseher, M. J. Loessner, and M. Zourob, "A bacteriophage endolysin-based electrochemical impedance biosensor for the rapid detection of Listeria cells," *Analyst*, 10.1039/C2AN35988J vol. 137, no. 24, pp. 5749-5756, 2012.
- [35] C. Berggren, P. Stålhandske, J. Brundell, and G. Johansson, "A Feasibility Study of a Capacitive Biosensor for Direct Detection of DNA Hybridization," *Electroanalysis*, vol. 11, no. 3, pp. 156-160, 1999.

- [36] F. Yan, A. Erdem, B. Meric, K. Kerman, M. Ozsoz, and O. A. Sadik, "Electrochemical DNA biosensor for the detection of specific gene related to *Microcystis* species," *Electrochemistry Communications*, vol. 3, no. 5, pp. 224-228, 2001/05/01/ 2001.
- [37] B. Zhu, O. A. Alsager, S. Kumar, J. M. Hodgkiss, and J. Travas-Sejdic, "Label-free electrochemical aptasensor for femtomolar detection of 17 β -estradiol," *Biosensors and Bioelectronics*, vol. 70, pp. 398-403, 8/15/ 2015.
- [38] Y. Liu, N. Tuleouva, E. Ramanculov, and A. Revzin, "Aptamer-Based Electrochemical Biosensor for Interferon Gamma Detection," *Analytical Chemistry*, vol. 82, no. 19, pp. 8131-8136, 2010/10/01 2010.
- [39] M. Varshney and Y. Li, "Interdigitated array microelectrodes based impedance biosensors for detection of bacterial cells," *Biosensors and Bioelectronics*, vol. 24, no. 10, pp. 2951-2960, 6/15/ 2009.
- [40] K. J. Cash, F. Ricci, and K. W. Plaxco, "An Electrochemical Sensor for the Detection of Protein–Small Molecule Interactions Directly in Serum and Other Complex Matrices," *Journal of the American Chemical Society*, vol. 131, no. 20, pp. 6955-6957, 2009/05/27 2009.
- [41] C. B. Jacobs, M. J. Peairs, and B. J. Venton, "Review: Carbon nanotube based electrochemical sensors for biomolecules," *Analytica Chimica Acta*, vol. 662, no. 2, pp. 105-127, 3/10/ 2010.
- [42] B. Zhu, M. A. Booth, P. Shepherd, A. Sheppard, and J. Travas-Sejdic, "Distinguishing cytosine methylation using electrochemical, label-free detection of DNA hybridization and ds-targets," *Biosensors and Bioelectronics*, vol. 64, pp. 74-80, 2/15/ 2015.
- [43] A. E. K. Peh and S. F. Y. Li, "Dengue virus detection using impedance measured across nanoporous aluminamembrane," *Biosensors and Bioelectronics*, vol. 42, pp. 391-396, 4/15/ 2013.
- [44] A. Ibraheem and R. E. Campbell, "Designs and applications of fluorescent protein-based biosensors," *Current Opinion in Chemical Biology*, vol. 14, no. 1, pp. 30-36, 2010/02/01/ 2010.
- [45] D. L. Graham, H. A. Ferreira, and P. P. Freitas, "Magnetoresistive-based biosensors and biochips," *Trends in Biotechnology*, vol. 22, no. 9, pp. 455-462, 2004/09/01/ 2004.
- [46] I. M. Thompson *et al.*, "Prevalence of Prostate Cancer among Men with a Prostate-Specific Antigen Level ≤ 4.0 ng per Milliliter," *New England Journal of Medicine*, vol. 350, no. 22, pp. 2239-2246, 2004.

- [47] (2000). *Drinking-Water Standards for New Zealand 2000*. Available: <https://www.health.govt.nz/system/files/documents/publications/drinking-waterstandards-2000.pdf>
- [48] (2016). *Maximum Residue Levels for Agricultural Compounds*.
- [49] I. Schmueser, A. J. Walton, J. G. Terry, H. L. Woodvine, N. J. Freeman, and A. R. Mount, "A systematic study of the influence of nanoelectrode dimensions on electrode performance and the implications for electroanalysis and sensing," (in eng), *Faraday Discuss*, vol. 164, pp. 295-314, 2013.
- [50] David J. Beebe, a. Glennys A. Mensing, and G. M. Walker, "Physics and Applications of Microfluidics in Biology," *Annual Review of Biomedical Engineering*, vol. 4, no. 1, pp. 261-286, 2002.
- [51] H. Ben-Yoav, P. H. Dykstra, W. E. Bentley, and R. Ghodssi, "A microfluidic-based electrochemical biochip for label-free diffusion-restricted DNA hybridization analysis," *Biosensors and Bioelectronics*, vol. 38, no. 1, pp. 114-120, 10// 2012.
- [52] R. Esfandyarpour, H. Esfandyarpour, M. Javanmard, J. S. Harris, and R. W. Davis, "Microneedle biosensor: A method for direct label-free real time protein detection," *Sensors and Actuators B: Chemical*, vol. 177, pp. 848-855, 2// 2013.
- [53] P. H. Dykstra, V. Roy, C. Byrd, W. E. Bentley, and R. Ghodssi, "Microfluidic Electrochemical Sensor Array for Characterizing Protein Interactions with Various Functionalized Surfaces," *Analytical Chemistry*, vol. 83, no. 15, pp. 5920-5927, 2011/08/01 2011.
- [54] Y. Huang and A. J. Mason, "Lab-on-CMOS integration of microfluidics and electrochemical sensors," *Lab on a Chip*, 10.1039/C3LC50437A vol. 13, no. 19, pp. 3929-3934, 2013.
- [55] S. B. Dulay, R. Gransee, S. Julich, H. Tomaso, and C. K. O' Sullivan, "Automated microfluidically controlled electrochemical biosensor for the rapid and highly sensitive detection of *Francisella tularensis*," *Biosensors and Bioelectronics*, vol. 59, no. 0, pp. 342-349, 9/15/ 2014.
- [56] S. Kumar *et al.*, "Microfluidic-integrated biosensors: Prospects for point-of-care diagnostics," *Biotechnology Journal*, vol. 8, no. 11, pp. 1267-1279, 2013.
- [57] T. G. Henares, A. Shirai, K. Sueyoshi, T. Endo, and H. Hisamoto, "Fabrication and packaging of a mass-producible capillary-assembled microchip for simple and multiplexed bioassay," *Sensors and Actuators B: Chemical*, vol. 218, pp. 245-252, 2015/10/31/ 2015.
- [58] R. Esfandyarpour, H. Esfandyarpour, J. S. Harris, and R. W. Davis, "Simulation and fabrication of a new novel 3D injectable biosensor for high throughput

- genomics and proteomics in a lab-on-a-chip device," *Nanotechnology*, vol. 24, no. 46, p. 465301, 2013.
- [59] A. M. Johnson, D. R. Sadoway, M. J. Cima, and R. Langer, "Design and Testing of an Impedance-Based Sensor for Monitoring Drug Delivery," *Journal of The Electrochemical Society*, vol. 152, no. 1, pp. H6-H11, 2005.
- [60] J. R. Windmiller *et al.*, "Microneedle array-based carbon paste amperometric sensors and biosensors," *Analyst*, 10.1039/C1AN00012H vol. 136, no. 9, pp. 1846-1851, 2011.
- [61] D. Klob, M. Fischer, A. Rothermel, J. C. Simon, and A. A. Robitzki, "Drug testing on 3D in vitro tissues trapped on a microcavity chip," *Lab on a Chip*, 10.1039/B800394G vol. 8, no. 6, pp. 879-884, 2008.
- [62] B. J. Privett, J. H. Shin, and M. H. Schoenfish, "Electrochemical Sensors," *Analytical Chemistry*, vol. 82, no. 12, pp. 4723-4741, 2010/06/15 2010.
- [63] C. Berggren, B. Bjarnason, and G. Johansson, "Capacitive Biosensors," *Electroanalysis*, vol. 13, no. 3, pp. 173-180, 2001.
- [64] G. Ulrich, V. Winfried, and Z. Jens, "Recent developments in electrochemical sensor application and technology—a review," *Measurement Science and Technology*, vol. 20, no. 4, p. 042002, 2009.
- [65] F. Patolsky, M. Zayats, E. Katz, and I. Willner, "Precipitation of an Insoluble Product on Enzyme Monolayer Electrodes for Biosensor Applications: Characterization by Faradaic Impedance Spectroscopy, Cyclic Voltammetry, and Microgravimetric Quartz Crystal Microbalance Analyses," *Analytical Chemistry*, vol. 71, no. 15, pp. 3171-3180, 1999/08/01 1999.
- [66] X. Yu *et al.*, "An impedance array biosensor for detection of multiple antibody-antigen interactions," *Analyst*, 10.1039/B517148B vol. 131, no. 6, pp. 745-750, 2006.
- [67] R. Maalouf *et al.*, "Label-Free Detection of Bacteria by Electrochemical Impedance Spectroscopy: Comparison to Surface Plasmon Resonance," *Analytical Chemistry*, vol. 79, no. 13, pp. 4879-4886, 2007/07/01 2007.
- [68] M. Varshney, Y. Li, B. Srinivasan, and S. Tung, "A label-free, microfluidics and interdigitated array microelectrode-based impedance biosensor in combination with nanoparticles immunoseparation for detection of Escherichia coli O157:H7 in food samples," *Sensors and Actuators B: Chemical*, vol. 128, no. 1, pp. 99-107, 12/12/ 2007.
- [69] K. Y. Chan *et al.*, "Ultrasensitive detection of E. coli O157:H7 with biofunctional magnetic bead concentration via nanoporous membrane based

- electrochemical immunosensor," *Biosensors and Bioelectronics*, vol. 41, pp. 532-537, 3/15/ 2013.
- [70] P.-D. Nguyen, T. B. Tran, D. T. X. Nguyen, and J. Min, "Magnetic silica nanotube-assisted impedimetric immunosensor for the separation and label-free detection of *Salmonella typhimurium*," *Sensors and Actuators B: Chemical*, vol. 197, pp. 314-320, 7/5/ 2014.
- [71] F. Lisdat and D. Schäfer, "The use of electrochemical impedance spectroscopy for biosensing," *Analytical and Bioanalytical Chemistry*, journal article vol. 391, no. 5, pp. 1555-1567, 2008.
- [72] B.-Y. Chang and S.-M. Park, "Electrochemical Impedance Spectroscopy," *Annual Review of Analytical Chemistry*, vol. 3, no. 1, pp. 207-229, 2010.
- [73] J. S. Daniels and N. Pourmand, "Label-Free Impedance Biosensors: Opportunities and Challenges," *Electroanalysis*, vol. 19, no. 12, pp. 1239-1257, 2007.
- [74] A. Bogomolova *et al.*, "Challenges of Electrochemical Impedance Spectroscopy in Protein Biosensing," *Analytical Chemistry*, vol. 81, no. 10, pp. 3944-3949, 2009/05/15 2009.
- [75] V. Velusamy, K. Arshak, O. Korostynska, K. Oliwa, and C. Adley, "An overview of foodborne pathogen detection: In the perspective of biosensors," *Biotechnology Advances*, vol. 28, no. 2, pp. 232-254, 2010/03/01/ 2010.
- [76] O. Lazcka, F. J. D. Campo, and F. X. Muñoz, "Pathogen detection: A perspective of traditional methods and biosensors," *Biosensors and Bioelectronics*, vol. 22, no. 7, pp. 1205-1217, 2007/02/15/ 2007.
- [77] G. A. Posthuma-Trumpie, J. Korf, and A. van Amerongen, "Lateral flow (immuno)assay: its strengths, weaknesses, opportunities and threats. A literature survey," *Analytical and Bioanalytical Chemistry*, journal article vol. 393, no. 2, pp. 569-582, January 01 2009.
- [78] G. V. Kaigala *et al.*, "An inexpensive and portable microchip-based platform for integrated RT-PCR and capillary electrophoresis," *Analyst*, 10.1039/B714308G vol. 133, no. 3, pp. 331-338, 2008.
- [79] P. Liu, S. H. I. Yeung, K. A. Crenshaw, C. A. Crouse, J. R. Scherer, and R. A. Mathies, "Real-time forensic DNA analysis at a crime scene using a portable microchip analyzer," *Forensic Science International: Genetics*, vol. 2, no. 4, pp. 301-309, 2008/09/01/ 2008.
- [80] O. Tokel, F. Inci, and U. Demirci, "Advances in Plasmonic Technologies for Point of Care Applications," *Chemical Reviews*, vol. 114, no. 11, pp. 5728-5752, 2014/06/11 2014.

- [81] B. N. Johnson and R. Mutharasan, "Biosensing using dynamic-mode cantilever sensors: A review," *Biosensors and Bioelectronics*, vol. 32, no. 1, pp. 1-18, 2/15/2012.
- [82] J. L. Arlett, E. B. Myers, and M. L. Roukes, "Comparative advantages of mechanical biosensors," *Nat Nano*, 10.1038/nnano.2011.44 vol. 6, no. 4, pp. 203-215, 04//print 2011.
- [83] J. Tamayo, P. M. Kosaka, J. J. Ruz, A. San Paulo, and M. Calleja, "Biosensors based on nanomechanical systems," *Chemical Society Reviews*, 10.1039/C2CS35293A vol. 42, no. 3, pp. 1287-1311, 2013.
- [84] A. Santos, J. J. Davis, and P. R. Bueno, "Fundamentals and applications of impedimetric and redox capacitive biosensors," *Journal of Analytical & Bioanalytical Techniques*, no. S7, p. 1, 2015.
- [85] D. D. Macdonald, "Reflections on the history of electrochemical impedance spectroscopy," *Electrochimica Acta*, vol. 51, no. 8-9, pp. 1376-1388, 1/20/2006.
- [86] G. Wiegand, K. R. Neumaier, and E. Sackmann, "Fast impedance spectroscopy: General aspects and performance study for single ion channel measurements," *Review of Scientific Instruments*, vol. 71, no. 6, pp. 2309-2320, 2000.
- [87] S.-M. Park and J.-S. Yoo, "Peer Reviewed: Electrochemical Impedance Spectroscopy for Better Electrochemical Measurements," *Analytical Chemistry*, vol. 75, no. 21, pp. 455 A-461 A, 2003/11/01 2003.
- [88] X. Huang, H. Chen, H. Deng, L. Wang, S. Liao, and A. Tang, "A fast and simple electrochemical impedance spectroscopy measurement technique and its application in portable, low-cost instrument for impedimetric biosensing," *Journal of Electroanalytical Chemistry*, vol. 657, no. 1-2, pp. 158-163, 7/1/2011.
- [89] M. Min, U. Pliquet, T. Nacke, A. Barthel, P. Annus, and R. Land, "Broadband excitation for short-time impedance spectroscopy," *Physiological Measurement*, vol. 29, no. 6, p. S185, 2008.
- [90] B. Sanchez, G. Vandersteen, R. Bragos, and J. Schoukens, "Optimal multisine excitation design for broadband electrical impedance spectroscopy," *Measurement Science and Technology*, vol. 22, no. 11, p. 115601, 2011.
- [91] B.-Y. Chang and S.-M. Park, "Integrated Description of Electrode/Electrolyte Interfaces Based on Equivalent Circuits and Its Verification Using Impedance Measurements," *Analytical Chemistry*, vol. 78, no. 4, pp. 1052-1060, 2006/02/01 2006.

- [92] M. Nahvi and B. S. Hoyle, "Electrical Impedance Spectroscopy Sensing for Industrial Processes," *IEEE Sensors Journal*, vol. 9, no. 12, pp. 1808-1816, 2009.
- [93] J. Kang, J. Wen, S. H. Jayaram, A. Yu, and X. Wang, "Development of an equivalent circuit model for electrochemical double layer capacitors (EDLCs) with distinct electrolytes," *Electrochimica Acta*, vol. 115, no. 0, pp. 587-598, 1/1/ 2014.
- [94] C. RoyChaudhuri and R. Dev Das, "A biomolecule compatible electrical model of microimpedance affinity biosensor for sensitivity improvement in cell detection," *Sensors and Actuators A: Physical*, vol. 157, no. 2, pp. 280-289, 2// 2010.
- [95] L. V. Protsailo and W. R. Fawcett, "Studies of electron transfer through self-assembled monolayers using impedance spectroscopy," *Electrochimica Acta*, vol. 45, no. 21, pp. 3497-3505, 7/14/ 2000.
- [96] J. Hong *et al.*, "AC frequency characteristics of coplanar impedance sensors as design parameters," *Lab on a Chip*, 10.1039/B410325D vol. 5, no. 3, pp. 270-279, 2005.
- [97] M. D. Porter, T. B. Bright, D. L. Allara, and C. E. D. Chidsey, "Spontaneously organized molecular assemblies. 4. Structural characterization of n-alkyl thiol monolayers on gold by optical ellipsometry, infrared spectroscopy, and electrochemistry," *Journal of the American Chemical Society*, vol. 109, no. 12, pp. 3559-3568, 1987/06/01 1987.
- [98] H. Wang and L. Pilon, "Accurate Simulations of Electric Double Layer Capacitance of Ultramicroelectrodes," *The Journal of Physical Chemistry C*, vol. 115, no. 33, pp. 16711-16719, 2011/08/25 2011.
- [99] E. Gongadze, U. Rienen, and A. Iglič, "Generalized stern models of the electric double layer considering the spatial variation of permittivity and finite size of ions in saturation regime," in *Cellular and Molecular Biology Letters* vol. 16, ed, 2011, p. 576.
- [100] D. C. Grahame, "The Electrical Double Layer and the Theory of Electrocapillarity," *Chemical Reviews*, vol. 41, no. 3, pp. 441-501, 1947/12/01 1947.
- [101] M. S. Kilic, M. Z. Bazant, and A. Ajdari, "Steric effects in the dynamics of electrolytes at large applied voltages. I. Double-layer charging," *Physical Review E*, vol. 75, no. 2, p. 021502, 2007.
- [102] G. J. Brug, A. L. G. van den Eeden, M. Sluyters-Rehbach, and J. H. Sluyters, "The analysis of electrode impedances complicated by the presence of a

- constant phase element," *Journal of Electroanalytical Chemistry and Interfacial Electrochemistry*, vol. 176, no. 1–2, pp. 275-295, 9/25/ 1984.
- [103] A. J. Bard and L. R. Faulkner, "Electrochemical Methods: Fundamentals and Applications," 2nd ed. New York: John Wiley & Sons, Inc., 2000, p. 96.
- [104] A. J. Bard and L. R. Faulkner, "Electrochemical Methods: Fundamentals and Applications," 2nd ed. New York: John Wiley & Sons, Inc., 2000, pp. 377-381.
- [105] T. Jacobsen and K. West, "Diffusion impedance in planar, cylindrical and spherical symmetry," *Electrochimica Acta*, vol. 40, no. 2, pp. 255-262, 2// 1995.
- [106] J. Bisquert and A. Compte, "Theory of the electrochemical impedance of anomalous diffusion," *Journal of Electroanalytical Chemistry*, vol. 499, no. 1, pp. 112-120, 2/23/ 2001.
- [107] Y. Wang, J. Ping, Z. Ye, J. Wu, and Y. Ying, "Impedimetric immunosensor based on gold nanoparticles modified graphene paper for label-free detection of Escherichia coli O157:H7," *Biosensors and Bioelectronics*, vol. 49, pp. 492-498, 11/15/ 2013.
- [108] S. Wu, Q. He, C. Tan, Y. Wang, and H. Zhang, "Graphene-Based Electrochemical Sensors," *Small*, vol. 9, no. 8, pp. 1160-1172, 2013.
- [109] S. Dhanekar and S. Jain, "Porous silicon biosensor: Current status," *Biosensors and Bioelectronics*, vol. 41, no. 0, pp. 54-64, 3/15/ 2013.
- [110] L. Yang, Y. Li, and G. F. Erf, "Interdigitated Array Microelectrode-Based Electrochemical Impedance Immunosensor for Detection of Escherichia coli O157:H7," *Analytical Chemistry*, vol. 76, no. 4, pp. 1107-1113, 2004/02/01 2004.
- [111] P. Van Gerwen *et al.*, "Nanoscaled interdigitated electrode arrays for biochemical sensors," *Sensors and Actuators B: Chemical*, vol. 49, no. 1–2, pp. 73-80, 6/25/ 1998.
- [112] B. Timmer, W. Sparreboom, W. Olthuis, P. Bergveld, and A. van den Berg, "Optimization of an electrolyte conductivity detector for measuring low ion concentrations," *Lab on a Chip*, 10.1039/B201225A vol. 2, no. 2, pp. 121-124, 2002.
- [113] R. de la Rica, A. Baldi, C. Fernández-Sánchez, and H. Matsui, "Selective Detection of Live Pathogens via Surface-Confined Electric Field Perturbation on Interdigitated Silicon Transducers," *Analytical Chemistry*, vol. 81, no. 10, pp. 3830-3835, 2009/05/15 2009.
- [114] Y.-C. Kuo, C.-S. Chen, K.-N. Chang, C.-T. Lin, and C.-K. Lee, "Sensitivity improvement of a miniaturized label-free electrochemical impedance biosensor

- by electrode edge effect," *Journal of Micro/Nanolithography, MEMS, and MOEMS*, vol. 13, no. 3, pp. 033019-033019, 2014.
- [115] L.-C. Hsiung *et al.*, "A planar interdigitated ring electrode array via dielectrophoresis for uniform patterning of cells," *Biosensors and Bioelectronics*, vol. 24, no. 4, pp. 869-875, 2008/12/01/ 2008.
- [116] W. Olthuis, W. Streekstra, and P. Bergveld, "Theoretical and experimental determination of cell constants of planar-interdigitated electrolyte conductivity sensors," *Sensors and Actuators B: Chemical*, vol. 24, no. 1–3, pp. 252-256, 3// 1995.
- [117] O. Laczka, E. Baldrich, F. X. Muñoz, and F. J. del Campo, "Detection of *Escherichia coli* and *Salmonella typhimurium* Using Interdigitated Microelectrode Capacitive Immunosensors: The Importance of Transducer Geometry," *Analytical Chemistry*, vol. 80, no. 19, pp. 7239-7247, 2008/10/01 2008.
- [118] M. Hoyos-Nogués *et al.*, "Impedimetric antimicrobial peptide-based sensor for the early detection of periodontopathogenic bacteria," *Biosensors and Bioelectronics*, vol. 86, pp. 377-385, 2016/12/15/ 2016.
- [119] X. Chen, Y. Wang, J. Zhou, W. Yan, X. Li, and J.-J. Zhu, "Electrochemical Impedance Immunosensor Based on Three-Dimensionally Ordered Macroporous Gold Film," *Analytical Chemistry*, vol. 80, no. 6, pp. 2133-2140, 2008/03/01 2008.
- [120] R. Ferrigno and H. H. Girault, "Finite element simulation of electrochemical ac diffusional impedance. Application to recessed microdiscs," *Journal of Electroanalytical Chemistry*, vol. 492, no. 1, pp. 1-6, 9/29/ 2000.
- [121] R. Michel, C. Montella, C. Verdier, and J. P. Diard, "Numerical computation of the Faradaic impedance of inlaid microdisk electrodes using a finite element method with anisotropic mesh adaptation," *Electrochimica Acta*, vol. 55, no. 21, pp. 6263-6273, 2010.
- [122] I. J. Cutress, E. J. F. Dickinson, and R. G. Compton, "Analysis of commercial general engineering finite element software in electrochemical simulations," *Journal of Electroanalytical Chemistry*, vol. 638, no. 1, pp. 76-83, 2010.
- [123] E. J. F. Dickinson, H. Ekström, and E. Fontes, "COMSOL Multiphysics®: Finite element software for electrochemical analysis. A mini-review," *Electrochemistry Communications*, vol. 40, pp. 71-74, 3// 2014.
- [124] K. Singh, A. Whited, Y. Ragineni, T. Barrett, J. King, and R. Solanki, "3D nanogap interdigitated electrode array biosensors," (in English), *Analytical and Bioanalytical Chemistry*, vol. 397, no. 4, pp. 1493-1502, 2010/06/01 2010.

- [125] R. D. Das, N. Mondal, S. Das, and C. RoyChaudhuri, "Optimized Electrode Geometry for an Improved Impedance Based Macroporous Silicon Bacteria Detector," *IEEE Sensors Journal*, vol. 12, no. 6, pp. 1868-1877, 2012.
- [126] J.-W. Wang, M.-H. Wang, and L.-S. Jang, "Effects of electrode geometry and cell location on single-cell impedance measurement," *Biosensors and Bioelectronics*, vol. 25, no. 6, pp. 1271-1276, 2/15/ 2010.
- [127] K. Nagamine, T. Kaya, T. Yasukawa, H. Shiku, and T. Matsue, "Application of microbial chip for amperometric detection of metabolic alteration in bacteria," *Sensors and Actuators B: Chemical*, vol. 108, no. 1–2, pp. 676-682, 7/22/ 2005.
- [128] F. J. Rawson, A. J. Downard, and K. H. Baronian, "Electrochemical detection of intracellular and cell membrane redox systems in *Saccharomyces cerevisiae*," *Scientific Reports*, vol. 4, p. 5216, 06/09 2014.
- [129] K. Baronian, A. Downard, R. Lowen, and N. Pasco, "Detection of two distinct substrate-dependent catabolic responses in yeast cells using a mediated electrochemical method," (in English), *Applied Microbiology and Biotechnology*, vol. 60, no. 1-2, pp. 108-113, 2002/10/01 2002.
- [130] H. L. Woodvine, J. G. Terry, A. J. Walton, and A. R. Mount, "The development and characterisation of square microfabricated electrode systems," *Analyst*, 10.1039/B924342A vol. 135, no. 5, pp. 1058-1065, 2010.
- [131] R. de la Rica, C. Fernández-Sánchez, and A. Baldi, "Electric preconcentration and detection of latex beads with interdigitated electrodes," *Applied Physics Letters*, vol. 90, no. 17, p. 174104, 2007.
- [132] D. Krulic, N. Fatouros, and D. Khoshtariya, E., "Kinetic data for the hexacyanoferrate (II)/(III) couple on platinum electrode in various chlorides of monovalent cations," *J. Chim. Phys.*, vol. 95, no. 3, pp. 497-512, 1998.
- [133] M. A. Booth, S. Harbison, and J. Travas-Sejdic, "Development of an electrochemical polypyrrole-based DNA sensor and subsequent studies on the effects of probe and target length on performance," *Biosensors and Bioelectronics*, vol. 28, no. 1, pp. 362-367, 10/15/ 2011.
- [134] B. Kannan, D. E. Williams, M. A. Booth, and J. Travas-Sejdic, "High-Sensitivity, Label-Free DNA Sensors Using Electrochemically Active Conducting Polymers," *Analytical Chemistry*, vol. 83, no. 9, pp. 3415-3421, 2011/05/01 2011.
- [135] S.-J. Ding, B.-W. Chang, C.-C. Wu, M.-F. Lai, and H.-C. Chang, "Electrochemical evaluation of avidin–biotin interaction on self-assembled gold electrodes," *Electrochimica Acta*, vol. 50, no. 18, pp. 3660-3666, 6/10/ 2005.

- [136] L. M. Fischer *et al.*, "Gold cleaning methods for electrochemical detection applications," *Microelectronic Engineering*, vol. 86, no. 4, pp. 1282-1285, 2009/04/01/ 2009.
- [137] N. Lassalle *et al.*, "Electronically conductive polymer grafted with oligonucleotides as electrochemical sensors of DNA: Preliminary study of real time monitoring by in situ techniques," *Journal of Electroanalytical Chemistry*, vol. 509, no. 1, pp. 48-57, 8/10/ 2001.
- [138] O. Livnah, E. A. Bayer, M. Wilchek, and J. L. Sussman, "Three-dimensional structures of avidin and the avidin-biotin complex," *Proceedings of the National Academy of Sciences of the United States of America*, vol. 90, no. 11, pp. 5076-5080, 1993.
- [139] M. Kakihana, H. Ikeuchi, G. P. Satô, and K. Tokuda, "Diffusion current at microdisk electrodes—application to accurate measurement of diffusion coefficients," *Journal of Electroanalytical Chemistry and Interfacial Electrochemistry*, vol. 117, no. 2, pp. 201-211, 1/25/ 1981.
- [140] J. LeBlanc, A. J. Mueller, A. Prinz, and M. J. Butte, "Optical planar waveguide for cell counting," *Applied Physics Letters*, vol. 100, no. 4, p. 043701, 2012.
- [141] T. Knieling, M. Shafi, W. Lang, and W. Benecke, "Microlens array production in a microtechnological dry etch and reflow process for display applications," *Journal of the European Optical Society - Rapid publications*, microlens array; quartz glass; microstructures; light focussing; brightness enhancement; interference display vol. 7, 2012.
- [142] I. Kim and P. F. Mentone, "Electroformed nickel stamper for light guide panel in LCD back light unit," *Electrochimica Acta*, vol. 52, no. 4, pp. 1805-1809, 12/1/ 2006.
- [143] Y. Tsuru, M. Nomura, and F. R. Foulkes, "Effects of chloride, bromide and iodide ions on internal stress in films deposited during high speed nickel electroplating from a nickel sulfamate bath," *Journal of Applied Electrochemistry*, journal article vol. 30, no. 2, pp. 231-238, February 01 2000.